Nanoscale Engineering for Mixed-Dimensional Heterostructure Growth and Integration

by

Sangho Lee

B.S., Materials Science and Engineering, Hanyang University, 2012
S.M., Materials Science and Engineering, Massachusetts Institute of Technology, 2019

Submitted to the Department of Mechanical Engineering
in partial fulfillment of the requirements for the degree of

Doctor of Philosophy in Mechanical Engineering

at the

MASSACHUSETTS INSTITUTE OF TECHNOLOGY

February 2022

Signature of author_____
Department of Mechanical Engineering
January 14, 2022

Certified by_____
Jeehwan Kim
Associate Professor, Department of Mechanical Engineering
Thesis Supervisor

Certified by_____
Caroline A. Ross
Professor, Department of Materials Science and Engineering
Thesis Supervisor

Accepted by_____
Nicolas Hadjiconstantinou
Professor, Department of Mechanical Engineering
Chair, Department Committee on Graduate Theses

Nanoscale Engineering for Mixed-Dimensional Heterostructure Growth and Integration

by

Sangho Lee

Submitted to the Department of Mechanical Engineering
on January 14, 2022, in partial fulfillment of the
requirements for the degree of Doctor of Philosophy in
Mechanical Engineering

ABSTRACT

Recent attempts to create van der Waals (vdW)-bonded heterostructures of distinct two-dimensional (2D) crystals has opened new avenues for research, from the fundamental studies of emergent phenomena to the development of practical applications with unique functionalities, which are attributed to a wide variety of configurations attainable with no lattice and processing limitations. Despite compelling opportunities in the field of vdW heterostructures, it still faces a couple of fundamental limitations in scalability, tunability, and degree of physical coupling of electronic properties. On the other hand, remote epitaxy – an emerging growth method of single-crystalline membranes copied from the underlying substrates through the atomically thin graphene interlayer – has been alternatively suggested to solve major challenges in all-2D vdW heterointegration as well as in conventional heteroepitaxy, resulting in high-quality three-dimensional (3D) thin films that can be released from weak vdW interface and transferred/stacked onto arbitrary substrate/layer of interest. Therefore, graphene-based layer transfer technique offers an efficient route to produce all-3D artificial heterostructures analogous to all-2D vdW heterostructures, but 3D components here are expected to show more enhanced physical coupling at their interfaces and a wider range of materials including III-Vs, III-Ns, and complex-oxides, which in general outperforms 2D counterparts in material properties, can be considered as a building block to form heterogeneous stacks. However, remote epitaxy is still in infancy to work universally for all material systems and all epitaxy techniques.

In this thesis, nanoscale engineering is introduced to tackle major challenges in current technologies, especially in remote epitaxy, and to propose new strategies to assemble or integrate a broad range of mixed-dimensional heterostructures that are distinct from the vdW heterostructure counterparts. Three case studies are presented to exemplify how material design and engineering at nanoscale are leveraged to solve long-standing problems that are not readily overcome through the conventional techniques and methodologies: 1) nanopatterned graphene-based universal epitaxy for single-crystalline membrane transfer; 2) freestanding complex-oxide membrane growth and transfer *via* sacrificial interlayer for emergent multiferroics; and 3) self-assembled block copolymer thin films templating hybrid nanostructures.

Thesis Supervisor: Jeehwan Kim
Title: Associate Professor of Mechanical Engineering

Thesis Supervisor: Caroline A. Ross
Title: Professor of Materials Science and Engineering

Acknowledgments

First and foremost, I would like to acknowledge my advisors, Professor Jeehwan Kim and Professor Caroline A. Ross. I am so grateful to Jeehwan for giving me an opportunity to pursue such an amazing area of research even though I had had no background knowledge or related experience at all when I joined his group. I have always been inspired by his passion for research and his leadership. I am also very fortunate to have had a chance to be coadvised by Caroline continuously after my master's degree. There have been so many twists and turns during 5 years working with her, but I was able to get through all the difficulties I encountered thanks to her infinite support and invaluable advice. I will always be grateful to both my advisors for all that they have taught me over my Ph.D. journey.

I would also like to thank Professor Ashwin Gopinath for being my committee member and introducing me his fascinating work of DNA origami. I hope there will be a chance to do a collaborative work with him in the nearer future. Moreover, I have had a privilege to be involved in a variety of collaborations with world-leading colleagues such as Professor Yunfeng Shi, Professor Jinwoo Hwang, Professor Chang-Yong Nam, Professor Hee-Tae Jung, and Dr. Karim Aissou. The work in this thesis would not have been possible without their help.

I am so grateful to all the Prof. Kim's group members, past and present. I have always learned so many new things from such a multidisciplinary team with a variety of backgrounds. Enjoyable work environment and warmhearted people allowed me to easily be part of Jeehwan Kim Research Group. In addition, I would like to thank all the current and prior group members in Ross group. Ross group provided me with a friendly atmosphere to pursue my research and develop my skills.

Serving as a teaching assistant in class 2.675/2.676 is truly a rewarding experience in my graduate studies. It was a wonderful time to interact with Dr. Benita Comeau and all the students who took a class in Fall 2021. I have rather learned a lot from all of them by assisting with the labs and recitations throughout the semester.

When I was totally new to MIT, Korean graduate student society in both departments of DMSE and MechE helped me a lot to ease my concerns and enjoy my Ph.D. adventure. I am very thankful to them for offering me the most memorable graduate experience. It was also a great pleasure spending enjoyable time with my board game, tennis, and badminton friends. I will not forget all the precious time I had with them.

I would like to thank my family for their unconditional love and support. Long Ph.D. journey would not have been possible without patience and encouragement of my parents, Yong Soo Lee and Chae Hee Song. I always respect them with all my heart. I am also grateful to my parents-in-law, Po In Choi, the CEO of KOMAS, and Hyun Ja Baek, for their infinite support. Last but foremost, I would like to express my deepest gratitude and love to my wife, Sujeong Choi, for being my eternal partner. I am the luckiest to meet her in my life and to be with her at the most critical of times. I promise all the best will come to us from now on.

This thesis is dedicated to my family.

January 14, 2022

Sangho Lee

Contents

Part I. Nanopatterned Graphene-Based Universal Epitaxy for Single-Crystalline Membrane Transfer

Part II. Freestanding Complex-Oxide Membrane Growth and Transfer *via* Sacrificial Interlayer for Emergent Multiferroics

Part III. Self-Assembled Block Copolymer Thin Films Templating Hybrid Nanostructures

List of Figures

maps (right) for Ge on graphene/Ge (top), Ge on graphene/GaAs (middle), and GaAs on graphene/Ge (bottom). All scale bars, 2 μm. Redrawn from ref 9.

Figure 2-2. Process incompatibility of remote epitaxy with chemically or thermally weak materials. (a) Schematics of dry process of graphene transfer onto InAs substrate, where Ni etchant chemically degrades InAs. Top-view SEM image (right) showing degraded InAs. (b) Schematics of graphene growth on InAs substrate, where InAs is thermally damaged below growth temperature. Photograph (middle) and atomic force microcopy (AFM) image (right) showing roughened surface of InAs.

Figure 2-3. (a) Conceptual schematic diagrams of lateral overgrowth of epitaxial film on substrate through patterned graphene (n-Gr) interlayer and structural parameters of n-Gr (period, *P*; opening width, *W*; rotation angle, θ). (b) Color-coded table of epitaxial film quality depending on structural parameters of *P*, *W*, and θ_{110}. Top-view SEM images of epitaxial film morphologies formed through n-Gr with (c) *P*=400 nm, *W*=100 nm, and θ_{110}=0 º, (d) *P*=1600 nm, *W*=100 nm, and θ_{110}=0 º, and (e) *P*=800 nm, *W*=100 nm, and θ_{110}=45 º, and through (f) bare graphene. All the results are for GaAs on Ge. All scale bars, 2 μm.

Figure 2-4. (a) EBSD map and (b) electron channeling contrast imaging (ECCI) image for GaAs grown on Ge through n-Gr with *P*=400 nm, *W*=100 nm, and θ_{110}=0 º.

Figure 2-5. (a) Conceptual schematic diagrams of film exfoliation from n-Gr/substrate platform. Exfoliation yield of GaAs membrane released from n-Gr/Ge depending on structural parameters of n-Gr of (b) *P* and *W* and of (c) θ_{110}.

Figure 2-6. (a) Conceptual schematic diagrams of three different modes of crack propagation depending on stress level of Ni stressor: spalling mode (left), exfoliation mode (middle), and

delamination mode (right). (b) Theoretically obtained plot of accumulated strain energy in epitaxial film as a function of internal stress of Ni. Upper and lower bounds of strain energy values for exfoliation mode are empirically determined. (c) Top-view SEM images for respective modes: spalling mode (left), exfoliation mode (middle), and delamination mode (right). All the results are for GaAs on Ge. All scale bars, 5 μm.

Figure 2-7. Theoretically obtained plots exhibiting Ni stressor thickness required for film exfoliation as a function of (a) exfoliated film thickness and (b) graphene coverage. Three different regimes of spalling mode (red), exfoliation mode (yellow), and delamination mode (blue) are identified by comparing stress intensity factors (K_I and K_{II}) with fracture toughness of bare Ge substrate (K_{IC}) and effective fracture toughness of n-Gr/Ge ($K_{IC,eff}$) for respective conditions. For Figure 2-7a and 2-7b, Ni stress is fixed to be 800 MPa and graphene coverage and film thickness are 70 % and 2 μm, respectively.

Figure 2-8. (a) Top-view SEM images and (b) EBSD maps of epitaxial films and (c) top-view SEM images of exfoliated surface of substrates for Ge on n-Gr/Ge, GaAs on n-Gr/Ge, Ge on n-Gr/GaAs, and GaAs on n-Gr/GaAs from left to right as illustrated in corresponding schematics.

Figure 2-9. Top-view SEM images of (a) as patterned n-Gr and (b) as exfoliated n-Gr surfaces. (c) Photographs showing patterned area on substrate side (left) and tape side (side) after film exfoliation process. (d) Photographs showing patterned area on tape side when membrane is bent (left) and returned back (right). All the results are for GaAs on Ge.

Figure 2-10. Schematics (left), top-view SEM images (middle), and cross-sectional transmission electron microscope (TEM) images (right) for (a) GaAs directly grown on bare Ge and (b) GaAs

grown on n-Gr/Ge, exhibiting antiphase boundary (APB)-free epitaxial film in n-Gr-based heteroepitaxy.

Figure 2-11. (a) Cross-sectional SEM image of AlGaAs-based red light-emitting diode (LED) fabricated on GaAs buffer released from n-Gr/Ge platform. (b) I–V curves of LEDs grown on GaAs/Ge (blue) and GaAs/n-Gr/Ge (red).

Figure 2-12. Photographs of emitted red light from LEDs with multiple geometries grown on (a) GaAs/Ge and (b) GaAs/n-Gr/Ge. (c) Electroluminescence (EL) intensity curves for LEDS grown on GaAs/Ge (left) and GaAs/n-Gr/Ge (right).

Figure 2-13. Molecular dynamics (MD) simulation results with atomic representation (left) and dislocation analysis representation (right) of (a) conventional direct heteroepitaxy and (b) n-Gr-based heteroepitaxy for 4% lattice-mismatched heteroepitaxy system.

Figure 2-14. (a) Dislocation density as a function of graphene coverage in n-Gr for InAs on n-Gr/GaAs. Dislocation density values are estimated from (b) ECCI images of InAs grown on bare GaAs (top) and on n-Gr/GaAs with graphene coverage of 50 %, 75 %, 88 %, and 93 % (bottom).

Figure 2-15. Schematics (left) and cross-sectional TEM images (right) for InAs grown on (a) bare InP and on (b) n-Gr/InP. High-resolution cross-sectional TEM images (left) and geometric phase analysis or GPA (right) for (c) directly grown InAs on InP and (d) laterally overgrown InAs on n-Gr/InP.

Figure 2-16. Schematics (left) and top-view SEM images (right) of InAs grown on (a) n-Gr/InP and (b) n-SiO_2/InP with different pattern parameters of *P* and *W*.

Figure 2-17. Cross-sectional TEM images of InAs grown on (a) n-Gr/InP and (b) n-SiO_2/InP. High-resolution TEM images (left) and GPA (middle and right) for InAs laterally overgrown on

(c) n-Gr/InP and (d) n-SiO_2/InP and for InAs directly grown on InP next to edge of (e) n-Gr and (f) n-SiO_2. e_{xx} and e_{yy} plots refer to lattice constant modulation with respect to InP lattice along in-plane and out-of-plane direction, respectively.

Figure 3-1. Process limitation in perovskite remote epitaxy using pulsed laser deposition (PLD). (a) Schematic diagram of $BaTiO_3$ (BTO) remote epitaxy, where graphene is etched in harsh film growth environment of PLD chamber. (b) Photographs of BTO membrane obtained by remote epitaxy *via* molecular beam epitaxy (MBE) (left) and spalled film and substrate when BTO is remote epitaxially grown *via* PLD (right).

Figure 3-2. (a) Overview of process for oxide membrane growth, release, and transfer. (b) Top 1/4 of $Sr_3Al_2O_6$ (SAO) unit cell projected onto (001) plane (left) and 4 × 4 unit cells of $SrTiO_3$ (STO) crystal structure projected onto (001) plane (right). Dashed circles indicate vacancy sites. (c) X-ray diffraction (XRD) scan of 80 nm SAO film on STO (001) substrate. Redrawn from ref 8.

Figure 3-3. (a) Conceptual schematic diagrams of growing and releasing STO membrane *via* sacrificial SAO interlayer. (b) Top-view SEM image and (c) XRD scan of STO film grown on SAO/STO.

Figure 3-4. Photographs exhibiting (a) STO membrane peeling process by dissolving SAO interlayer in de-ionized (DI) water and (b) exfoliated STO membrane and substrate. (c) Top-view SEM image of exfoliated surface of STO membrane. Insets in Figure 3-4a and 3-4c present schematics for thermal release tape (TRT)/Ni/Ti/STO/SAO/STO and STO/Ti/Ni/TRT stacks before and after peeling process, respectively.

Figure 3-5. (a,b) Top-view SEM images, (c,d) EBSD maps, and (e,f) XRD scans of (a,c,e) $BiFeO_3$ (BFO) and (b,d,f) BTO membranes grown on SAO/STO.

Figure 3-6. (a,b) Photographs and (c,d) top-view SEM images of exfoliated surfaces of (a,c) BFO and (b,d) BTO membranes. Insets in Figure 3-6a and 3-6b present schematics for membrane (BFO and BTO)/Ti/Ni/TRT stacks after peeling process, respectively.

Figure 3-7. (a,b) Schematic diagrams, (c,d) top-view SEM images, and (e,f) XRD scans of BFO-$CoFe_2O_4$ (CFO) nanocomposite membranes grown on (a,c,e) SAO/STO and (b,d,f) ultrathin STO-coated SAO/STO.

Figure 3-8. (a,b) Photographs and (c,d) optical microscopy images of exfoliated surfaces of ultrathin STO/BFO-CFO membranes by (a,c) metal stressor/poly(methyl methacrylate) (PMMA) support and (b,d) only metal stressor. Insets in Figure 3-8a and 3-8b present schematics for exfoliated membrane of STO/BFO-CFO/Ti/PMMA/TRT and STO/BFO-CFO/Ti/TRT stacks, respectively.

Figure 3-9. Top-view SEM images of BFO-CFO nanocomposites grown on ultrathin STO-coated (a) SAO/STO (100), (b) SAO/STO (110), and (c) SAO/STO (111). Insets in Figure 3-9a, 3-9b, and 3-9c present schematics for BFO-CFO/STO/SAO stacks grown on STO (100), (110), and (111) substrates, respectively.

Figure 3-10. M–H hysteresis loops of BFO-CFO nanocomposite along out-of-plane (OOP) and in-plane (IP) directions (a) before and (b) after its exfoliation from SAO/STO (100) substrate.

Figure 4-1. (a) Chemical structure of poly(1,1-dimethylsilacyclobutane-*b*-styrene-*b*-lactide) (PDMSB-*b*-PS-*b*-PLA or DSL) and schematic illustrations of self-assembled DSL films. The dominant morphologies obtained in this study for each DSL are presented. DSL-L with symmetric

PDMSB and PS compositions form alternating in-plane lamellae (left) and DSL-H with asymmetric PDMSB and PS fractions exhibit in-plane lamellae combined with hexagonally packed vertical core-shell cylinders (right). Schematics in light grey, blue, and red represent PDMSB, PS, and PLA, respectively. (b) SEM images of the final morphologies in DSL films: Top-view (left), plan-view of terraced layers (middle), and side-view (right). The images mainly show contrast from the oxidized PDMSB nanopatterns.

Figure 4-2. Small-angle X-ray scattering (SAXS) plots of intensity *I(q) vs. q* in nm^{-1} for the bulk morphologies of (a) DSL-L1, (b) DSL-L2, (c) DSL-H1, and (d) DSL-H2 after placing the powders under vacuum at 140 °C for 12 h and cooling slowly down to room temperature. The corresponding morphology and period are noted below the plots.

Figure 4-3. Top-view SEM images of self-assembled morphologies in DSL-H films after annealing in a solvent vapor flow of $CHCl_3$:N_2 = 10:1: (a) DSL-H1 and (b) DSL-H2 showing the vertical core-shell cylinders of PLA-PS after O_2 reactive ion etching (RIE).

Figure 4-4. (a) Schematic illustrations depicting the solvent vapor annealing (SVA) followed by infiltration synthesis to produce SiO_x/PS/ZnO nanostructures in DSL-L films. The purple structure in the spin-coated DSL film represents as-cast DSL-L before microphase separation. Schematics in light grey, blue, red, grey, and yellow represent PDMSB, PS, PLA, SiO_x, and ZnO, respectively. (b) Schematic illustrations (left) of the cross-sections of DSL-L structure before (top) and after (bottom) infiltration of ZnO and TEM images (right) of resultant SiO_x/PS/ZnO nanostructure in DSL-L1 film.

Figure 4-5. TEM images of the cross-sections of DSL-L2 structure after infiltration of ZnO, showing the resultant SiO_x/PS/ZnO three-color lamellae.

Figure 4-6. High-angle annular dark-field (HAADF) scanning transmission electron microscopy (STEM) images and associated energy-dispersive spectroscopy (EDS) area elemental mappings (Si, Zn, and O) for the cross-sections of ZnO infiltrated (a) DSL-L1 and (b) DSL-L2 structures.

Figure 4-7. (a) HAADF STEM image and associated EDS area elemental mappings (Si and O) for a cross-section of non-infiltrated DSL-H1. (b) Bright field image of non-infiltrated DSL-H2. The darker layers are the PDMSB, and the lighter layers include both PS and PLA. The PDMSB shows periodic in-plane changes in contrast corresponding to the vertical cylinders.

Figure 4-8. EDS elemental mappings of both Si (red) and Zn (blue) for DSL structures: (a) DSL-L1 and (b) DSL-L2. Estimated width of each microdomain is indicated.

Figure 4-9. (a) Schematic illustrations depicting SVA followed by infiltration synthesis to produce SiO_x/PS/ZnO nanostructures in DSL-H films. The purple structure in the spin-coated DSL film represents as-cast DSL-H before phase separation. Schematics in light grey, blue, red, grey, and yellow represent PDMSB, PS, PLA, SiO_x, and ZnO, respectively. (b) Schematic illustrations (left) and HAADF STEM images (right) of the cross-sections of DSL-H1 structure before (top) and after (bottom) infiltration of ZnO. The junctions between the lateral and vertical PLA domains are highlighted by orange circles in the schematic and in the magnified STEM image of ZnO infiltrated DSL-H1 structure.

Figure 4-10. HAADF STEM images and associated EDS area elemental mappings (Si, Zn, and O) for the cross-sections of ZnO-infiltrated DSL-H2 structure.

Figure 5-1. Schematic illustrations and plan-view AFM images with height profiles of self-assembled BCP thin films on Si substrates: (a,d,g) Thermally annealed PS-*b*-PMMA (SM-T), (b,e,h) solvent annealed PS-*b*-PMMA (SM-S), and (c,f,i) solvent annealed PS-*b*-P2VP (SV-S)

nanostructures. All BCP morphologies here are vertically aligned PMMA (or P2VP) cylinders in PS matrix exhibiting different topographies as described in AFM profiles. Schematics in blue, red, yellow, and light gray represent PS, PMMA, P2VP, and Si, respectively.

Figure 5-2. (a,b) Schematic illustrations depicting Cu sputtering onto (a) SM-T and (b) SM-S and (c,d) plan-view STEM images of Cu morphologies on the corresponding BCP structures. (e) Schematic of process used to resolve Cu morphology assisted by O_2 RIE. (f,g) Plan-view SEM images of Cu nanostructure on SM-T surface (f) before and (g) after O_2 RIE treatment, which is obtained at specific sputtering condition (R_d = 0.016 nm/s, t = 3 nm). Schematics in blue, red, brown, dark brown, and light gray represent PS, PMMA, Cu, oxidized Cu, and Si, respectively. All the scale bars in the main images and insets are 100 nm.

Figure 5-3. Top-view SEM images of Cu morphologies on the self-assembled SM-T thin films, which are sputtered at (a) R_d = 0.016 nm/s, t = 3 nm, (b) R_d = 0.016 nm/s, t = 6 nm, (c) R_d = 0.049 nm/s, t = 3 nm, and (d) R_d = 0.049 nm/s, t = 6 nm. All the scale bars are 100 nm.

Figure 5-4. Top-view SEM images of oxidized Cu morphologies on the self-assembled SV-S thin films, which are sputtered at (a) R_d = 0.016 nm/s, t = 6 nm, (b) R_d = 0.028 nm/s, t = 10 nm, (c) R_d = 0.028 nm/s, t = 20 nm, and (d) R_d = 0.049 nm/s, t = 35 nm. Insets exhibit the schematics for the respective Cu/SV-S structures. All the scale bars in the SEM images are 200 nm. Schematics in blue, yellow, brown, and light gray represent PS, P2VP, Cu, and Si, respectively.

Figure 5-5. (a) Cu 2p and (b) O 1s X-ray photoelectron spectroscopy (XPS) spectra of Cu sputtered SM-S template. From the bottom to the top, each panel indicates the spectra for nominal Cu thickness of 0 nm, 3 nm, 6 nm, and 15 nm. Each set of spectra is plotted on the same relative scale.

Figure 5-6. (a) Cu 2p and (b) N 1s XPS spectra of Cu sputtered SV-S template. From the bottom to the top, each panel indicates the spectra for nominal Cu thickness of 0 nm, 3 nm, 6 nm, and 15 nm. Each set of spectra is plotted on the same relative scale.

Figure 5-7. (a) TEM characterization result (left) and corresponding color-coded image (right) showing the Cu morphology on SV-S thin film deposited by e-beam evaporation at R_d = 0.01 nm/s, t = 3 nm. Only Cu particles are colored in red in the color-coded image. Blue rings indicate some of the regions of lower particle density which correspond to the surface of the P2VP cylinders. (b) Plan-view TEM images of Cu/SV-S structures, which are electron-beam evaporated at R_d = 0.03 nm/s and R_d = 0.05 nm/s for t = 3 nm (top) and for t = 5 nm and t = 7 nm at R_d = 0.01 nm/s (bottom).

Figure 6-1. Technological advances of n-Gr-based epitaxy. Features expected in both remote epitaxy and n-Gr-based epitaxy are written in black and additional benefits in n-Gr-based epitaxy are written in red.

Figure A. Schematics of (a) wet transfer and (b) dry transfer process to form graphene-coated substrates.

Figure B. Schematics of chemical lift-off process based on the strained layer to transfer perovskite complex-oxide membranes.

List of Tables

Chapter 1

Introduction

1.1 Van der Waals (VdW) Heterostructures

Since the atomic monolayer of carbon, called graphene, was discovered[1], there have been enormous efforts to greatly expand the family of two-dimensional (2D) materials over the past few decades, which now covers a broad range of properties of solid-state systems including metals, semimetals, semiconductors, insulators, topological insulators, and superconductors[2-3]. As illustrated in Figure 1-1, recent attempts to create van der Waals (vdW)-bonded heterostructures of distinct 2D crystals has further opened new avenues for research, from the fundamental studies of emergent phenomena to the development of practical applications with unique functionalities, which are attributed to a wide variety of configurations attainable with no lattice and processing limitations.[3-9] As the synthetic and assembly techniques advance to gain access to diverse classes of nanomaterials, the concept of vdW integration is not only restricted to 2D layered materials but also applied to a combination of materials with different dimensionality to form mixed-dimensional vdW heterostructures, which holds early promise for further progress in either performance or function.[10]

Despite compelling opportunities in the field of vdW heterostructures, it still faces a couple of fundamental limitations in scalability, tunability, and degree of physical coupling of electronic properties. First, it remains a challenge to generate entire families of vdW materials and their

heterostructures over large areas with high electronic quality.[10] In addition, it is challenging to precisely control the doping type, carrier concentration, and stoichiometry of a majority of vdW materials, limiting the range of device functionalities that can be explored.[2,11-12] Above all, vdW heterostructures do not facilitate any hybridization of atomic orbitals across their interfaces due to the absence of dangling bonds on the surface, which minimizes delocalization of carriers and diffusive transport across the vdW interfaces.[10,13] Thus, alternative approaches are required to push the frontier of heterostructure manufacturing without compromising structural, thermal, and chemical compatibilities as well as performance of integrated heterogeneous systems.

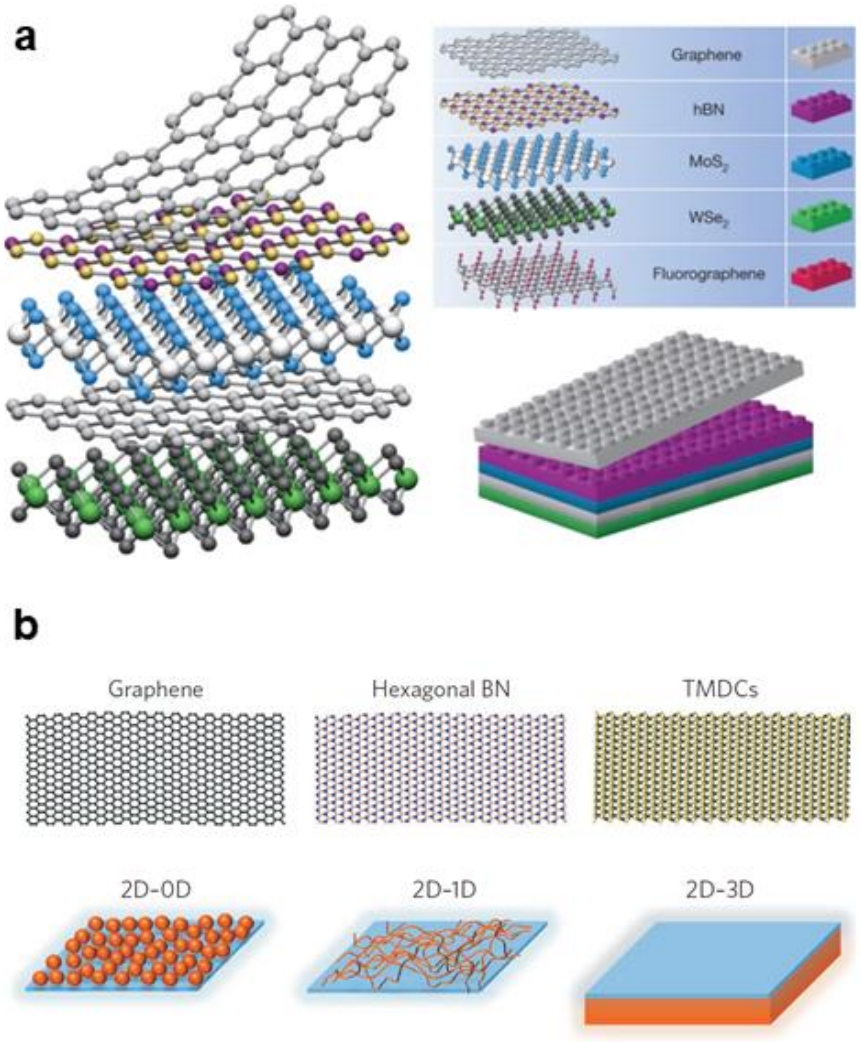

Figure 1-1. (a) Conceptual schematic diagrams of building van der Waals (vdW) heterostructures composed of a wide variety of two-dimensional (2D) layers, which is analogous to stacking Lego blocks. Redrawn from ref 4. (b) Schematic illustrations of prototypical 2D materials (top) and mixed-dimensional vdW heterojunctions (bottom): a heterojunction between 2D and zero-dimensional (0D) materials such as quantum dots or small organic molecules (left), one-dimensional (1D) materials such as nanotubes, nanowires, or polymers (middle), and three-dimensional (3D) materials such as bulk Si, amorphous oxides, or III–V compound semiconductors (right). Redrawn from ref 10.

1.2 Heterointegration of Three-Dimensional (3D) Membranes

Epitaxial lift-off techniques have become of increasing importance to generate freestanding three-dimensional (3D) membranes out of which we can produce all-3D artificial heterostructures, where structurally and chemically incompatible materials are interfaced with each other analogous to all-2D vdW heterostructures.[14] 3D components here are expected to show more enhanced physical coupling at their interfaces owing to the presence of surface dangling bonds, leading to higher interlayer charge transfer in vertical direction. Moreover, a wider range of materials including III-Vs, III-Ns, and complex-oxides, which in general outperforms 2D counterparts in material properties, can be considered as a building block to form the heterogeneous stacks as described in Figure 1-2a.

Four major lift-off technologies have been developed to produce 3D layers that can be separated from host substrate: chemical, optical, mechanical, and 2D-assisted lift-off.[14] Chemical lift-off is a method of creating freestanding thin films by inserting a sacrificial buffer layer in between the epitaxial layer and substrate, which can be selectively removed by proper chemicals (Figure 1-2b). This approach allows producing wafer-scale membranes, but it typically takes several hours to days and forms unwanted byproducts on the substrate, which severely reduces its throughput and substrate reusability. Laser lift-off is a technique of releasing epitaxial layers by inducing excimer lasers that can weaken the film/substrate interface (Figure 1-2c). Although film release rate is relatively high when using this method, it requires transparent substrates such as sapphire and SiC to enable lasers to reach the film/substrate interface across the substrate. In addition, plasma induced at the interface during laser excitation roughens the substrate surface, which needs post-release refurbishment process to use such costly substrates multiple times. Both

chemical and optical lift-off techniques can be only applied to the specific material systems, which limits universal use of such methods. Mechanical lift-off is a brute force method of generating membranes a few μm thick, where a metal stressor layer is deposited on top of epitaxial film to introduce a crack propagating laterally to split the film from the substrate (Figure 1-2d). It is relatively quick process and applicable to a majority of materials, but it is extremely difficult to precisely control the spalling depth, which determines the membrane thickness, and it results in too rough substrate surface after mechanically exfoliating the films.

Among others, 2D material-assisted layer transfer technique in Figure 1-2e is expected to show more advantages in terms of the release rate of membrane, universality of approach, need for post-release refurbishment of substrate, and controllability of membrane thickness. A recently developed method of epitaxially growing single-crystalline thin films across the atomically thin 2D interlayer, which is called remote epitaxy, has opened up new possibilities of producing high-quality 3D membranes on top of 2D materials.[13-19] As 2D surface is slippery due to its weak vdW interaction with the upper layer, epitaxial film remotely grown on it can be easily released from the substrate and subsequently transferred/stacked onto the arbitrary substrate/layer of interest. Here, a quick and seamless exfoliation of 3D membrane can be made at the atomically flat 3D/2D interface, where they barely interact with each other, thus resulting in intact 2D surface to be directly reused for another remote epitaxy without any refurbishment process after peeling off the first epitaxial layers. Furthermore, this approach allows to access a wider variety of material systems compared to chemical and optical lift-off and much thinner films with well-controlled thickness unlike mechanical lift-off. Therefore, such 2D material-based layer growth and transfer technique offers more efficient route to produce all-3D artificial heterostructures than other lift-off techniques do.

However, remote epitaxy is still in infancy to work universally for all material systems and all epitaxy techniques. Recent study found that it is limited to apply remote epitaxy to elemental semiconductors (*e.g.* Si and Ge)[16] and weak III-Vs (*e.g.* InAs and InP) because of their non-polar nature and a difficulty with graphene coating process, respectively. As the ionicity of materials strongly governs a distant atomic interaction between the substrate and epitaxial layer, the weak potential field from non-polar materials is screened by a monolayer of graphene, which in turn prevents their remote epitaxy.[16] Thermally or chemically weak materials that are easily degraded while graphene transfer or growth on them also restrict their remote epitaxy. In particular for complex-oxides, remote epitaxy of specific films (*e.g.* $BaTiO_3$) *via* pulsed laser deposition (PLD) requires too harsh growth environment for graphene to survive during film growth, while relatively mild growth condition of molecular beam epitaxy (MBE) enables their remote epitaxy.[14,17]

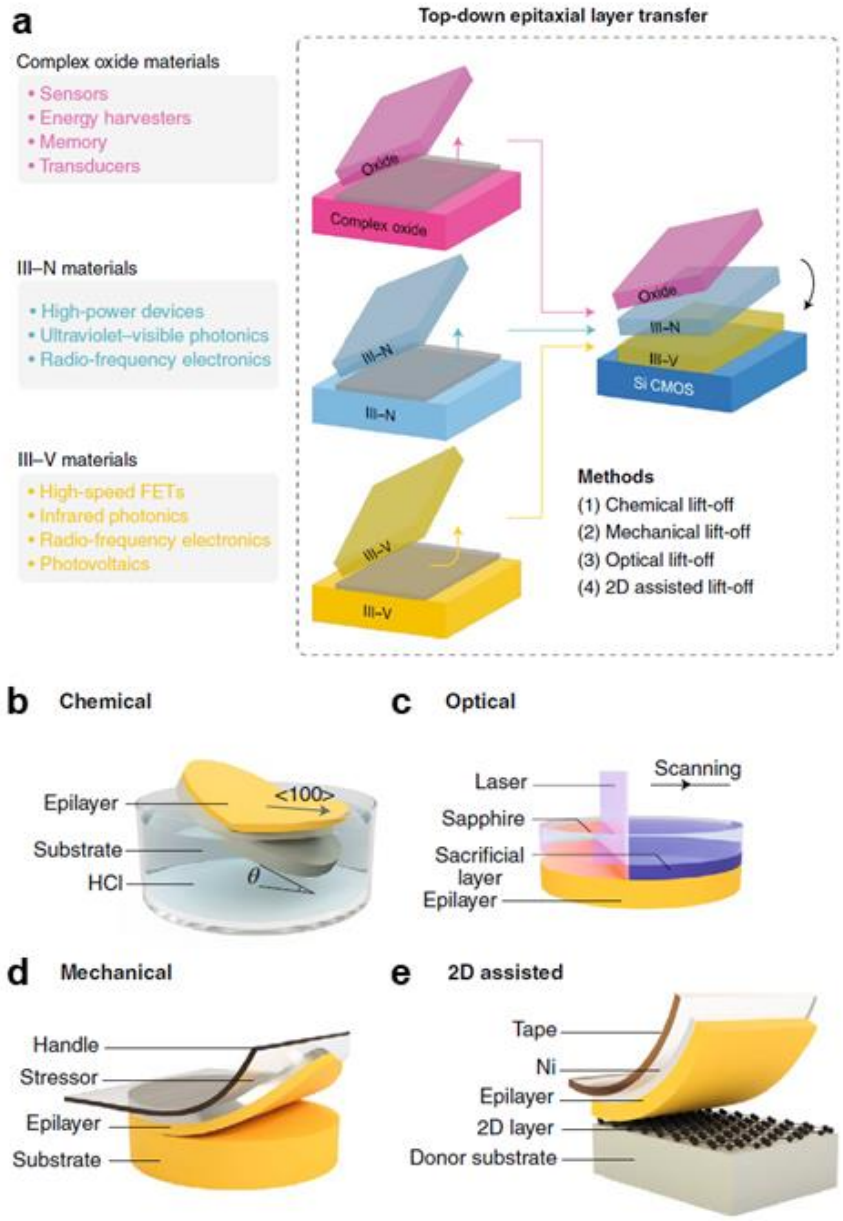

Figure 1-2. (a) Overview of heterogeneous integration of diverse 3D membranes including complex-oxide, III-N, and III-V materials *via* epitaxial lift-off and transfer for electronic and photonic applications. Schematics of epitaxial lift-off techniques based on (b) chemically removable sacrificial layer, (c) optically induced separation of epitaxial layer from substrate, (d) mechanical spalling using metal stressor layer, and (e) 2D material-assisted layer growth and transfer, which is termed remote epitaxy. Redrawn from ref 14.

1.3 Nanoscale Engineering for Mixed-Dimensional Heterostructures

Rational design introducing the nanostructured materials are of vital importance not only to overcome the aforementioned limitations in remote epitaxy, leading to new opportunities in both material physics and device performance, but also to show a great potential of generating a wider variety of mixed-dimensional heterostructures. For example, nanoscale periodic openings in graphene can induce a lateral overgrowth of thin films, where an opening acts as a favorable nucleation site allowing the epitaxy to occur regardless of polarity and process compatibility of materials. Thus, the nanostructured graphene interlayer enables a facile exfoliation of epitaxial films from the substrate depending on its structural parameters such as period and size of openings, thereby providing a universal epitaxy platform that can accommodate the growth, release, and transfer of high-quality membranes with no material restrictions. Also, a strain-mediated magnetoelectric coupling at the interfaces of complex-oxide membranes (both layered and nanocomposite structures) can be well-controlled in an efficient and programmable manner by avoiding any substrate clamping effect. This is feasible when chemical membrane lift-off strategy using an ultrathin water-soluble sacrificial layer[20] instead of 2D materials is assisted by the engineered strain layer-based membrane release process[21]. Slow film release rate is a major drawback of chemical lift-off, but it is solved by introducing the strain at the film/buffer interface to promote dissolving process of sacrificial layer. Moreover, a combined approach of block copolymer self-assembly[22-23] and epitaxy[24] or infiltration synthesis[25] techniques enables the realization of a rich variety of functional hybrid nanostructures (*e.g.* hierarchical 3D nanostructures and heterogeneous metallic nanostructures) in a controlled manner beyond those classically envisioned. As the concept of vdW integration has been extended from all-2D to mixed-

dimensional vdW heterostructures due to the advancement of nanomaterial synthesis and assembly techniques, emerging epitaxial lift-off methods to form all-3D artificial heterostructures can be combined with top-down or bottom-up nanofabrication strategies to leverage the creation of unique heterointegrated nanostructures with mixed-dimensionality.

1.4 Thesis Organization

In this thesis, nanoscale engineering is introduced to tackle major challenges in current technologies, especially in remote epitaxy, and to propose new strategies to assemble or integrate a broad range of mixed-dimensional heterostructures that are distinct from vdW heterostructure counterparts. Three case studies are presented to exemplify how material design and engineering at nanoscale are leveraged to solve long-standing problems that are not readily overcome through the conventional techniques and methodologies: 1) nanopatterned graphene-based universal epitaxy for single-crystalline membrane transfer; 2) freestanding complex-oxide membrane growth and transfer *via* sacrificial interlayer for emergent multiferroics; and 3) self-assembled block copolymer thin films templating hybrid nanostructures.

Part I. Nanopatterned Graphene-Based Universal Epitaxy for Single-Crystalline Membrane Transfer

To develop a universal epitaxy platform that allows the release of single-crystalline group III-V and IV membranes, which have been difficult to generate *via* remote epitaxy, Chapter 2 introduces the nanostructured graphene interlayer that can solve fundamental challenges in remote

epitaxy of non-polar and weak semiconductor materials. It is further demonstrated to significantly reduce a defect density of heteroepitaxial films when epitaxial layers are formed through graphene nanopattern due to its flexible and slippery nature, which provides an additional pathway to produce high-quality epitaxial films even in the heteroepitaxy system. This work will be an effective stepping stone toward developing a new class of epitaxial lift-off that could be widely used not only in the laboratory-scale research but also in the industrial-scale production.

Part II. Freestanding Complex-Oxide Membrane Growth and Transfer *via* Sacrificial Interlayer for Emergent Multiferroics

In Chapter 3, a facile method for generating freestanding complex-oxide membranes is developed to enhance material properties by avoiding substrate clamping effect and to efficiently control physical properties of membrane interfaced with exotic layers. Instead of remote epitaxy that is limited to produce perovskite complex-oxide membranes with high exfoliation yield due to a difficulty of preserving graphene while film growth, we alternatively use chemical lift-off process using water-soluble sacrificial interlayer, which is greatly expedited by applying strains at the film/sacrificial buffer interface while releasing membrane. As this method can not only provide a large-area membrane of high-quality but also be used to generate multiferroic nanocomposite membranes, which enables the accomplishment of more enhanced magnetoelectric coupling effect by making substrate clamping-free composite membrane.

Part III. Self-Assembled Block Copolymer Thin Films Templating Hybrid Nanostructures

In Chapter 4, we self-assemble complicated 3D nanostructures of three-color microdomains consisting of triblock terpolymers. It is extremely hard to resolve such nanoscale 3D morphologies using the conventional characterization techniques due to their low etching and scattering contrast. To better understand the phase behavior of these triblock terpolymers, we employ vapor-phase infiltration technique that can selectively convert one of the organic blocks to the inorganic ZnO, which allows to identify all three polymeric components in the microscopy: a silicon-containing block, ZnO infiltrated block, and remaining organic block. It also provides an efficient pathway to generate 3D heterogeneous nanostructures based on multiblock copolymer templates.

In Chapter 5, a variety of diblock copolymer templates are used to guide the formation of metallic nanostructures onto the specific microdomains by exploiting a difference in mobility of vapor-deposited species on each domain. It is found that a single processing step of sputtering metal on the block copolymer templates can spontaneously form metal nanostructures replicating the underlying block copolymer geometries, which offers a simple route to fabricate heterogeneous functional surfaces at nanoscale.

References

[1] Novoselov, K. S.; Geim, A. K.; Morozov, S. V.; Jiang, D.; Zhang, Y.; Dubonos, S. V.; Grigorieva, I. V.; Firsov, A. A. Electric Field Effect in Atomically Thin Carbon Films. *Science* **2004**, *306*, 666−669.

[2] Jariwala, D.; Sangwan, V. K.; Lauhon, L. J.; Marks, T. J.; Hersam, M. C. Emerging Device Applications for Semiconducting Two-Dimensional Transition Metal Dichalcogenides. *ACS Nano* **2014**, *8*, 1102−1120.

[3] Novoselov, K. S.; Mishchenko, A.; Carvalho, A.; Castro Neto, A. H. 2D Materials and van der Waals Heterostructures. *Science* **2016**, *353*, aac9439.

[4] Geim, A. K.; Grigorieva, I. V. Van der Waals Heterostructures. *Nature* **2013**, *499*, 419−425.

[5] Britnell, L.; Ribeiro, R. M.; Eckmann, A.; Jalil, R.; Belle, B. D.; Mishchenko, A.; Kim, Y.-J.; Gorbachev, R. V.; Georgiou, T.; Morozov, S. V.; Grigorenko, A. N.; Geim, A. K.; Casiraghi, C.; Castro Neto, A. H.; Novoselov, K. S. Strong Light–Matter Interactions in Heterostructures of Atomically Thin Films. *Science* **2013**, *340*, 1311−1314.

[6] Georgiou, T.; Jalil, R.; Belle, B. D.; Britnell, L.; Gorbachev, R. V.; Morozov, S. V.; Kim, Y.-J.; Gholinia, A.; Haigh, S. J.; Makarovsky, O.; Eaves, L.; Ponomarenko, L. A.; Geim, A. K.; Novoselov, K. S.; Mishchenko, A. Vertical Field-Effect Transistor Based on Graphene–WS_2 Heterostructures for Flexible and Transparent Electronics. *Nat. Nanotechnol.* **2013**, *8*, 100−103.

[7] Yu, W. J.; Li, Z.; Zhou, H.; Chen, Y.; Wang, Y.; Huang, Y.; Duan, X. Vertically Stacked Multi-Heterostructures of Layered Materials for Logic Transistors and Complementary Inverters. *Nat. Mater.* **2013**, *12*, 246−252.

[8] Mishchenko, A.; Tu, J. S.; Cao, Y.; Gorbachev, R. V.; Wallbank, J. R.; Greenaway, M. T.; Morozov, V. E.; Morozov, S. V.; Zhu, M. J.; Wong, S. L.; Withers, F.; Woods, C. R.; Kim, Y.-J.; Watanabe, K.; Taniguchi, T.; Vdovin, E. E.; Makarovsky, O.; Fromhold, T. M.; Fal'ko, V. I.; Geim, A. K.; Eaves, L.; Novoselov, K. S. Twist-Controlled Resonant Tunnelling in Graphene/Boron Nitride/Graphene Heterostructures. *Nat. Nanotechnol.* **2014**, *9*, 808−813.

[9] Liu, Y.; Weiss, N. O.; Duan, X.; Cheng, H.-C.; Huang, Y.; Duan, X. Van der Waals Heterostructures and Devices. *Nat. Rev. Mater.* **2016**, *1*, 16042.

[10] Jariwala, D.; Marks, T. J.; Hersam, M. C. Mixed-Dimensional van der Waals Heterostructures. *Nat. Mater.* **2017**, *16*, 170−181.

[11] Wang, H.; Yuan, H.; Hong, S. S.; Li, Y.; Cui, Y. Physical and Chemical Tuning of Two-Dimensional Transition Metal Dichalcogenides. *Chem. Soc. Rev.* **2015**, *44*, 2664−2680.

[12] Chhowalla, M.; Shin, H. S.; Eda, G.; Li, L.-J.; Loh, K. P.; Zhang, H. The Chemistry of Two-Dimensional Layered Transition Metal Dichalcogenide Nanosheets. *Nat. Chem.* **2013**, *5*, 263−275.

[13] Bae, S.-H.; Kum, H.; Kong, W.; Kim, Y.; Choi, C.; Lee, B.; Lin, P.; Park, Y.; Kim, J. Integration of Bulk Materials with Two-Dimensional Materials for Physical Coupling and Applications. *Nat. Mater.* **2019**, *18*, 550−560.

[14] Kum, H.; Lee, D.; Kong, W.; Kim, H.; Park, Y.; Kim, Y.; Baek, Y.; Bae, S.-H.; Lee, K.; Kim, J. Epitaxial Growth and Layer-Transfer Techniques for Heterogeneous Integration of Materials for Electronic and Photonic Devices. *Nat. Electron.* **2019**, *2*, 439−450.

[15] Kim, Y.; Cruz, S. S.; Lee, K.; Alawode, B. O.; Choi, C.; Song, Y.; Johnson, J. M.; Heidelberger, C.; Kong, W.; Choi, S.; Qiao, K.; Almansouri, I.; Fitzgerald, E. A.; Kong, J.; Kolpak, A. M.; Hwang, J.; Kim, J. Remote Epitaxy through Graphene Enables Two-Dimensional Material-Based Layer Transfer. *Nature* **2017**, *544*, 340−343.

[16] Kong, W.; Li, H.; Qiao, K.; Kim, Y.; Lee, K.; Nie, Y.; Lee, D.; Osadchy, T.; Molnar, R. J., Gaskill, D. K.; Myers-Ward, R. L.; Daniels, K. M.; Zhang, Y.; Sundram, S.; Yu, Y.; Bae, S.-H.; Rajan, S.; Shao-Horn, Y.; Cho, K.; Ougazzaden, A.; Grossman, J. C.; Kim, J. Polarity Governs Atomic Interaction through Two-Dimensional Materials. *Nat. Mater.* **2018**, *17*, 999−1004.

[17] Kum, H. S.; Lee, H.; Kim, S.; Lindemann, S.; Kong, W.; Qiao, K.; Chen, P.; Irwin, J.; Lee, J. H.; Xie, S.; Subramanian, S.; Shim, J.; Bae, S.-H.; Choi, C.; Ranno, L.; Seo, S.; Lee, S.; Bauer, J.; Li, H.; Lee, K.; Robinson, J. A.; Ross, C. A.; Schlom, D. G.; Rzchowski, M. S.; Eom, C.-B.; Kim, J. Heterogeneous Integration of Single-Crystalline Complex-Oxide Membranes. *Nature* **2020**, *578*, 75−81.

[18] Bae, S.-H.; Lu, K.; Han, Y.; Kim, S.; Qiao, K.; Choi, C.; Nie, Y.; Kim, H.; Kum, H. S.; Chen, P.; Kong, W.; Kang, B.-S.; Kim, C.; Lee, J.; Baek, Y.; Shim, J.; Park, J.; Joo, M.; Muller, D. A.; Lee, K.; Kim, J. Graphene-Assisted Spontaneous Relaxation towards Dislocation-Free Heteroepitaxy. *Nat. Nanotechnol.* **2020**, *15*, 272−276.

[19] Kim, H.; Lu, K.; Liu, Y.; Kum, H. S.; Kim, K. S.; Qiao, K.; Bae, S.-H.; Lee, S.; Ji, Y. J.; Kim, K. H.; Paik, H.; Xie, S.; Shin, H.; Choi, C.; Lee, J. H.; Dong, C.; Robinson, J. A.; Lee, J.-H.; Ahn, J.-H.; Yeom, G. Y.; Schlom, D. G.; Kim, J. Impact of 2D–3D Heterointerface on Remote Epitaxial Interaction through Graphene. *ACS Nano* **2021**, *15*, 10587−10596.

[20] Lu, D.; Baek, D. J.; Hong, S. S.; Kourkoutis, L. F.; Hikita, Y.; Hwang, H. Y. Synthesis of Freestanding Single-Crystal Perovskite Films and Heterostructures by Etching of Sacrificial Water-Soluble Layers. *Nat. Mater.* **2016**, *15*, 1255−1260.

[21] Kim, J.; Bayram, C.; Park, H.; Cheng, C.-W.; Dimitrakopoulos, C.; Ott, J. A.; Reuter, K. B.; Bedell, S. W.; Sadana, D. K. Principle of Direct van der Waals Epitaxy of Single-Crystalline Films on Epitaxial Graphene. *Nat. Commun.* **2014**, *5*, 4836.

[22] Bates, F. S.; Fredrickson, G. H. Block Copolymers—Designer Soft Materials. *Phys. Today* **1999**, *52*, 32−38.

[23] Ross, C. A.; Berggren, K. K.; Cheng, J. Y.; Jung, Y. S.; Chang, J.-B. Three-Dimensional Nanofabrication by Block Copolymer Self-Assembly. *Adv. Mater.* **2014**, *26*, 4386−4396.

[24] Erb, D. J.; Schlage, K.; Röhlsberger, R. Uniform Metal Nanostructures with Long-Range Order *via* Three-Step Hierarchical Self-Assembly. *Sci. Adv.* **2015**, *1*, e1500751.

[25] Subramanian, A.; Doerk, G.; Kisslinger, K.; Yi, D. H.; Grubbs, R. B.; Nam, C.-Y. Three-Dimensional Electroactive ZnO Nanomesh Directly Derived from Hierarchically Self-Assembled Block Copolymer Thin Films. *Nanoscale* **2019**, *11*, 9533−9546.

Part I

Nanopatterned Graphene-Based Universal Epitaxy for Single-Crystalline Membrane Transfer

Chapter 2

Nanopatterned Graphene as Universal Platform for Releasable Epitaxy with Ultimate Defect Reduction

Remote epitaxy – an emerging growth method of single-crystalline membranes copied from the underlying substrates through the atomically thin graphene interlayer – has greatly expanded material spectrum by efficiently producing costly thin films or heterogeneously integrating unique nanosystems. It was recently demonstrated that slippery graphene promotes a strain relaxation of epitaxial film on its surface, which also allows the heteroepitaxy of lattice-mismatched systems with reduced defect density. Despite such benefits, remote epitaxy has its fundamental limitations in non-polar materials because ionicity of materials strongly governs a distant atomic interaction between the substrate and epitaxial layer. Thermally or chemically weak materials that are incompatible with graphene transfer or growth on them also restrict their remote epitaxy. Here, we introduce periodic openings in graphene to induce a lateral overgrowth of thin films, where an opening acts as a favorable nucleation site allowing the epitaxy to occur regardless of polarity and process compatibility of materials. Nanostructured graphene interlayer enables a facile exfoliation of epitaxial films from substrate as well as a spontaneous relaxation of misfit strain during heteroepitaxy depending on its structural parameters such as period and size of openings. Engineered graphene is thus expected to provide a universal epitaxy platform that can accommodate the growth, release, and transfer of a wider variety of high-quality membranes.

2.1 Introduction

With the advancement of current electronics and photonics, there have been increasing demands for heterogenous integration of dissimilar materials to achieve new physical phenomena at unique interfaces or to realize multifunctional chips in a single platform. Disparate materials of high crystallinity are in general integrated by two major approaches: (1) direct heteroepitaxy of lattice-mismatched materials and (2) epitaxial film transfer from host substrates to foreign substrates.[1] In case of direct heteroepitaxy, elemental semiconductors such as Si and Ge are mainly used as an epitaxial template even for compound semiconductor growth due to their substantially lower cost. Among those, the cheapest Si is a mainstream material as a starting platform to construct III-V-based electronic and optoelectronic devices, while Ge is often considered as a buffer layer because it shows a closer lattice matching to III-V materials. However, dislocation formation is unavoidable in process of relaxing misfit strain in direct heteroepitaxy, which is detrimental to achieve high device performance. It can be mitigated to some extent by additionally introducing the compositionally graded layer (for metamorphic growth)[2] or dielectric barrier material (for epitaxial lateral overgrowth)[3] in between the epitaxial film and substrate. Metamorphic growth requires considerable material consumption though, and it is inevitable to form antiphase boundaries (APBs) in films when elemental semiconductor substrates are used to grow III-V materials, which also degrades device performance. Epitaxial lateral overgrowth based on patterned dielectric barriers can geometrically filter threading dislocations by the edge of their sidewalls, but high aspect ratio pattern is required for effective trapping of dislocations, which also induces facets on the film surface. Thus, it is limited to produce high-quality epitaxial films with no dislocations and APBs *via* conventional heteroepitaxy.

Another representative method to integrate dissimilar materials is epitaxial lift-off.[1] A general idea of epitaxial lift-off process is embedding a weak buffer layer in between the epitaxial film and substrate to release membrane from substrate taking advantage of its weak interface. Then, active layers can be mechanically, chemically, or optically separated from buffer, which offers a route to transfer them onto exotic substrates. Remote epitaxy – an emerging growth method of single-crystalline membranes copied from the underlying substrates through the atomically thin 2D materials – has greatly expanded material spectrum by efficiently producing costly thin films or heterogeneously integrating unique material stacks.[1,4-9] Graphene, as an epitaxial release layer, has been mostly studied among others due to its transparency and slippery surface, which allows for reading the atomic registry of underlying substrate across graphene and subsequently generating freestanding membrane of the same kind with high crystallinity. In addition, recent work demonstrated that graphene also promotes a strain relaxation of active layer on its surface, which even enables heteroepitaxy of lattice-mismatched systems with significantly reduced defect density.[8]

Despite such benefits, remote epitaxy has its fundamental limitations specifically in non-polar materials such as Si and Ge because ionicity of materials strongly governs a distant atomic interaction between the substrate and epitaxial layer.[5] As described in Figure 2-1a, Single-crystalline LiF film, for example, can be formed even through three layers of graphene due to its highest ionic character, while a monolayer graphene is still opaque to Si or Ge that is inherently non-polar. It is clearly shown in Figure 2-1b that film remotely formed across graphene is always polycrystalline if non-polar Ge is introduced to the remote epitaxy system. Another challenge is its process incompatibility with chemically or thermally weak materials including InAs and InP. To generate graphene-coated surface, we in general transfer graphene or directly grow graphene

onto substrate (more details about graphene formation process are described in Appendix A). However, when substrate material is weak and sensitive like InAs or InP, it is easily damaged during graphene coating process, which severely constrains its remote epitaxy (Figure 2-2). As a result, a process window for remote epitaxy of such weak materials becomes extremely narrow. Therefore, more advanced technologies must be leveraged to provide a universal epitaxy platform that can accommodate the growth, release, and transfer of high-quality membranes consisting of non-polar or weak materials to develop a wider variety of modern electronic and photonic devices.

Here, nanoscale periodic openings are introduced in graphene, which is expected to enable both epitaxial growth and film exfoliation when graphene nanopattern (n-Gr) is optimally designed. Furthermore, n-Gr is suggested to be a defect-reduced heteroepitaxy platform as bare graphene exhibited its potential of greatly improving the crystallinity of epitaxial layer by spontaneously relaxing misfit strain instead of forming threading dislocations due to its slippery surface[8]. We demonstrate that n-Gr-coated non-polar and weak substrates enable releasable epitaxy with ultimate defect reduction, which opens up new opportunities in applications that have not been accessible by epitaxial lift-off including remote epitaxy as well as conventional heteroepitaxy.

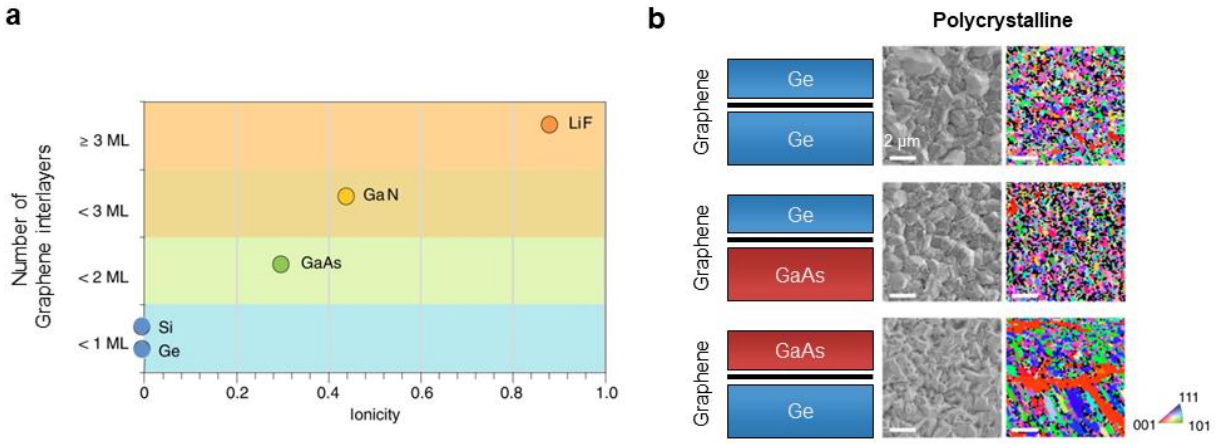

Figure 2-1. (a) The schematic of remote interaction penetration depth depending on ionicity for group IV, III–V and I–VII materials, suggesting graphene transparency increases with material ionicity. Redrawn from ref 5. (b) Remote epitaxy involving elemental materials. Top-view scanning electron microscope (SEM) images (left) and electron backscatter diffraction (EBSD) maps (right) for Ge on graphene/Ge (top), Ge on graphene/GaAs (middle), and GaAs on graphene/Ge (bottom). All scale bars, 2 μm. Redrawn from ref 9.

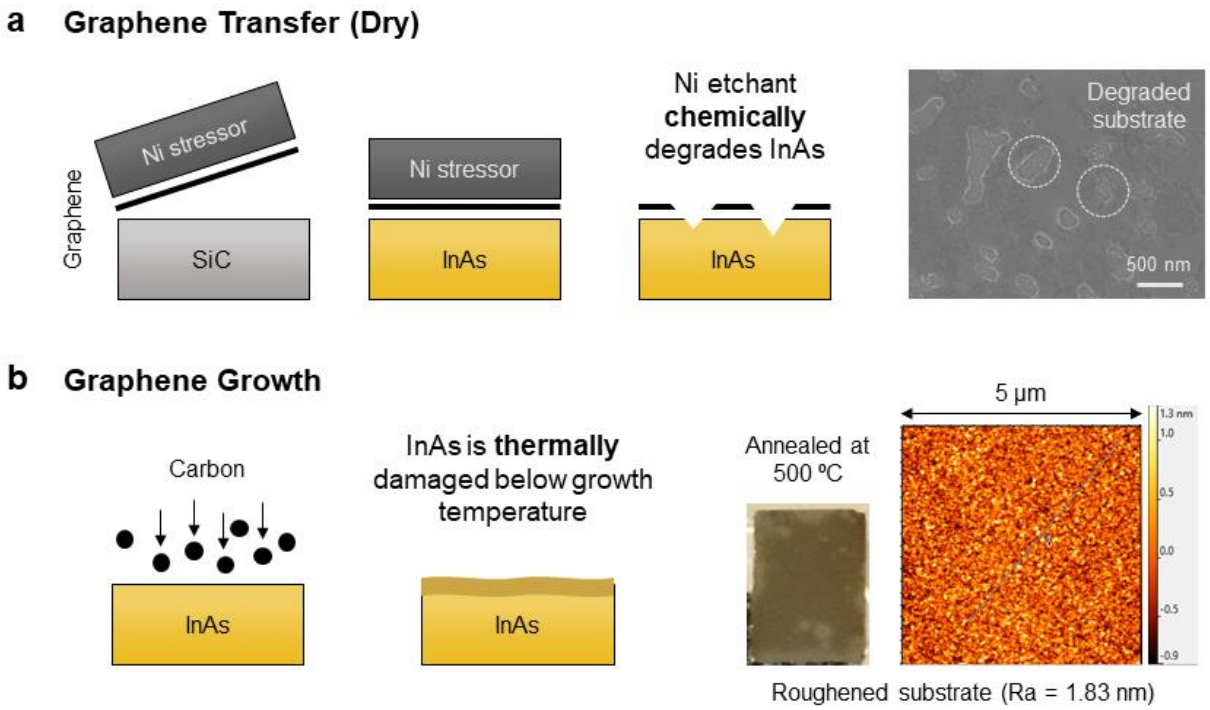

Figure 2-2. Process incompatibility of remote epitaxy with chemically or thermally weak materials. (a) Schematics of dry process of graphene transfer onto InAs substrate, where Ni etchant chemically degrades InAs. Top-view SEM image (right) showing degraded InAs. (b) Schematics of graphene growth on InAs substrate, where InAs is thermally damaged below growth temperature. Photograph (middle) and atomic force microcopy (AFM) image (right) showing roughened surface of InAs.

2.2 Experimental Methods

2.2.1 Graphene Growth and Transfer

For graphene coating on Ge, graphene was directly synthesized on Ge substrate by chemical vapor deposition (CVD), while graphene on GaAs, InAs, and InP substrates were wet transferred from CVD-grown graphene on Cu foils. Ge substrate (and Cu foil) were first annealed in a quartz tube furnace at 920 °C (and 1000 °C) for 30 min under H_2 flow, followed by graphene synthesis under CH_4:H_2 = 200 sccm:1000 sccm (and 4 sccm:70 sccm) flow for 60 min (and 30 min). Wet transfer of Cu-graphene is summarized as follows: (1) polymer support of poly(methyl methacrylate), PMMA was spin-cast on graphene and backed at 120 °C for 2 min, (2) graphene and Cu foil on the rear side were etched by O_2 plasma and in $FeCl_3$ solution, (3) PMMA/graphene stack was rinsed in deionized water and scooped by deoxidized GaAs, InAs, or InP substrate, and (4) PMMA was dissolved in acetone to produce graphene-covered GaAs, InAs, or InP substrate.

2.2.2 Graphene Nanopatterning

To optimize the periodic openings in graphene that enable both epitaxial growth and film exfoliation, n-Gr made up of line patterns with different structural parameters including the period, opening width, and rotation angle was patterned by e-beam lithography (EBL) technique. 50 × 50 μm^2-sized line pattern arrays were formed on the graphene surface with periods of 400 nm, 800 nm, 1200 nm, and 1600 nm, opening widths of 50 nm, 100 nm, and 200 nm, and rotation angles of 0 °, 15 °, 30 °, and 45 °. 200 nm thick PMMA resist layer was first spin-cast on graphene and baked at 180 °C for 2 min. Next, nanoscale patterns with the aforementioned designs were written

on PMMA/graphene by e-beam exposure using Elionix ELS-F125. Exposed samples were developed in methyl isobutyl ketone (MIBK):isopropanol (IPA) = 1:3 for 60 s and washed out in pure IPA. Developed PMMA patterns were then transferred to graphene by reactive ion etching (RIE) *via* Plasma-Therm 790 with O_2 (20 s, 6 mTorr, 90 W), followed by rinsing overlying PMMA layer in acetone to finish n-Gr formation process. For large-area membrane demonstration and light-emitting diode (LED) device fabrication, we employed few mm^2-sized line patterns with optimal structural parameters that simultaneously allow for well-flattened film growth and seamless film exfoliation.

2.2.3 Epitaxial Layer Growth and Exfoliation

All epitaxial growths in this work were performed in a close-coupled showerhead metal organic chemical vapor deposition (MOCVD) reactor. Reactor pressure was kept at 100 Torr throughout the growths using either nitrogen or hydrogen as a carrier gas. GaAs and Ge films were grown at 650 °C using trimethylgallium, arsine, and germane as sources of gallium, arsenic, and germanium, respectively. InAs films were grown at 500 °C using trimethylindium and arsine as sources of indium and arsenic, respectively. LED device stack was regrown on a 2 μm thick GaAs buffer layer at 650 °C in the MOCVD reactor, with 700 nm of p-GaAs contact, 350 nm of p-$Al_{0.65}Ga_{0.35}As$ barrier, 300 nm of $Al_{0.35}Ga_{0.65}As$ emitter, 350 nm of n-$Al_{0.65}Ga_{0.35}As$ barrier, and 100 nm of n-GaAs contact as a capping layer.

To exfoliate epitaxial films, 100 nm of Ti adhesion layer was deposited by e-beam evaporation, followed by sputtering of a few μm thick Ni stressor layer on top of epitaxial layer to induce strain at the film/n-Gr interface. Next, thermal release tape (TRT) is used as a handling

layer to mechanically exfoliate Ni/Ti/epitaxial film stack from n-Gr/substrate. Released stack is then manually attached onto foreign substrate of interest, followed by TRT removal at the elevated temperature of 120−150 °C on hot plates and Ni/Ti etching in $FeCl_3$ solution, resulting in 3D membrane-integrated substrate.

2.2.4 Characterization of Nanopatterned Graphene (n-Gr) and 3D Membrane

To characterize the morphology, crystallinity, and dislocation density of membranes, scanning electron microscope (SEM), electron backscatter diffraction (EBSD), and electron channeling contrast imaging (ECCI) measurements were performed using a ZEISS Merlin high-resolution SEM equipped with EBSD and ECCI detectors. Atomic force microscopy (AFM) measurements were carried out using a Park NX10 AFM tool in non-contact mode to identify the roughness of film surface. When analyzing membranes *via* cross-sectional transmission electron microscope (TEM), samples were protected by amorphous carbon films, which were deposited by electron beam at the early stage, and sequentially polished by FEI Helios 660 with 30 kV, 5 kV, and 2 kV to minimize Ga ion contamination. All TEM images here were obtained using a JEOL ARM 200cF operated at 200 kV and a FEI Titan operated at 120 kV. Geometric phase analysis (GPA) was conducted to measure the strain field between the substrate and target films based on high-resolution TEM images. The GPA had a 0.01% strain resolution.[10] We used DigitalMicrograph with GPA plugin developed by Humboldt-Universität zu Berlin.[11]

2.3 Results and Discussion

2.3.1 Periodic Opening Optimization in n-Gr for Epitaxial Growth and Film Exfoliation

Motivated by the aforementioned challenges in remote epitaxy as well as conventional heteroepitaxy, we have developed an alternative epitaxy platform by engineering graphene expecting that our new approach can embrace materials that have not been accessible by remote epitaxy. When nanoscale periodic openings are introduced in graphene by patterning it, underlying substrate is partially exposed for epitaxial material species to nucleate there first instead of forming other islands on graphene surface. As we further grow film on top, those nucleated islands are merged into a single high-quality film by lateral overgrowth. This method requires optimum pattern parameters that accommodate a fully planarized film *via* lateral overgrowth. In case of line pattern, for instance, too small opening width, *W*, relative to the period, *P*, results in a farther spacing between the adjacent islands, which makes them difficult to be merged into a defect-free film. Also, each material has its own preferable orientation to laterally grow faster than other directions so that a film morphology depends on the rotation angle, θ, of graphene pattern with respect to the cleavage plane of substrate (*e.g.* θ_{110} for Ge). A difference in film morphology depending on theses structural parameters of n-Gr is clearly described in Figure 2-3. While remote epitaxy of GaAs on Ge through bare graphene produces polycrystalline islands that are not merged into a film (Figure 2-3), identical Ge platform with n-Gr, which is structurally optimized, generates a single-crystalline GaAs film with no defects as shown in EBSD mapping data and ECCI image in Figure 2-4, suggesting that polarity of substrate materials is no longer an issue in this approach.

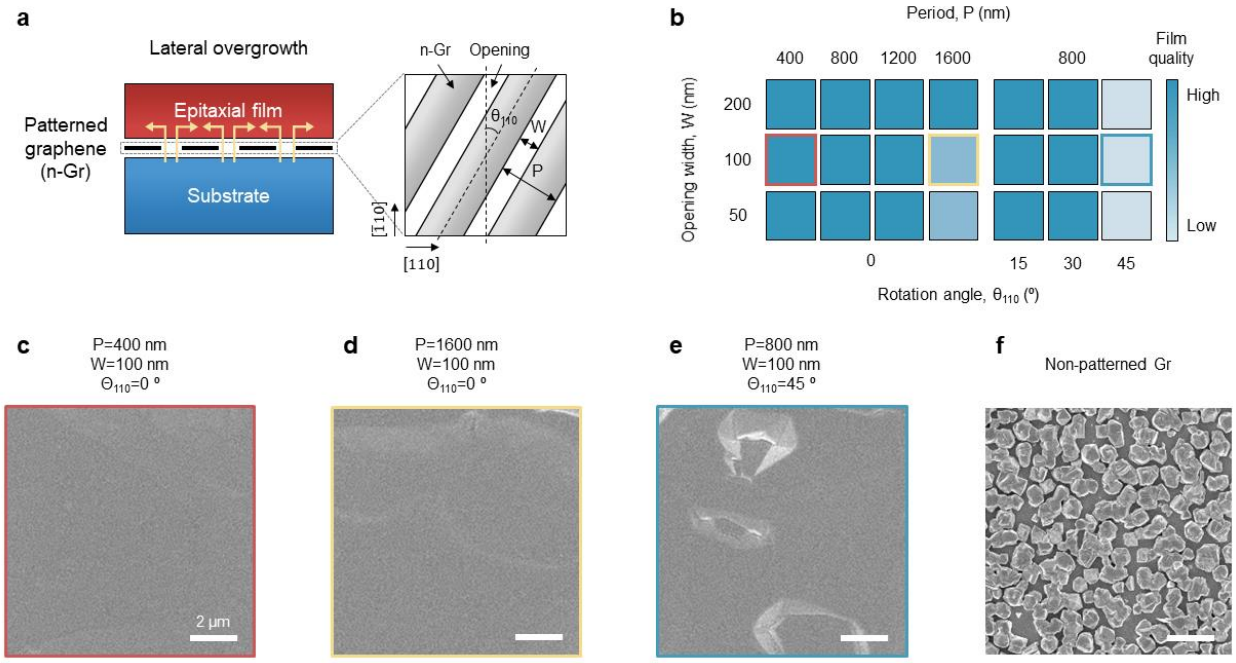

Figure 2-3. (a) Conceptual schematic diagrams of lateral overgrowth of epitaxial film on substrate through patterned graphene (n-Gr) interlayer and structural parameters of n-Gr (period, *P*; opening width, *W*; rotation angle, θ). (b) Color-coded table of epitaxial film quality depending on structural parameters of *P*, *W*, and θ_{110}. Top-view SEM images of epitaxial film morphologies formed through n-Gr with (c) *P*=400 nm, *W*=100 nm, and θ_{110}=0 º, (d) *P*=1600 nm, *W*=100 nm, and θ_{110}=0 º, and (e) *P*=800 nm, *W*=100 nm, and θ_{110}=45 º, and through (f) bare graphene. All the results are for GaAs on Ge. All scale bars, 2 μm.

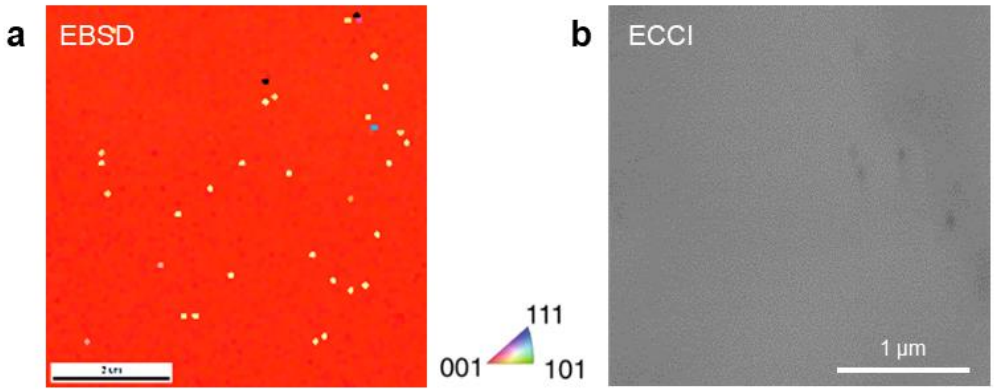

Figure 2-4. (a) EBSD map and (b) electron channeling contrast imaging (ECCI) image for GaAs grown on Ge through n-Gr with P=400 nm, W=100 nm, and θ_{110}=0 º.

2.3.2 Exfoliation Mechanics of 3D Membrane from n-Gr

Epitaxial layer formed across n-Gr can also be peeled off from substrate in a controlled manner depending on the structural parameters of n-Gr as well as the stress level given to the system. First, too large W relative to P results in epitaxial film strongly bound to substrate, significantly reducing the exfoliation yield as described in Figure 2-5b. Also, it shows a θ dependency of film exfoliation yield, indicating that a direction of moment applied with respect to that of line pattern heading toward determines the yield as well (Figure 2-5c). More importantly, strain energy to separate film from substrate is modulated by Ni stressor layer on top of film, and there is an optimal stress window that allows a seamless exfoliation of membrane exactly at the interface with n-Gr. As illustrated in schematics of Figure 2-6, if a stress is too high, a crack penetrates all the way down to substrate generating the unwanted spalling in substrate, while if it is too low, only Ni stressor layer comes off of film leaving film still attached to substrate. Therefore,

targeting a right stress level in between these two bounds is a key to have a nice graphene interface after film exfoliation.

In our approach, a bond strength between graphene and epitaxial layer is orders of magnitude weaker than that between substrate and epitaxial layer (*e.g.* GaAs and GaAs, GaAs and Ge, or Ge and Ge), thus average interfacial bond strength can be effectively decreased by the coverage of n-Gr when compared to the case of direct heteroepitaxy without graphene. In other words, partially covered graphene significantly weakens the interface, which facilitates a crack propagation along the interface. In principle, a crack propagates only when energy release rate by residual stress exceeds the fracture toughness of medium, wherein a direction of propagation is determined by the shear stress. Effective fracture toughness at the n-Gr interface is smaller, which has two important implications: i) crack prefers to propagate along n-Gr even when spalling depth determined by Ni does not exactly match the thickness of epitaxial layer, ii) relatively thin epitaxial layer can be exfoliated, which is not accessible without n-Gr due to high fracture toughness of medium. As described in Figure 2-7a, when 2 μm-thick epitaxial layer is exfoliated by Ni stressor layer with stress level of 800 MPa, it shows a large processing window in Ni thickness from 0.25 μm to 1.62 μm for successful film exfoliation from n-Gr platform with 70 % graphene coverage, while releasing such a thin film is not accessible by the conventional mechanical spalling without n-Gr (minimum releasable film thickness here is estimated to be 10.75 μm at the same Ni stressor condition). Such flexibility is reduced as graphene coverage in n-Gr decreases as shown in Figure 2-7b, where peelable regime is completely vanished when graphene covers less than around 65 % of substrate surface at which spalling depth becomes higher than the film thickness of 2 μm in this example.

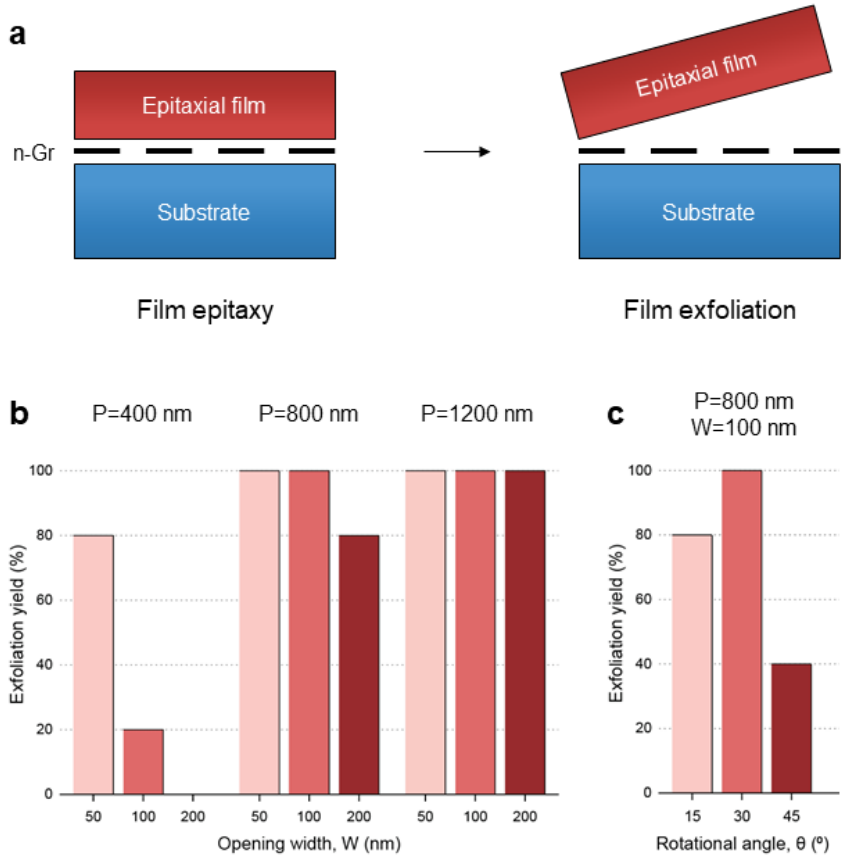

Figure 2-5. (a) Conceptual schematic diagrams of film exfoliation from n-Gr/substrate platform. Exfoliation yield of GaAs membrane released from n-Gr/Ge depending on structural parameters of n-Gr of (b) P and W and of (c) θ_{110}.

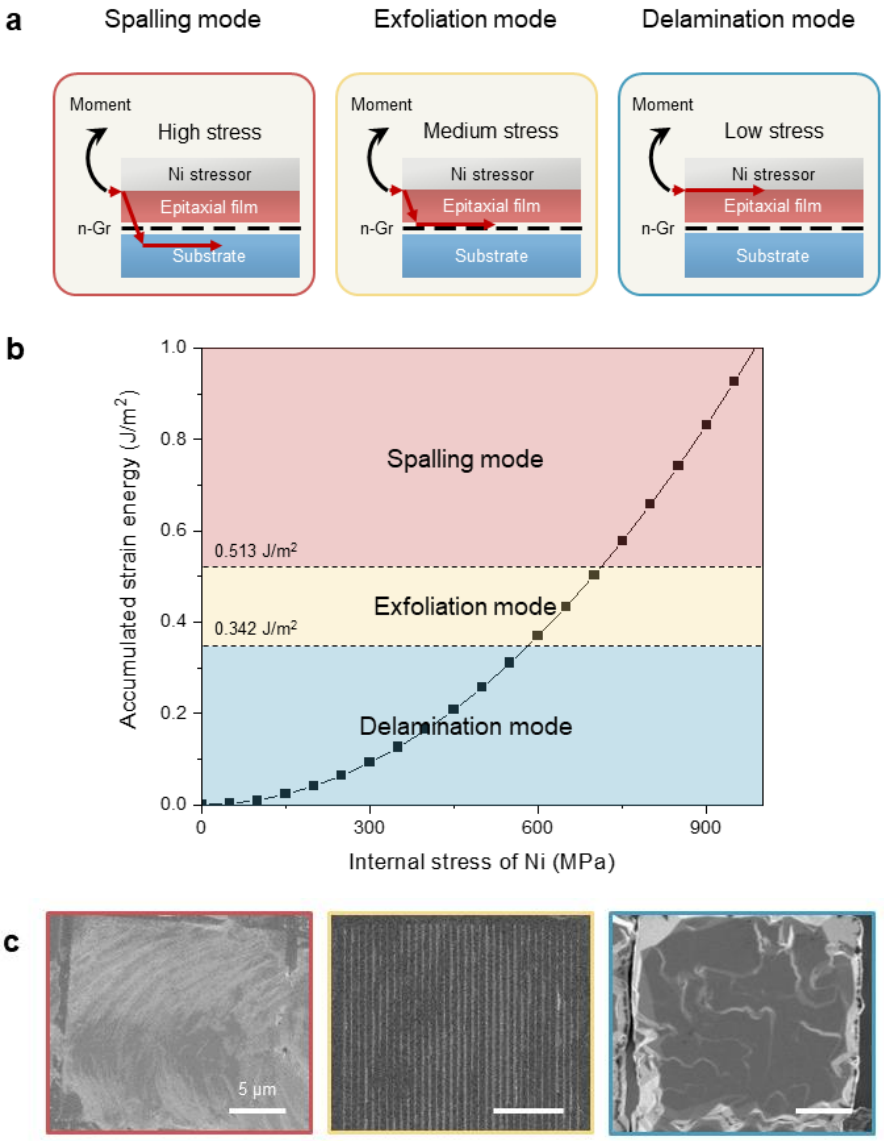

Figure 2-6. (a) Conceptual schematic diagrams of three different modes of crack propagation depending on stress level of Ni stressor: spalling mode (left), exfoliation mode (middle), and delamination mode (right). (b) Theoretically obtained plot of accumulated strain energy in epitaxial film as a function of internal stress of Ni. Upper and lower bounds of strain energy values for exfoliation mode are empirically determined. (c) Top-view SEM images for respective modes: spalling mode (left), exfoliation mode (middle), and delamination mode (right). All the results are for GaAs on Ge. All scale bars, 5 μm.

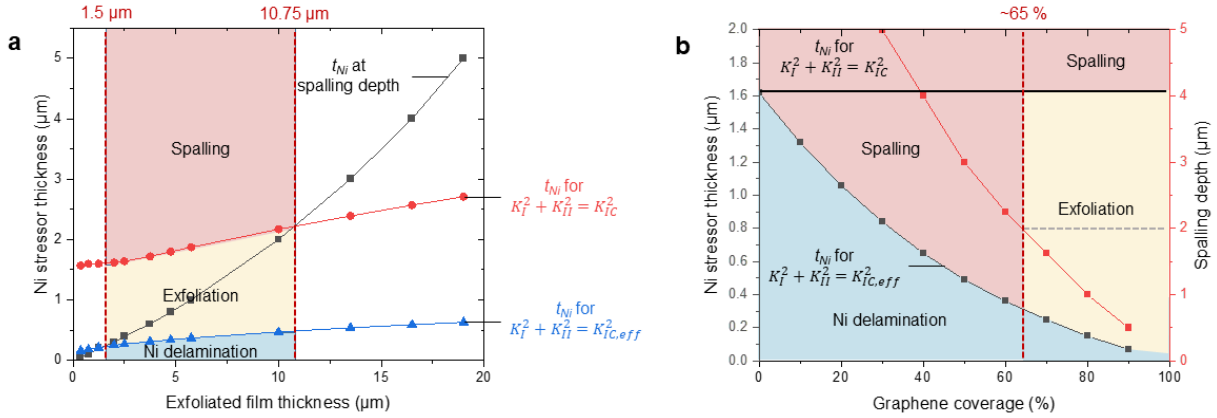

Figure 2-7. Theoretically obtained plots exhibiting Ni stressor thickness required for film exfoliation as a function of (a) exfoliated film thickness and (b) graphene coverage. Three different regimes of spalling mode (red), exfoliation mode (yellow), and delamination mode (blue) are identified by comparing stress intensity factors (K_I and K_{II}) with fracture toughness of bare Ge substrate (K_{IC}) and effective fracture toughness of n-Gr/Ge ($K_{IC,eff}$) for respective conditions. For Figure 2-7a and 2-7b, Ni stress is fixed to be 800 MPa and graphene coverage and film thickness are 70 % and 2 μm, respectively.

2.3.3 Universal Epitaxy for Non-Polar Material-Included System

Given that n-Gr is ideally structured, it provides a universal epitaxy platform that can be even applied to non-polar materials like Ge as summarized in Figure 2-8. For all four different material combinations out of GaAs and Ge, it is clearly demonstrated to produce single-crystalline epitaxial films with good surface morphologies, and to exhibit sharp graphene interface after peeling off epitaxial layers, which has not been possible in remote epitaxy. Furthermore, this method is proved to be applied to generating large-area membrane, which is favorable to be used for real device applications. In Figure 2-9, few mm-sized freestanding GaAs membrane is grown and released

from n-Gr-based epitaxy platform, leaving a clean n-Gr surface after exfoliation process, and the membrane is intact even after bending it with a high curvature because it is thin and flexible enough. We expect that the size of exfoliated membrane can be further increased by introducing top-down large-area patterning techniques such as interference lithography and stepper lithography or bottom-up polymer-based self-assembly techniques such as block copolymer self-assembly and DNA origami self-assembly to pattern graphene instead of using EBL, which is not preferable for such large-scale patterning due to its ridiculously high processing time and cost.

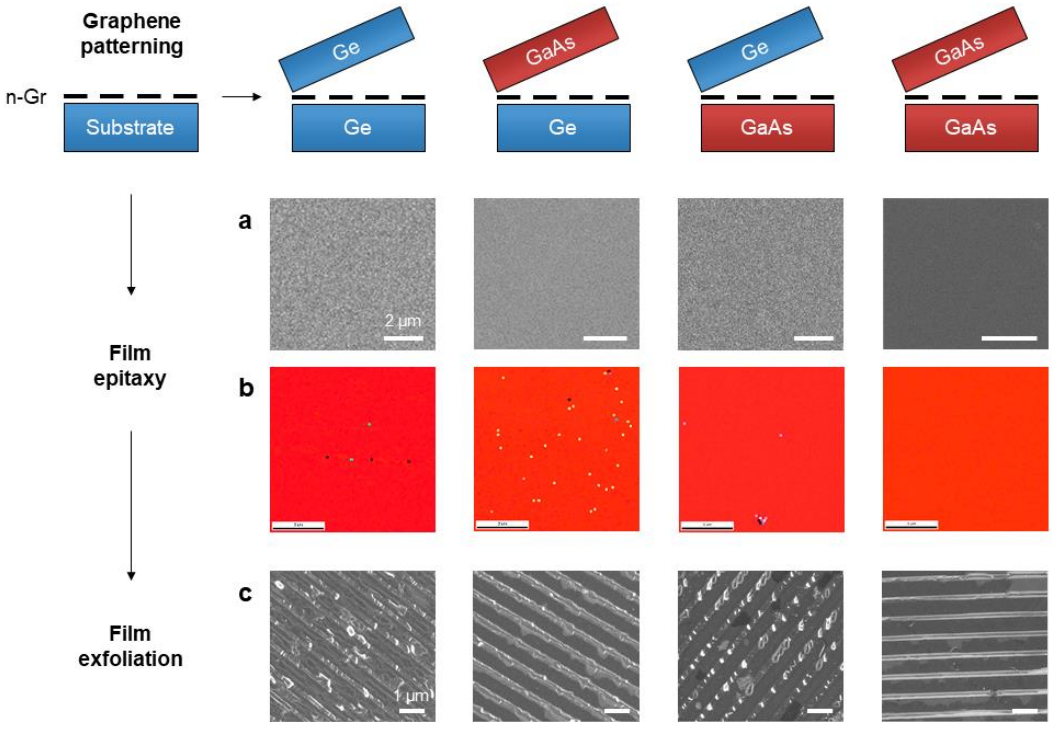

Figure 2-8. (a) Top-view SEM images and (b) EBSD maps of epitaxial films and (c) top-view SEM images of exfoliated surface of substrates for Ge on n-Gr/Ge, GaAs on n-Gr/Ge, Ge on n-Gr/GaAs, and GaAs on n-Gr/GaAs from left to right as illustrated in corresponding schematics.

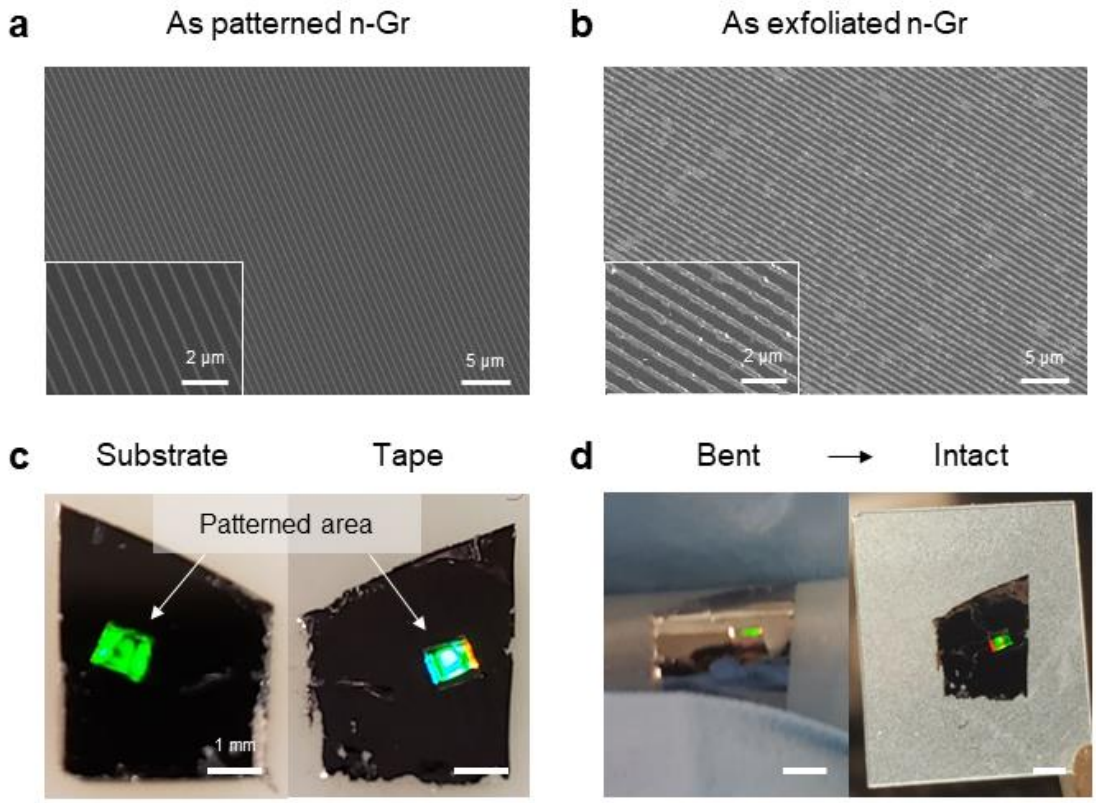

Figure 2-9. Top-view SEM images of (a) as patterned n-Gr and (b) as exfoliated n-Gr surfaces. (c) Photographs showing patterned area on substrate side (left) and tape side (side) after film exfoliation process. (d) Photographs showing patterned area on tape side when membrane is bent (left) and returned back (right). All the results are for GaAs on Ge.

2.3.4 Antiphase Boundary (APB)-Free Heteroepitaxy through n-Gr

We found an additional benefit of nanoscale graphene pattern that allows to form APB-free films even when compound semiconductor film is grown on elemental semiconductor substrate. As shown in Figure 2-10, a noticeable number of APBs is observed in GaAs film directly grown on bare Ge substrate, while the counterpart film does not show any of those defects when it is

formed through n-Gr-coated Ge platform. As a result, fabricated AlGaAs-based red LED device made out of GaAs buffer in each case exhibits clear difference in lighting performance (Figure 2-11 and 2-12). In Figure 2-11a, APB-free LEDs grown on n-Gr are fabricated, followed by peeling with Ni stressor layer and transferring onto polyimide/silicon substrate. I-V curve for direct heteroepitaxy case in Figure 2-11b exhibits an order of magnitude higher dark current at a reverse bias as well as recombination current at a forward bias in comparison with that for n-Gr-based heteroepitaxy, substantiating superior material quality of APB-free LEDs grown on n-Gr. This is also supported by electroluminescence (EL) measurements that show much brighter EL and more efficient current spreading when compared with LEDs grown on bare Ge substrate exhibiting emission only near the contact metals (Figure 2-12). Thus, our new approach offers a simple route to produce a device with more improved optoelectronic quality by eliminating the APBs.

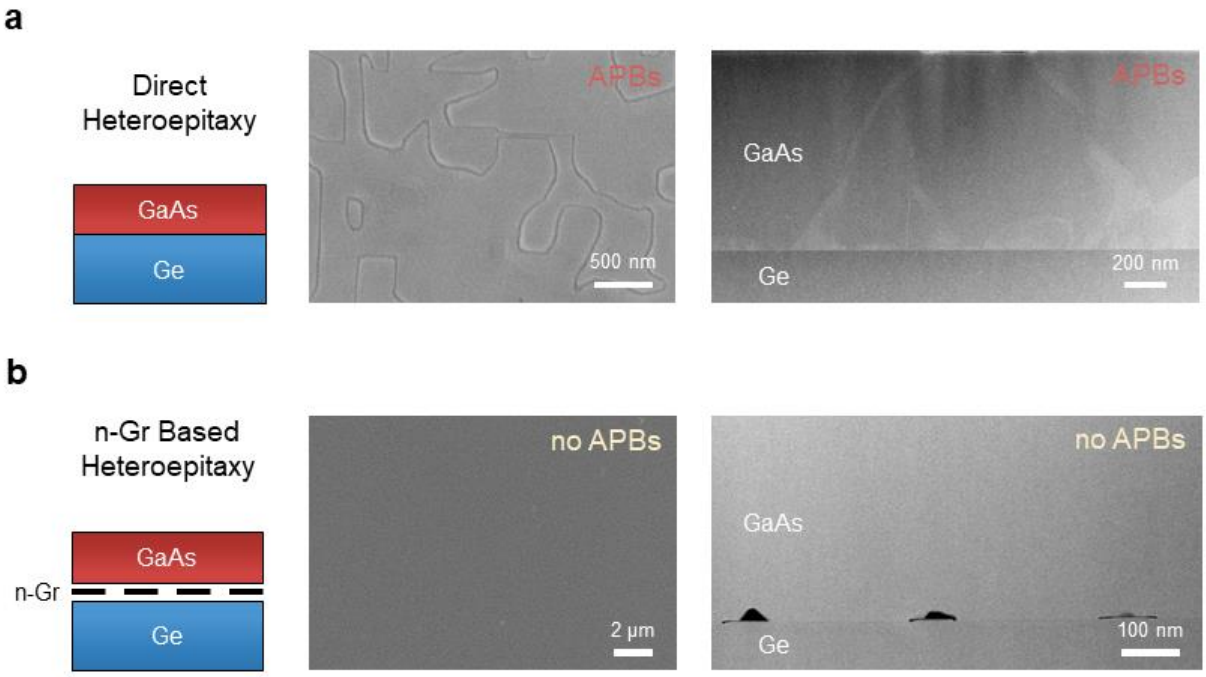

Figure 2-10. Schematics (left), top-view SEM images (middle), and cross-sectional transmission electron microscope (TEM) images (right) for (a) GaAs directly grown on bare Ge and (b) GaAs grown on n-Gr/Ge, exhibiting antiphase boundary (APB)-free epitaxial film in n-Gr-based heteroepitaxy.

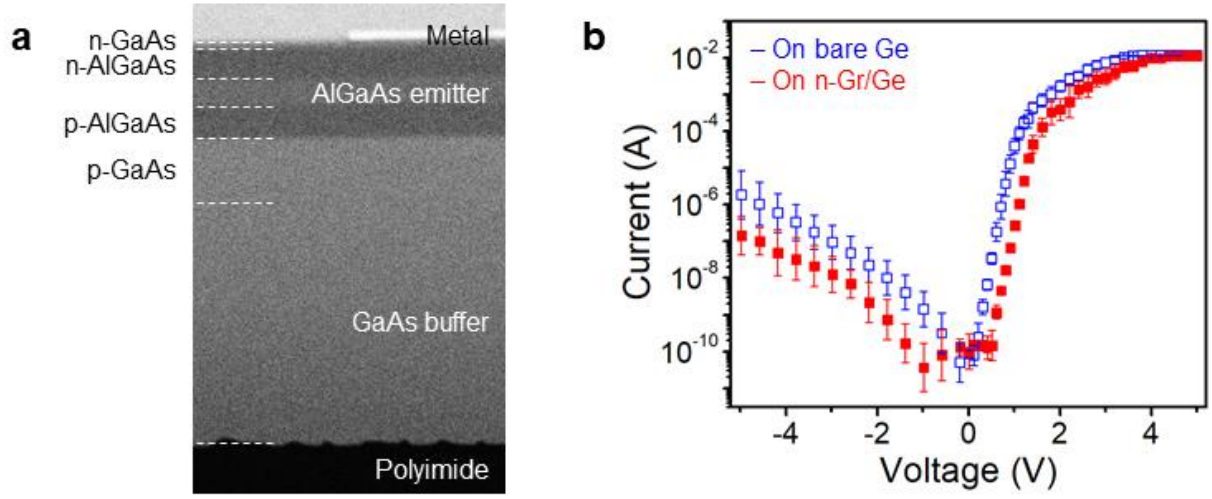

Figure 2-11. (a) Cross-sectional SEM image of AlGaAs-based red light-emitting diode (LED) fabricated on GaAs buffer released from n-Gr/Ge platform. (b) I–V curves of LEDs grown on GaAs/Ge (blue) and GaAs/n-Gr/Ge (red).

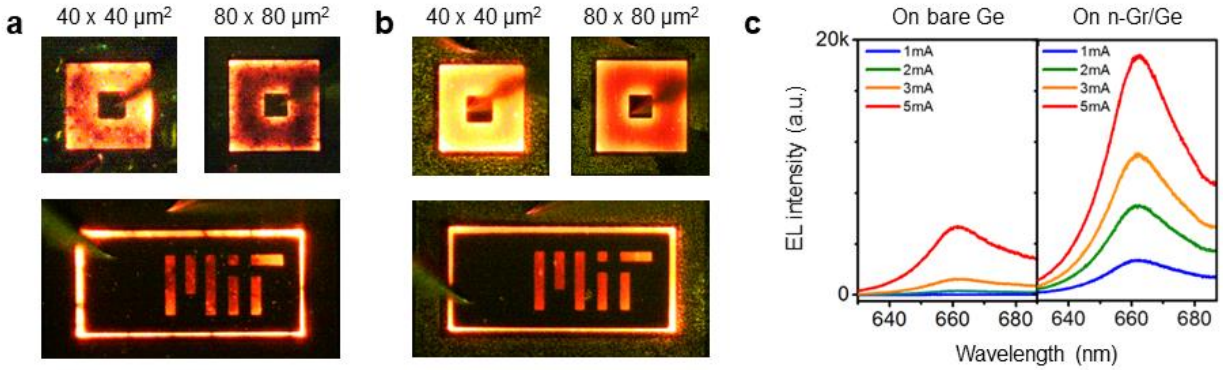

Figure 2-12. Photographs of emitted red light from LEDs with multiple geometries grown on (a) GaAs/Ge and (b) GaAs/n-Gr/Ge. (c) Electroluminescence (EL) intensity curves for LEDS grown on GaAs/Ge (left) and GaAs/n-Gr/Ge (right).

2.3.5 Dislocation-Reduced Heteroepitaxy through n-Gr

Lastly, we elaborate more on our new finding of dislocation-reduced heteroepitaxy based on n-Gr, which could be an alternative pathway to tackle the challenge in remote epitaxy of weak materials like InAs and further allow to produce high-quality InAs membrane out of this approach. By introducing molecular dynamics (MD) simulation, we first observed that epitaxial film is grown with no threading dislocations even on top of 4 % lattice-mismatched substrate when in the presence of n-Gr interlayer, while the same heteroepitaxy system with no graphene exhibits a large number of dislocations as expected (Figure 2-13). More interestingly, our experimental results show a good agreement with these modeling results. As described in Figure 2-14, a misfit dislocation density is rapidly dropped as graphene coverage of n-Gr increases in 7.2 % lattice-mismatched system of InAs on GaAs. Thus, we achieve around an order of magnitude lower dislocation density at the graphene coverage of 93 % compared to a direct heteroepitaxy counterpart as the corresponding ECCI image shows a clear difference in terms of dislocation density.

Further comparative studies based on cross-sectional TEM analysis provides a better understanding in dislocation reduction mechanism of n-Gr platform. Similar to the modeling results in Figure 2-13, InAs film grown on bare InP substrate (3.2 % lattice mismatch) shows a significant number of threading dislocations, while n-Gr-coated InP substrate results in apparently less defect density in InAs film. When we zoom in n-Gr-covered area *via* high-resolution TEM, a laterally overgrown film on graphene exhibits fully relaxed InAs lattice without forming any misfit dislocations, which may be due to the misfit atoms gliding over graphene surface that can flexibly accommodate their atomic arrangements, no longer affected by the atomic registry of underlying

substrate. Therefore, a geometric strain mapping analysis shows an abrupt change in strain level at the graphene interface, while a gradual change is observed at the film/substrate interface in case of direct heteroepitaxy. Based on these results, we speculate that a flexible graphene strip is likely to promote an ultimate reduction of misfit dislocations while lateral overgrowth in our proposed approach, suggesting an additional route to expand material spectrum of high-quality freestanding membranes beyond remote epitaxy.

Furthermore, it is demonstrated in Figure 2-16 and 2-17 that n-Gr platform exhibits a superior dislocation reduction effect and well-planarized film morphology compared to a rigid SiO_2 nanopattern (n-SiO_2) with comparable dimension showing noticeable facets on top surface of films and more threading dislocations throughout films. Here, a combined effect of spontaneous relaxation of InAs on the flexible graphene and partially strained InAs on the patterned area leads to a dramatic reduction of dislocation density in heteroepitaxial InAs, which opens up the possibility of obtaining a defect-free InAs film overcoming 3.2 % lattice mismatch to InP through n-Gr interlayer.

By looking into cross-sectional TEM images and GPA analysis for each case, we notice a clear difference in dislocation reduction mechanism between the n-Gr and n-SiO_2 cases in Figure 2-17. We hypothesize that an inherent flexibility of n-Gr may play a major role in relaxing misfit strain when epitaxial film is laterally growing over graphene strip, while rigid n-SiO_2 is used to physically block threading dislocations by their sidewalls. Epitaxial InAs film right on top of opened area is more or less similar in both cases, where misfit strains are built at the interface and some of them can be a source of defects. However, n-Gr case does not exhibit any noticeable defects near the openings when nucleation there is merged into a film *via* lateral growth over graphene strip, while some threading dislocations that are not fully blocked by the sidewalls of n-

SiO_2 propagate throughout film, as shown in the respective low-magnification TEM images in Figure 2-17. This indicates that a reduction of misfit defects in the conventional selective-area epitaxy based on dielectric barrier materials such as n-SiO_2 is solely dependent on the physical trapping of them by their sidewalls, which thus requires high-aspect ratio pattern in order to improve a dislocation reduction effect. On the other hand, atomically thin n-Gr can show a comparable or even better dislocation reduction effect for the identical system, which supports our hypothesis that slippery and flexible n-Gr promotes a strain relaxation during lateral overgrowth.

High-resolution cross-sectional TEM images and strain mapping results in Figure 2-17 reveal that a local strain is built at the InAs/n-SiO_2 unlike the InAs/n-Gr interface. This is because n-SiO_2 prefers to interact with the upper InAs film due to the presence of dangling bonds on its surface, while n-Gr is not likely to form any bonds with epitaxial InAs layer as it can only have a vdW interaction with adjacent materials. Thus, unwanted strain accumulated on n-SiO_2 surface could be another source of defects, which is not desirable to reduce defect density in heteroepitaxial layer. In other words, a flexibility as well as a dangle bond-free surface of graphene enable improving material quality of laterally overgrown heteroepitaxial film when compared with the case of conventional n-SiO_2-based lateral overgrowth.

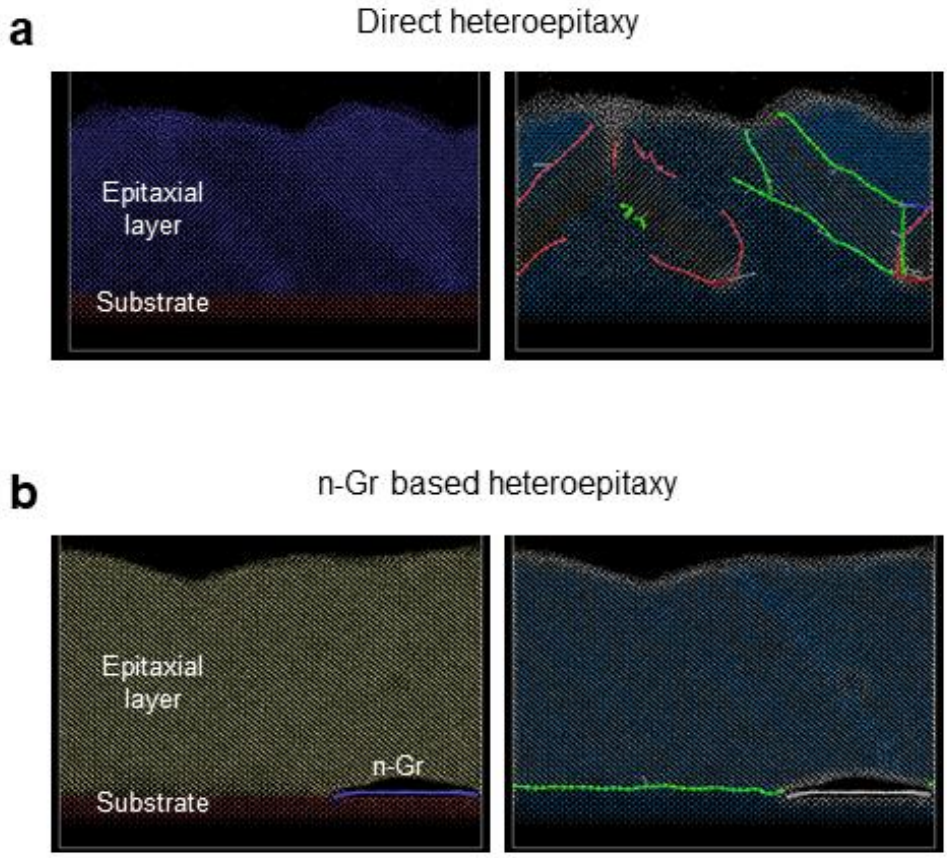

Figure 2-13. Molecular dynamics (MD) simulation results with atomic representation (left) and dislocation analysis representation (right) of (a) conventional direct heteroepitaxy and (b) n-Gr-based heteroepitaxy for 4% lattice-mismatched heteroepitaxy system.

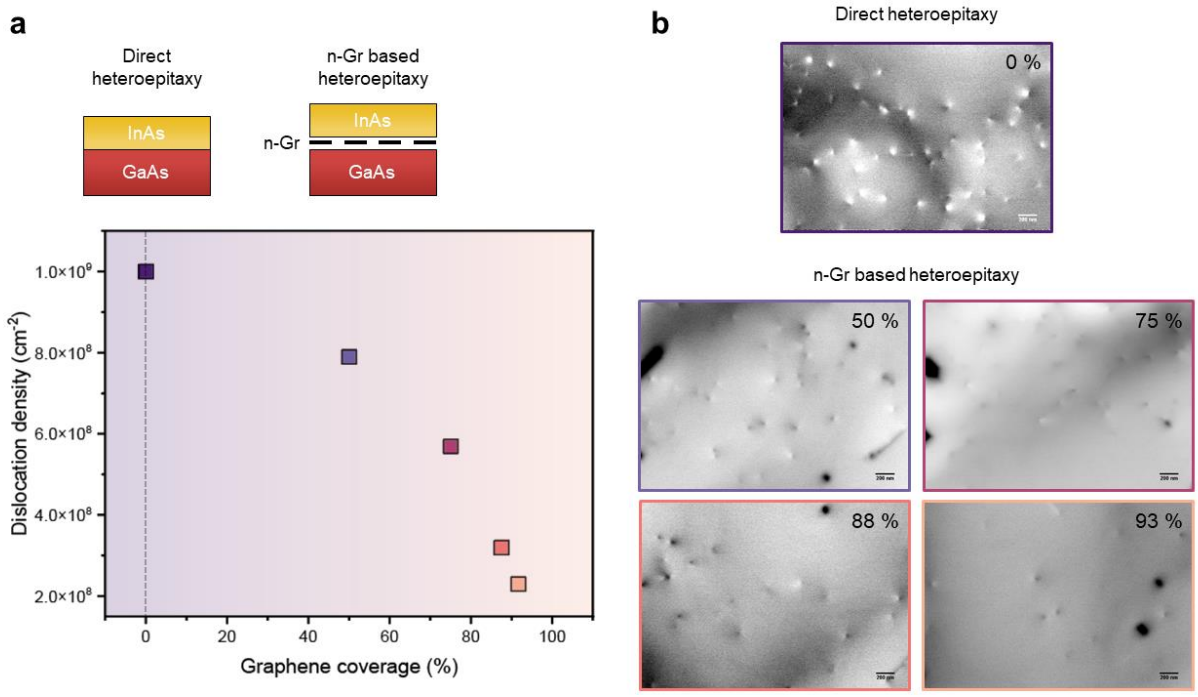

Figure 2-14. (a) Dislocation density as a function of graphene coverage in n-Gr for InAs on n-Gr/GaAs. Dislocation density values are estimated from (b) ECCI images of InAs grown on bare GaAs (top) and on n-Gr/GaAs with graphene coverage of 50 %, 75 %, 88 %, and 93 % (bottom).

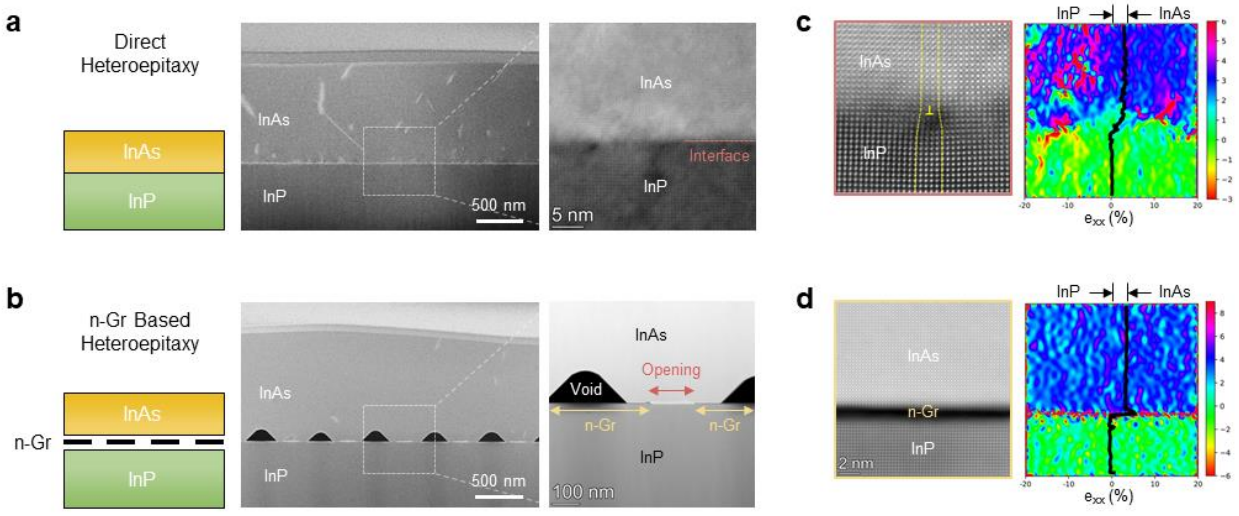

Figure 2-15. Schematics (left) and cross-sectional TEM images (right) for InAs grown on (a) bare InP and on (b) n-Gr/InP. High-resolution cross-sectional TEM images (left) and geometric phase analysis or GPA (right) for (c) directly grown InAs on InP and (d) laterally overgrown InAs on n-Gr/InP.

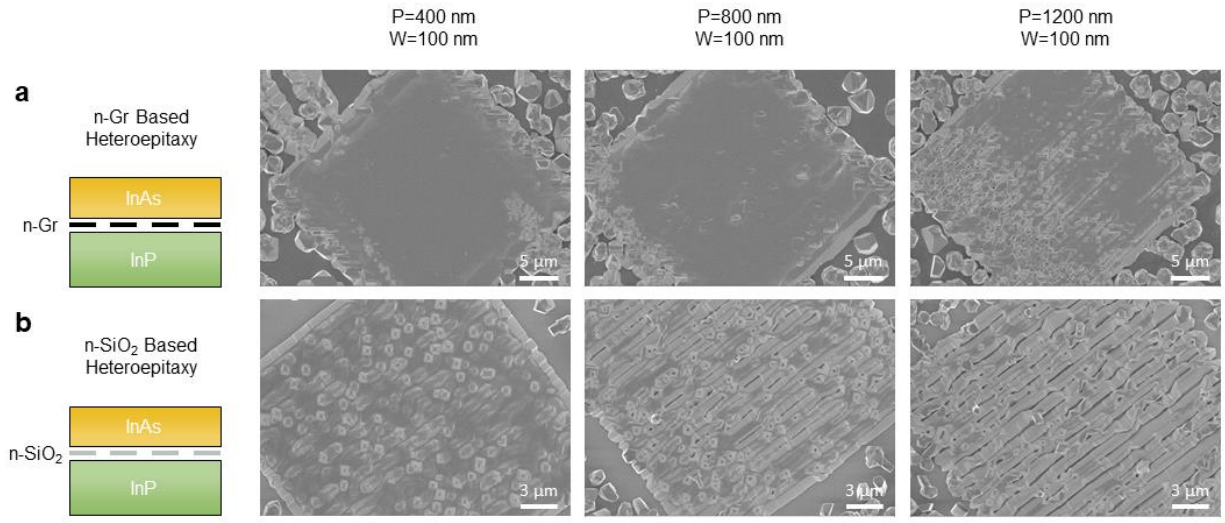

Figure 2-16. Schematics (left) and top-view SEM images (right) of InAs grown on (a) n-Gr/InP and (b) n-SiO_2/InP with different pattern parameters of *P* and *W*.

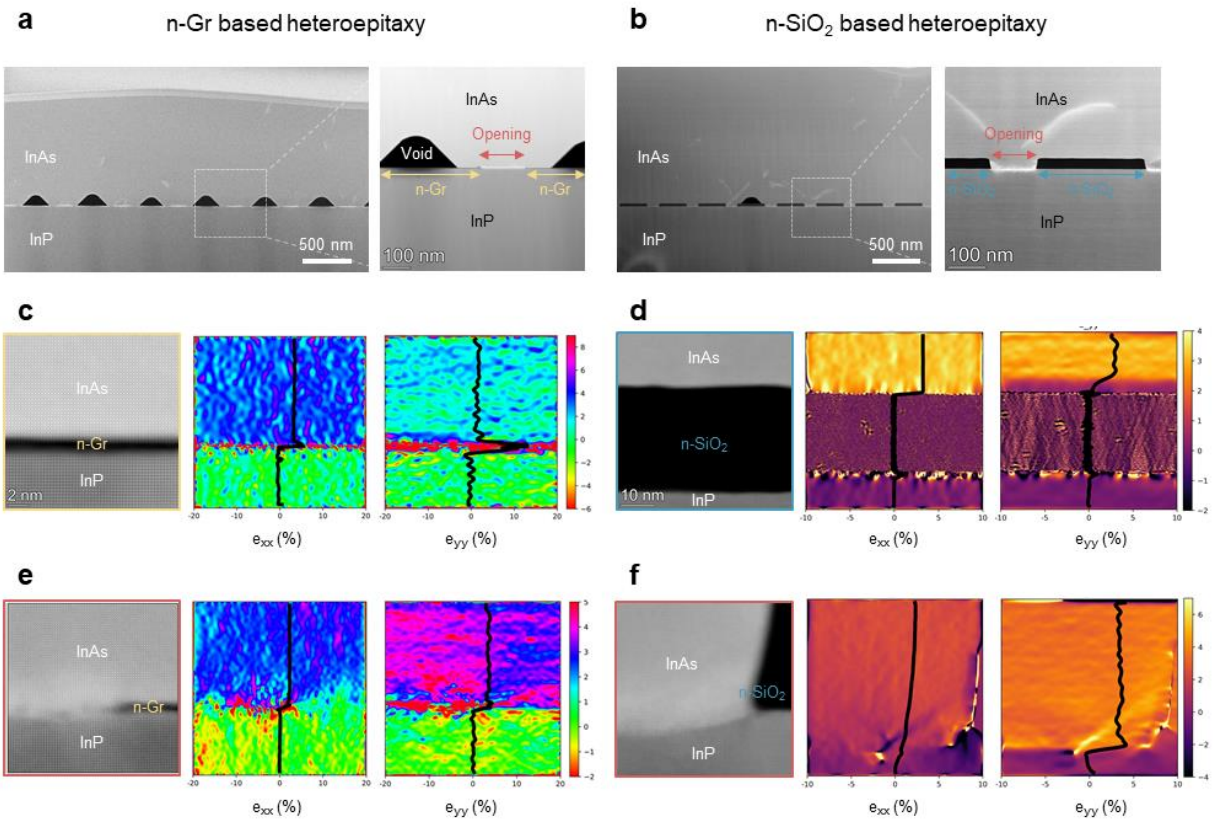

Figure 2-17. Cross-sectional TEM images of InAs grown on (a) n-Gr/InP and (b) n-SiO_2/InP. High-resolution TEM images (left) and GPA (middle and right) for InAs laterally overgrown on (c) n-Gr/InP and (d) n-SiO_2/InP and for InAs directly grown on InP next to edge of (e) n-Gr and (f) n-SiO_2. e_{xx} and e_{yy} plots refer to lattice constant modulation with respect to InP lattice along in-plane and out-of-plane direction, respectively.

2.4 Conclusions

In conclusion, we propose n-Gr as a universal platform for the epitaxy of single-crystalline films, where both elemental and compound semiconductors can be used for the substrate as well as the epitaxial layer. Relatively thin films can be grown and exfoliated in a controlled manner *via* mechanical lift-off with using a nickel stressor, which is not accessible by the conventional mechanical spalling of bare substrate. More importantly, the formation of APBs is prevented when III-V films are grown on elemental substrates with graphene stripes, offering an access to high-quality optoelectronic devices based on III-V thin films that can be made freestanding and transferred onto foreign platforms for heterointegration. We also unveil the mechanism of dislocation reduction by employing dangling bond-free, ultrathin, and deformable n-Gr interlayer in lattice-mismatched heteroepitaxy. Our findings provide a new path for generating a wide variety of high-quality single-crystalline membranes with no constraints of material and process compatibilities and lattice-matching requirements, which have been a critical obstacle to build heterointegrated multifunctional systems.

References

[1] Kum, H.; Lee, D.; Kong, W.; Kim, H.; Park, Y.; Kim, Y.; Baek, Y.; Bae, S.-H.; Lee, K.; Kim, J. Epitaxial Growth and Layer-Transfer Techniques for Heterogeneous Integration of Materials for Electronic and Photonic Devices. *Nat. Electron.* **2019**, *2*, 439−450.

[2] Kohen, D.; Nguyen, X. S.; Yadav, S.; Kumar, A.; Made, R. I; Heidelberger, C.; Gong, X.; Lee, K. H.; Lee, K. E. K.; Yeo, Y. C.; Yoon, S. F.; Fitzgerald, E. A. Heteroepitaxial Growth of $In_{0.30}Ga_{0.70}As$ High-Electron Mobility Transistor on 200 mm Silicon Substrate Using Metamorphic Graded Buffer. *AIP Adv.* **2016**, *6*, 085106.

[3] Kapolnek, D.; Keller, S.; Vetury, R.; Underwood, R. D.; Kozodoy, P.; Den Baars, S. P.; Mishra, U. K. Anisotropic Epitaxial Lateral Growth in GaN Selective Area Epitaxy. *Appl. Phys. Lett.* **1997**, *71*, 1204−1206.

[4] Kim, Y.; Cruz, S. S.; Lee, K.; Alawode, B. O.; Choi, C.; Song, Y.; Johnson, J. M.; Heidelberger, C.; Kong, W.; Choi, S.; Qiao, K.; Almansouri, I.; Fitzgerald, E. A.; Kong, J.; Kolpak, A. M.; Hwang, J.; Kim, J. Remote Epitaxy through Graphene Enables Two-Dimensional Material-Based Layer Transfer. *Nature* **2017**, *544*, 340−343.

[5] Kong, W.; Li, H.; Qiao, K.; Kim, Y.; Lee, K.; Nie, Y.; Lee, D.; Osadchy, T.; Molnar, R. J., Gaskill, D. K.; Myers-Ward, R. L.; Daniels, K. M.; Zhang, Y.; Sundram, S.; Yu, Y.; Bae, S.-H.; Rajan, S.; Shao-Horn, Y.; Cho, K.; Ougazzaden, A.; Grossman, J. C.; Kim, J. Polarity Governs Atomic Interaction through Two-Dimensional Materials. *Nat. Mater.* **2018**, *17*, 999−1004.

[6] Bae, S.-H.; Kum, H.; Kong, W.; Kim, Y.; Choi, C.; Lee, B.; Lin, P.; Park, Y.; Kim, J. Integration of Bulk Materials with Two-Dimensional Materials for Physical Coupling and Applications. *Nat. Mater.* **2019**, *18*, 550−560.

[7] Kum, H. S.; Lee, H.; Kim, S.; Lindemann, S.; Kong, W.; Qiao, K.; Chen, P.; Irwin, J.; Lee, J. H.; Xie, S.; Subramanian, S.; Shim, J.; Bae, S.-H.; Choi, C.; Ranno, L.; Seo, S.; Lee, S.; Bauer, J.; Li, H.; Lee, K.; Robinson, J. A.; Ross, C. A.; Schlom, D. G.; Rzchowski, M. S.; Eom, C.-B.; Kim, J. Heterogeneous Integration of Single-Crystalline Complex-Oxide Membranes. *Nature* **2020**, *578*, 75−81.

[8] Bae, S.-H.; Lu, K.; Han, Y.; Kim, S.; Qiao, K.; Choi, C.; Nie, Y.; Kim, H.; Kum, H. S.; Chen, P.; Kong, W.; Kang, B.-S.; Kim, C.; Lee, J.; Baek, Y.; Shim, J.; Park, J.; Joo, M.; Muller, D. A.; Lee, K.; Kim, J. Graphene-Assisted Spontaneous Relaxation towards Dislocation-Free Heteroepitaxy. *Nat. Nanotechnol.* **2020**, *15*, 272−276.

[9] Kim, H.; Lu, K.; Liu, Y.; Kum, H. S.; Kim, K. S.; Qiao, K.; Bae, S.-H.; Lee, S.; Ji, Y. J.; Kim, K. H.; Paik, H.; Xie, S.; Shin, H.; Choi, C.; Lee, J. H.; Dong, C.; Robinson, J. A.; Lee, J.-H.; Ahn, J.-H.; Yeom, G. Y.; Schlom, D. G.; Kim, J. Impact of 2D–3D Heterointerface on Remote Epitaxial Interaction through Graphene. *ACS Nano* **2021**, *15*, 10587−10596.

[10] Han, Y.; Li, M.-Y.; Jung, G.-S.; Marsalis, M. A.; Qin, Z.; Buehler, M. J.; Li, L.-J.; Muller, D. A. Sub-Nanometre Channels Embedded in Two-Dimensional Materials. *Nat. Mater.* **2018**, *17*, 129−133.

[11] Hÿtch, M. J.; Snoeck, E.; Kilaas, R. Quantitative Measurement of Displacement and Strain Fields from HREM Micrographs. *Ultramicroscopy* **1998**, *74*, 131−146.

Part II

Freestanding Complex-Oxide Membrane Growth and Transfer *via* Sacrificial Interlayer for Emergent Multiferroics

Chapter 3

Efficient Chemical Lift-Off of Complex-Oxide Membrane Assisted by Strained Layer

Recent developments in graphene-based epitaxy and its layer transfer techniques allow for generating a wide range of freestanding complex oxide membranes with high-crystallinity including perovskite, spinel, and garnet. Such single-crystalline complex-oxide membranes can be easily stacked to form unique material systems, where structurally and chemically incompatible materials are interfaced with each other. Thus, material spectrum can be greatly expanded to explore new physical phenomena by creating the artificial heterostructures as well as to enhance material properties by avoiding the substrate clamping effect. However, it is limited to achieve high yield of exfoliated perovskite membrane in this approach due to the challenges of protecting graphene interlayer especially while such film growth in harsh plasma environment of PLD at high temperature. Here, we investigate chemical lift-off of perovskite membranes *via* water-soluble sacrificial interlayer of $Sr_3Al_2O_6$ (SAO), where an additional strained metal layer is introduced on top of membrane surface to expedite peeling process by applying strain at the interface and to generate a large-area membrane supported by metal layer. Also, we demonstrate that a freestanding form of self-assembled $BiFeO_3$-$CoFe_2O_4$ (BFO-CFO) nanocomposites can be formed in the same manner, which is expected to exhibit significantly improved magnetoelectric coupling at the interphases of ferroelectric perovskite of BFO and ferrimagnetic spinel of CFO.

3.1 Introduction

Recent developments in graphene-based epitaxy, which is called remote epitaxy, and its epitaxial layer transfer techniques allow for producing a wide range of freestanding membranes with high-crystallinity.[1-7] This concept has been primarily demonstrated for expensive group III-V and III-N materials with particular emphasis on recycling costly wafers by introducing reusable graphene-coated platforms.[1-4,6-7] At the same time, complex-oxides have also garnered significant interest in their remote epitaxy based on recently reported design rule that polarity or ionicity of substrate materials strongly governs a distant atomic interaction between the substrate and epitaxial layer across graphene.[2] In other words, complex-oxides are suggested to be ideal candidates for remote epitaxy due to their noticeably high ionic character, thereby depending less on the precise control of number of graphene layers. As a result, it was recently published that remote epitaxy enables generating high-quality complex-oxide membranes including perovskite, spinel, and garnet, where freestanding membrane is not clamped by substrate, thus leading to superior material properties such as piezoelectric and magnetostrictive responses in comparison with the counterpart film bound to substrate.[5]

In general, graphene-based lift-off of complex-oxide membranes is advantageous over their chemical lift-off, which is the other archetypal epitaxial layer transfer technique, in terms of the release rate of membrane, universality of approach, and need for post-release refurbishment of substrate.[3] However, we found this method is not favorable to be applied to complex-oxides that specifically require relatively high growth temperature when using PLD technique in Figure 3-1. For example, an optimal growth temperature of perovskite materials such as $SrTiO_3$ (STO) and $BaTiO_3$ (BTO) to obtain single-crystalline films *via* PLD is around 700−800 ºC, where graphene is highly susceptible to its degradation by plasma plume during film growth, thus the yield of such

membranes is significantly reduced. Moreover, it is imperative that single-crystalline graphene (*e.g.* SiC-graphene) needs to be used as an interlayer, otherwise it cannot withstand harsh plasma environment of PLD, thereby not allowing high yield exfoliation of remote epitaxially grown complex-oxide films. Therefore, an alternative approach needs to be developed to generate such oxide membranes in a quick and controlled manner.

Revisit to widely used chemical lift-off using a sacrificial buffer layer counts for producing large-area perovskite membranes. Hwang *et al.*[8] has developed a facile method of generating freestanding perovskite membranes using a water-soluble SAO interlayer as described in Figure 3-2. When SAO is grown on STO substrate, it forms a perovskite-like structure with regularly positioned vacancies, which includes discontinuous Al−O networks that are soluble in water. Thus, a variety of freestanding perovskite membranes have been proved to be accessible by simply immersing SAO-included heteroepitaxial films in water to release the layer above SAO although it typically takes several hours to days.[8-12]

In this work, we develop a strained layer-assisted chemical lift-off of perovskite complex-oxide membranes including STO, BTO, and BFO in order to produce membranes more efficiently with higher yield compared to the conventional chemical lift-off technique. Furthermore, this approach is also applied to generating freestanding nanocomposite membranes comprising the ferroelectric perovskite (BFO) and ferrimagnetic spinel (CFO), which are expected to show significantly improved magnetoelectric coupling at their interphases due to the absence of substrate clamping effect.

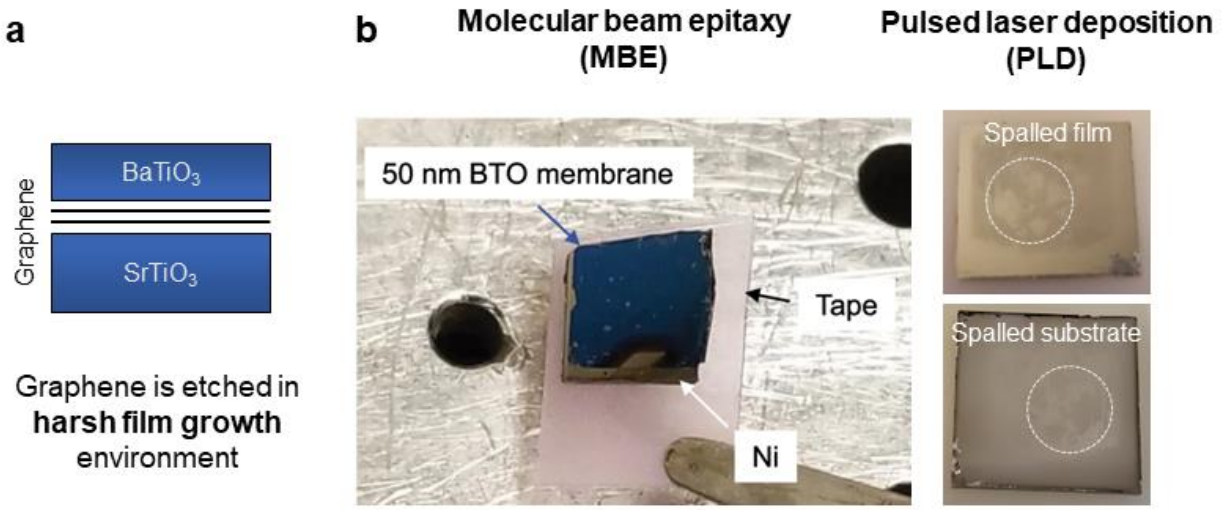

Figure 3-1. Process limitation in perovskite remote epitaxy using pulsed laser deposition (PLD). (a) Schematic diagram of $BaTiO_3$ (BTO) remote epitaxy, where graphene is etched in harsh film growth environment of PLD chamber. (b) Photographs of BTO membrane obtained by remote epitaxy *via* molecular beam epitaxy (MBE) (left) and spalled film and substrate when BTO is remote epitaxially grown *via* PLD (right).

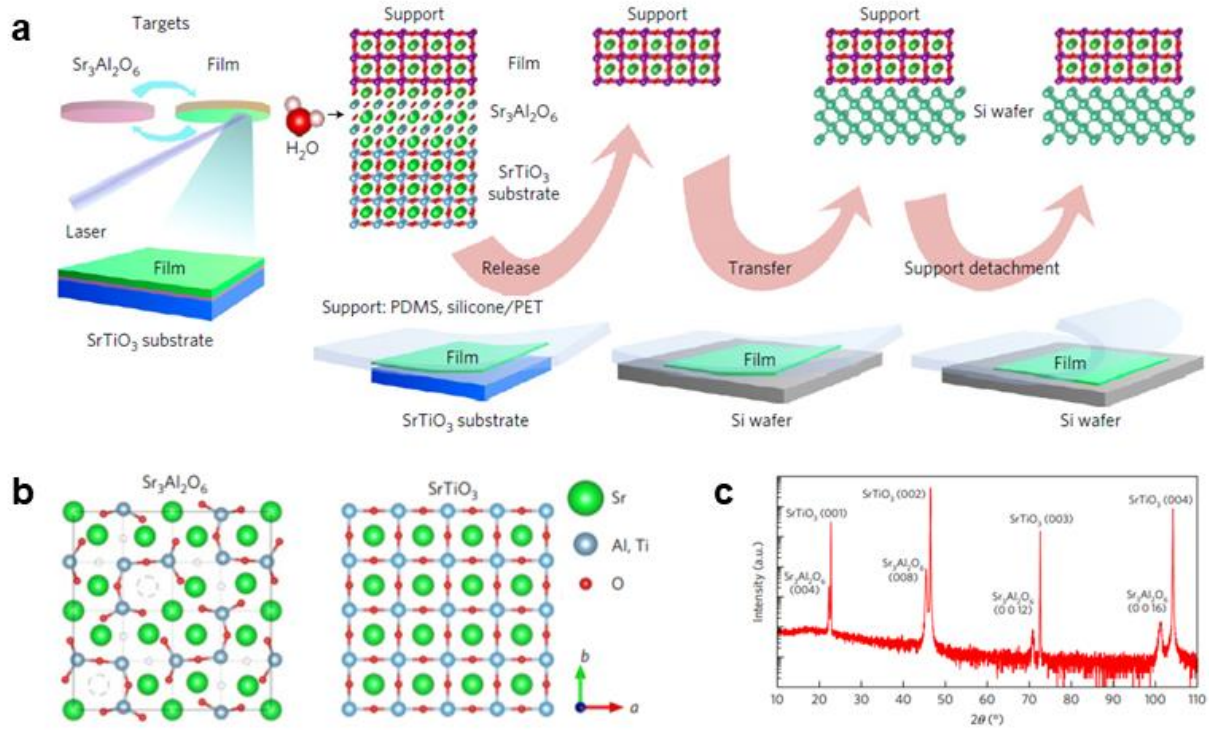

Figure 3-2. (a) Overview of process for oxide membrane growth, release, and transfer. (b) Top 1/4 of $Sr_3Al_2O_6$ (SAO) unit cell projected onto (001) plane (left) and 4 × 4 unit cells of $SrTiO_3$ (STO) crystal structure projected onto (001) plane (right). Dashed circles indicate vacancy sites. (c) X-ray diffraction (XRD) scan of 80 nm SAO film on STO (001) substrate. Redrawn from ref 8.

3.2 Experimental Methods

3.2.1 Sacrificial Buffer and Film Epitaxy

PLD was employed to grow both sacrificial buffer (SAO) and thin films (STO, BFO, BTO, and BFO-CFO) using KrF excimer laser ($\lambda = 248$ nm) with 1.3 J/cm^2 fluence in this work. STO substrates were pre-annealed at an oxygen partial pressure, $p(O_2)$, of 5×10^{-6} Torr for 30 min at a set temperature of 950 °C, where actual substrate temperature was estimated to be ~100 °C lower, to achieve sharp step-and-terrace surfaces. SAO buffer layer was grown first on top of STO substrate prior to active membrane layer growth at a set temperature of 900 °C, $p(O_2)$ of 5×10^{-6} Torr, and pulse rate of 2 Hz using ceramic single-crystal SAO target. SAO thickness measured by cross-sectional TEM was ~30 nm. STO films were directly grown on SAO buffer at a set temperature of 850 °C, $p(O_2)$ of 50 mTorr, and pulse rate of 10 Hz using ceramic single-crystal STO target. BFO films were directly grown on SAO buffer at a set temperature of 750 °C, $p(O_2)$ of 100 mTorr, and pulse rate of 10 Hz using ceramic single-crystal BFO target. BTO films were directly grown on SAO buffer at a set temperature of 900 °C, $p(O_2)$ of 100 mTorr, and pulse rate of 10 Hz using ceramic single-crystal BTO target. Thicknesses of all three perovskite films here were ~150 nm. BFO-CFO nanocomposite films were grown either on SAO buffer or on ~5 nm thick STO-covered SAO buffer at a set temperature of 700 °C and $p(O_2)$ of 5 mTorr using ceramic single-crystal BFO and CFO targets. Nanocomposites here were self-assembled *via* combinatorial growth approach by alternately ablating separate BFO and CFO targets to produce submonolayer thicknesses of each material during each cycle. The ratio of number of pulses applied to the respective targets was BFO:CFO = 420:60 per cycle, and 100 cycles were performed to obtain

~100 nm thick composite layers. After all layer growths, films were cooled down to room temperature at a rate of 20 °C/min maintaining the same oxygen atmosphere.

3.2.2 Chemical Lift-Off of Epitaxial Layer

After all film growths including SAO sacrificial layer using PLD, a Ni stressor layer was deposited on top *via* plasma sputtering with using commercially purchased Ni target with 99.99% purity. A thin Ti adhesive layer of ~20 nm was deposited using electron-beam evaporation before depositing Ni stressor. Ni was sputtered at a chamber pressure of 2×10^{-3} Torr with 9.5 sccm of Ar flow, with a growth rate of approximately 2 μm/h. TRT as a handling layer was then attached onto Ni/Ti/film/SAO/substrate stack that was immersed into de-ionized (DI) water at room temperature to dissolve SAO interlayer. Separated TRT/Ni/Ti/membrane stack was then transferred onto substrate of interest, followed by TRT removal at 120−150 °C on hot plates and metal layer etching in $FeCl_3$ solution (for removing both Ni and Ti) or Ni etchants (for removing only Ni), resulting in complex-oxide membrane-integrated substrate. Detailed process is illustrated in Appendix B.

3.2.3 Characterization of 3D Membrane

Morphology and crystallinity of top surface or exfoliated surface of complex-oxide membranes were analyzed by ZEISS Merlin high-resolution SEM equipped with an EBSD detector. Crystallinity of membranes was also characterized by high-resolution X-ray diffraction

(XRD), using a Rigaku SmartLab high-resolution diffractometer with Cu $K\alpha_1$ radiation (λ = 1.5406 Å) as X-ray source and an incident beam Ge-(220) double-bounce monochromator.

3.3 Results and Discussion

3.3.1 Strained Layer-Assisted Chemical Lift-Off of Perovskite Membranes

To generate perovskite membranes *via* chemical lift-off method, we find an optimal growth condition of SAO interlayer on top of STO substrate using PLD. As SAO is a hygroscopic oxide, which is easily degraded by atmospheric humidity on minutes timescale, any capping layer must be grown on SAO layer in the same chamber to avoid its early degradation. Thus, we first attempt to grow STO, which is lattice-matched to SAO interlayer, not only as a capping layer but also as an active membrane layer as illustrated in Figure 3-3. Top surface of STO layer is smooth under SEM, and high-resolution XRD reveals that a sharp SAO peak is situated right next to a STO substrate peak, which indicates the lattice of SAO is more or less matched to that of STO, showing a good agreement with XRD scan in ref 8. Upper STO layer is then separated from substrate by dissolving SAO buffer in DI water. Here, we introduce metal stressor layer of Ni and Ti, which work as an actual stressor layer and adhesive layer respectively, on top of STO membrane layer in order to expedite peeling process by applying strains to the STO/SAO interface. TRT is added to support this thin film layers, and a whole stack is then immersed in DI water. After few hours, STO film is detached from substrate, indicating SAO layer is completely removed by water and it eventually generates the membrane of STO. Released STO surface is clean and flat as shown in photo and SEM image in Figure 3-4, and it exhibits almost a 100 % exfoliation yield of a cm^2-sized membrane, which is sufficient to make a functional device out of it. Using this new chemical lift-off approach assisted by a strained layer, we expect that wafer-scale membrane can be produced in a reasonably short peeling process.

In addition, high-quality BFO and BTO, which are the representative ferroelectric perovskite complex-oxides, are successfully grown on top of water-soluble SAO layer *via* PLD technique. A single-crystallinity of top film surface is verified by single-colored EBSD mapping result and well-identified high-resolution XRD peaks of BFO and BTO phases for the respective films (Figure 3-5). However, their film surfaces shown in SEM images (Figure 3-5a and 3-5d) are slightly rougher than that of STO membrane layer (Figure 3-3b) due to the lattice mismatch between the active layer and substrate, which leads to more broadened XRD peaks. Around cm^2-sized membranes of both BFO and BTO are also released well with smooth exfoliated surfaces in DI water when metal stressor (Ni/Ti) is used as a support layer as illustrated in photos of Figure 3-6. Under SEM, both membranes show flat morphologies on exfoliated surface although several tiny holes are observed, which may be due to their lattice mismatch to SAO buffer and STO substrate. As a lattice mismatch between BTO and STO is higher than that between BFO and STO, more defects are found on BTO film surface than on BFO film surface.

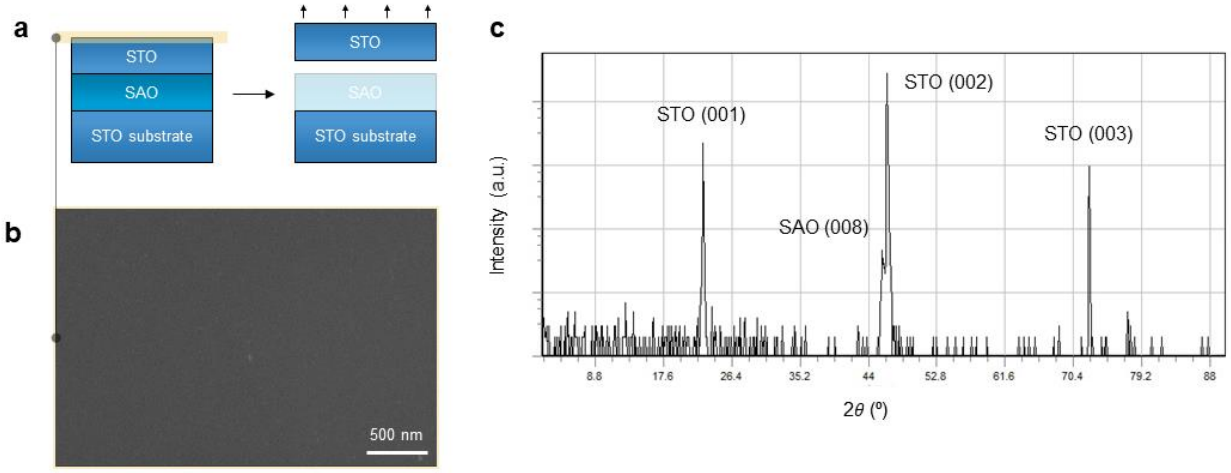

Figure 3-3. (a) Conceptual schematic diagrams of growing and releasing STO membrane *via* sacrificial SAO interlayer. (b) Top-view SEM image and (c) XRD scan of STO film grown on SAO/STO.

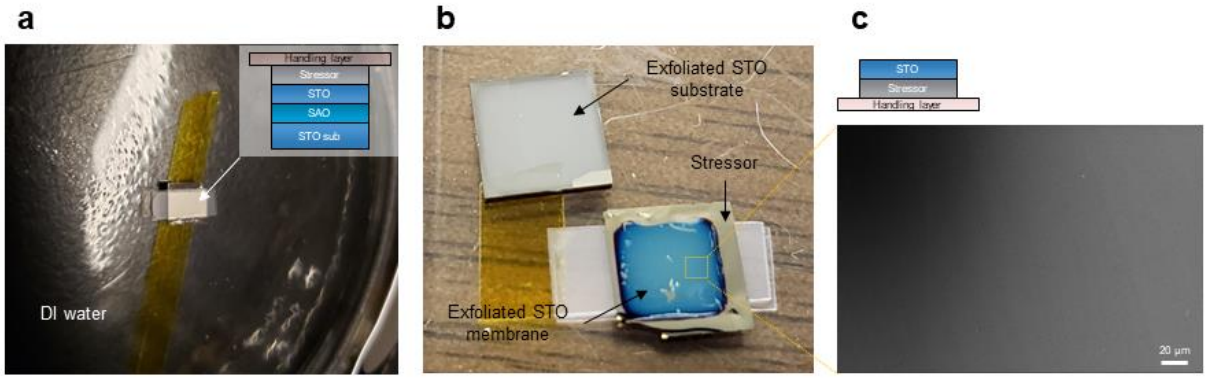

Figure 3-4. Photographs exhibiting (a) STO membrane peeling process by dissolving SAO interlayer in de-ionized (DI) water and (b) exfoliated STO membrane and substrate. (c) Top-view SEM image of exfoliated surface of STO membrane. Insets in Figure 3-4a and 3-4c present schematics for thermal release tape (TRT)/Ni/Ti/STO/SAO/STO and STO/Ti/Ni/TRT stacks before and after peeling process, respectively.

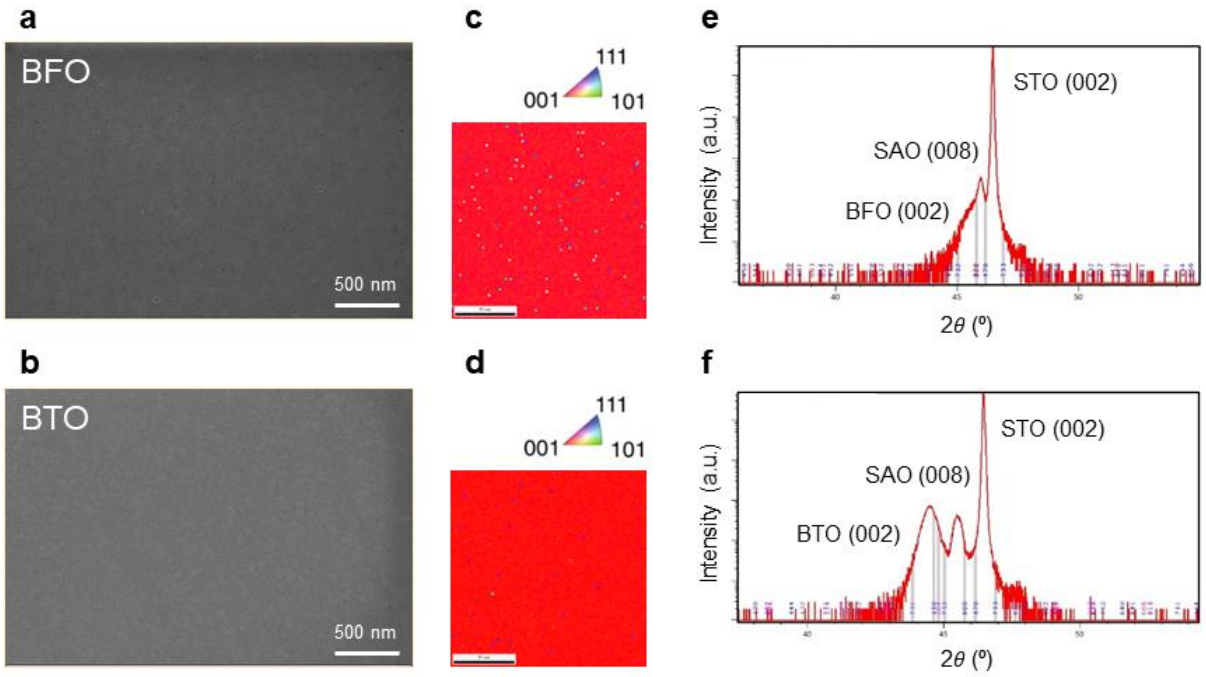

Figure 3-5. (a,b) Top-view SEM images, (c,d) EBSD maps, and (e,f) XRD scans of (a,c,e) $BiFeO_3$ (BFO) and (b,d,f) BTO membranes grown on SAO/STO.

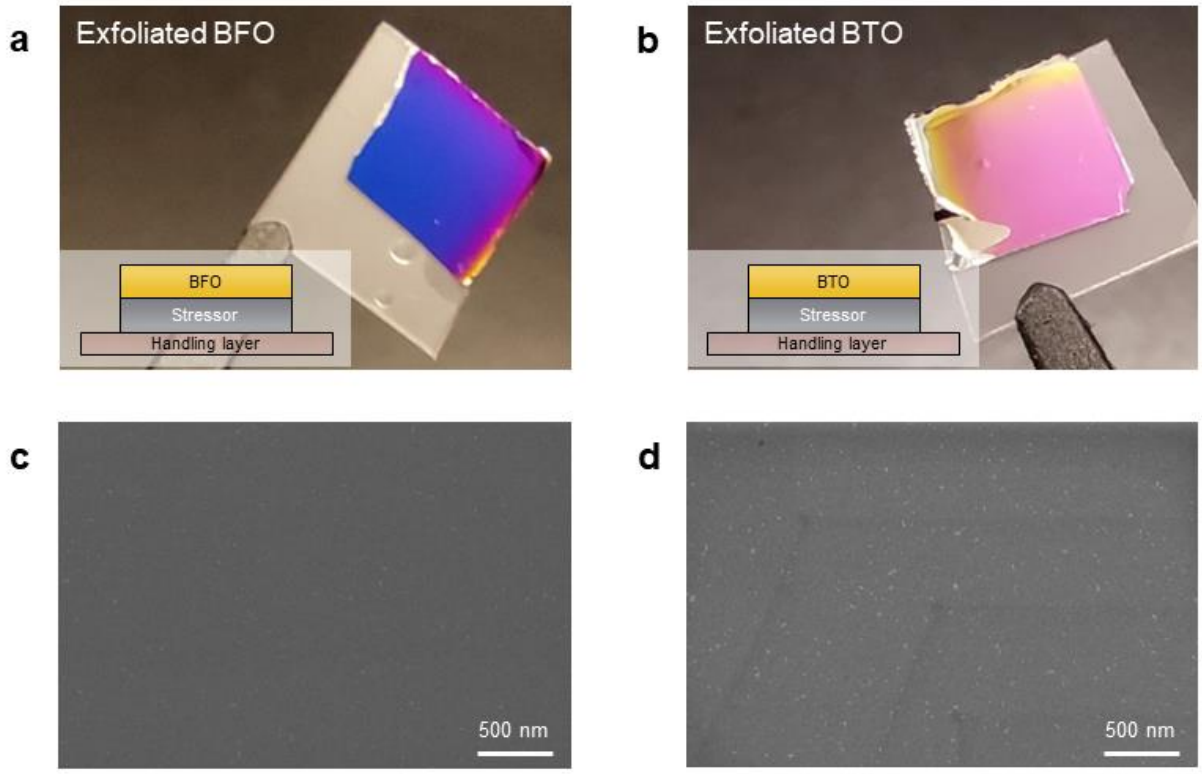

Figure 3-6. (a,b) Photographs and (c,d) top-view SEM images of exfoliated surfaces of (a,c) BFO and (b,d) BTO membranes. Insets in Figure 3-6a and 3-6b present schematics for membrane (BFO and BTO)/Ti/Ni/TRT stacks after peeling process, respectively.

3.3.2 Self-Assembled $BiFeO_3$-$CoFe_2O_4$ Nanocomposite Membrane Growth and Transfer

Our new approach is further extended to chemical lift-off of self-assembled nanocomposite membranes in order to generate substrate clamping-free multiferroic composites, which may show more enhanced magnetoelectric coupling effect. We start with standard multiferroic nanocomposites of BFO-CFO, which consist of ferrimagnetic CFO pillars surrounded by

ferroelectric BFO matrix. As described in Figure 3-7, it shows a clear difference in composite morphology depending on whether film is grown on bare SAO or ultrathin STO-coated SAO layer. When it is directly formed on SAO buffer, it still shows a composite-like morphology including CFO pillars and BFO matrix around them, but there is a noticeable amount of grooves on BFO specifically between some of CFO pillars, suggesting the alignment of CFO pillars is not organized well. Thus, it is difficult to identify CFO peak in XRD scan probably due to such poorly defined structure or randomly oriented pillars. However, when additional layer of STO a few nm thick is embedded in between the nanocomposite layer and SAO buffer, BFO-CFO nanocomposites are formed with a better morphology and more well-defined interfaces between the CFO pillars and BFO matrix in comparison with the former structure grown on bare SAO. XRD result reflects improved morphology by showing a clear peak of CFO and narrower peaks of BFO and SAO. Therefore, ultrathin STO buffer allows to provide a flatter surface for better growth of BFO-CFO on top, but it does not clamp the upper layer like a substrate due to its thickness of few unit cells.

Few mm^2-sized membranes of BFO-CFO nanocomposite are also released well along with ultrathin STO layer on top in a similar manner used for perovskite membrane exfoliation discussed in Chapter 3.3.1. We notice here that exfoliated membrane shows many wrinkles when relatively thin metal stressor layer is introduced to be a support layer, while membrane quality is significantly improved by adding PMMA support between the stressor and TRT handling layer as described in Figure 3-8. It indicates that a support layer including metal stressor must be over certain thickness to work well for maintaining a flat and clean surface of exfoliated membrane, otherwise more defects and wrinkles can be introduced into membrane during peeling process, which is detrimental to achieve sharp interface between the transferred membrane and foreign substrate/layer of interest.

We also investigate a substrate orientation dependence of nanocomposite morphology in Figure 3-9. When STO substrates with three different crystal orientations of (100), (110), and (111) are used for chemical lift-off of BFO-CFO nanocomposites, it is expected to obtain composites grown along the respective substrate orientations even through SAO interlayer. As a result of growing BFO-CFO/STO (~5 nm)/SAO on each substrate simultaneously with the same growth condition, only STO (100) case exhibits a good morphology, while STO (110) and (111) cases show a poorly merged BFO matrix with almost randomly oriented CFO pillars. Here, we can clearly see a shape difference of CFO pillars in each composite depending on substrate orientation as similar to the literature showing that squared, striped, and triangular CFO pillars are formed in BFO-CFO composites grown on bare STO (100), (110), and (111) respectively[13]. This indicates that substrate information is transferred well to top BFO-CFO composite even through STO/SAO buffer, which is expected to change aspect ratio of nanostructures and magnetic anisotropy of nanocomposites. Thus, it shows a great potential of controlling material properties by simply changing substrate orientation although it requires further growth optimization to achieve better composite morphologies when grown on STO (110) and (111).

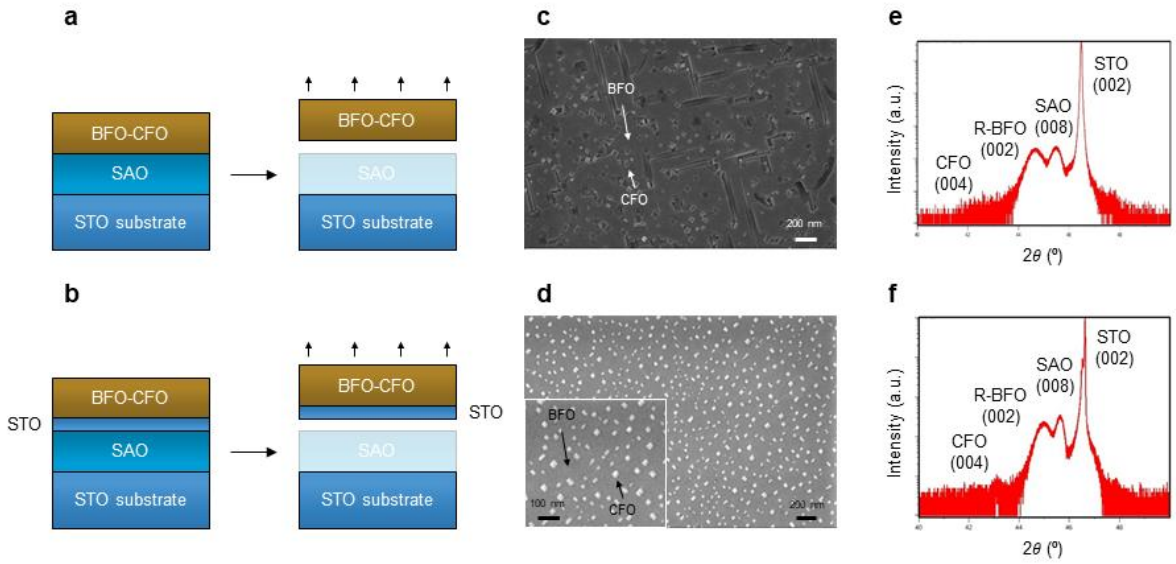

Figure 3-7. (a,b) Schematic diagrams, (c,d) top-view SEM images, and (e,f) XRD scans of BFO-$CoFe_2O_4$ (CFO) nanocomposite membranes grown on (a,c,e) SAO/STO and (b,d,f) ultrathin STO-coated SAO/STO.

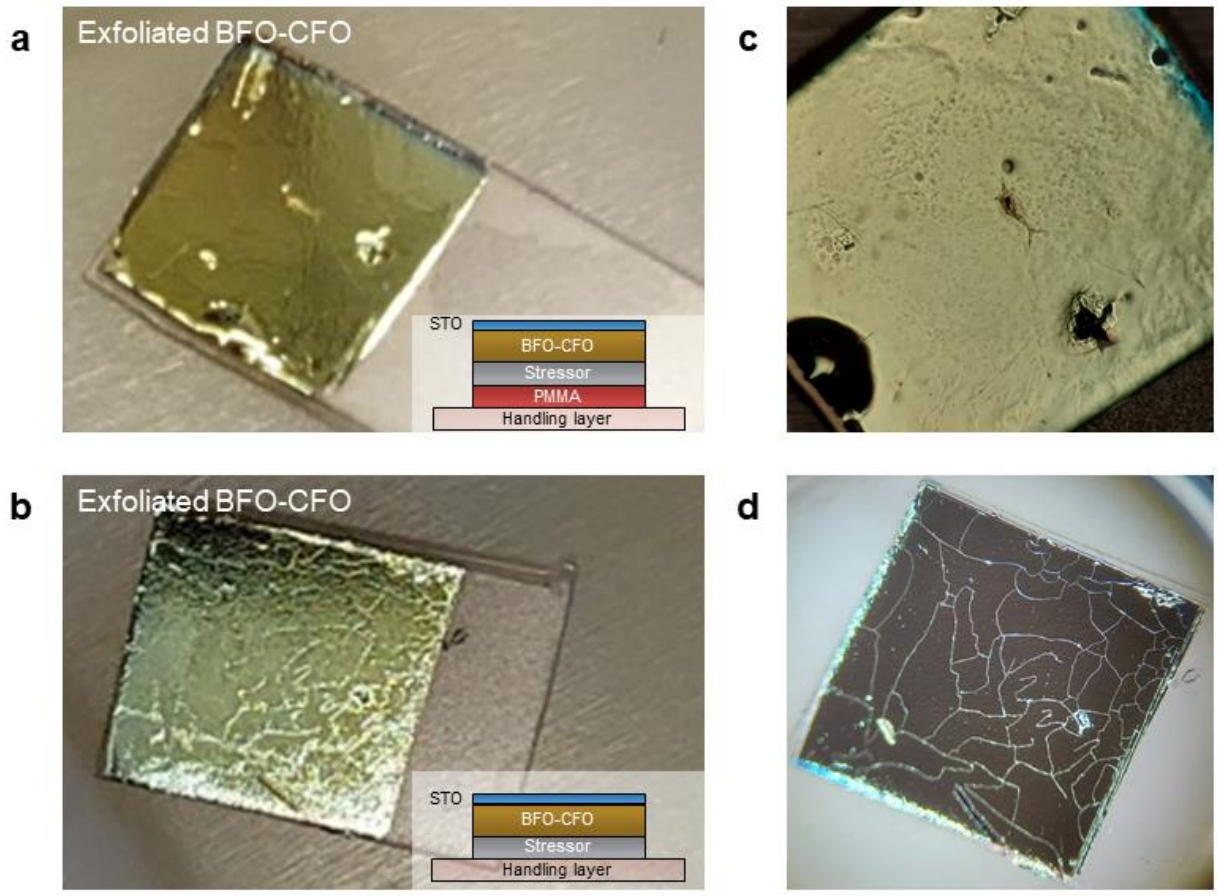

Figure 3-8. (a,b) Photographs and (c,d) optical microscopy images of exfoliated surfaces of ultrathin STO/BFO-CFO membranes by (a,c) metal stressor/poly(methyl methacrylate) (PMMA) support and (b,d) only metal stressor. Insets in Figure 3-8a and 3-8b present schematics for exfoliated membrane of STO/BFO-CFO/Ti/PMMA/TRT and STO/BFO-CFO/Ti/TRT stacks, respectively.

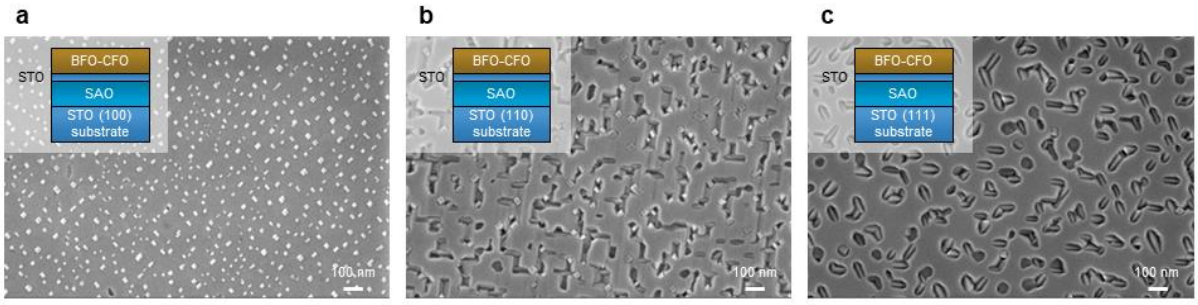

Figure 3-9. Top-view SEM images of BFO-CFO nanocomposites grown on ultrathin STO-coated (a) SAO/STO (100), (b) SAO/STO (110), and (c) SAO/STO (111). Insets in Figure 3-9a, 3-9b, and 3-9c present schematics for BFO-CFO/STO/SAO stacks grown on STO (100), (110), and (111) substrates, respectively.

3.3.3 Multiferroic Properties of $BiFeO_3$-$CoFe_2O_4$ Nanocomposite Membrane

Lastly, magnetic hysteresis loops of BFO-CFO nanocomposite are compared before and after its exfoliation in Figure 3-10. When the composite is bound to the substrate, a prominent magnetic anisotropy of CFO phase is observed along out-of-plane direction, which is typically obtained in such vertically aligned self-assembled nanocomposites[13]. Here, the saturated magnetization (M_s) values are ~200 emu/cm^3 in both directions, but the coercive field (H_c) is ~100 Oe for in-plane and ~1000 Oe for out-of-plane direction. However, it exhibits relatively isotropic magnetic behavior after peeling off BFO-CFO/STO (~5 nm) layer from substrate, where H_c values for both orientations are estimated to be ~200 Oe. This result implies that effective strain relaxation of composite film is achieved while its exfoliation, which leads to a significant reduction in

anisotropy. Interestingly, ultrathin STO layer does not impose any clamping effect on the overlying nanocomposite membrane, which allows to accomplish not only a better morphology of nanocomposite but also a clamping-free membrane with using such STO buffer. Amrillah *et al.* reported that BFO-CFO composite also shows an isotropic magnetic behavior when grown on 2D layered substrate *via* vdW epitaxy, where magnetoelectric (ME) coupling is noticeably enhanced due to the absence of substrate clamping.[14] Therefore, it is expected to see more remarkable ME coupling effect in our freestanding BFO-CFO membranes, which provides an attractive pathway for exploring emergent multiferroics.

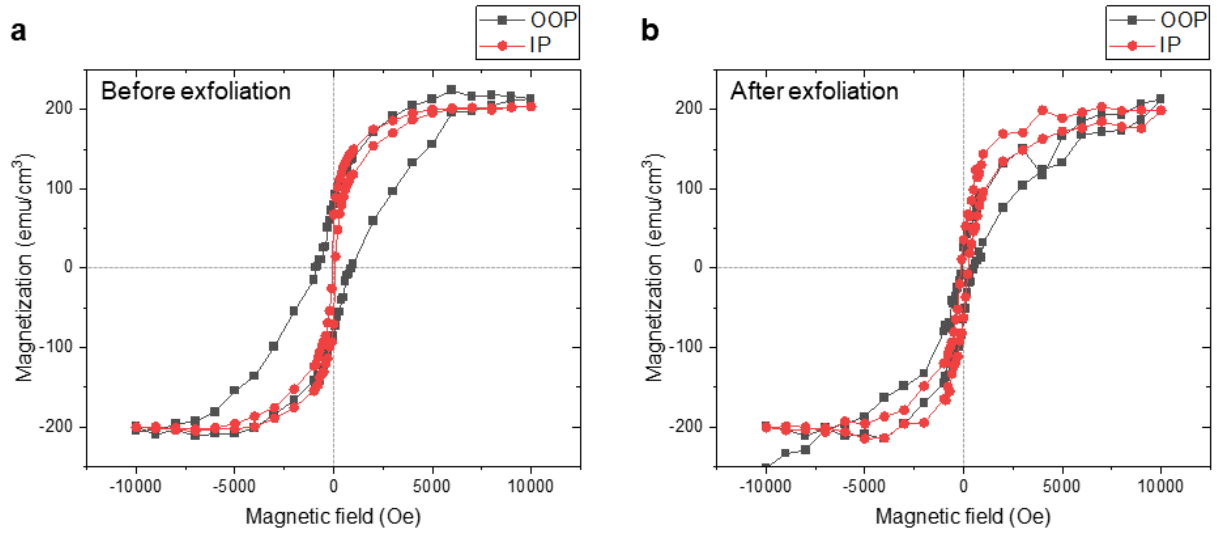

Figure 3-10. M–H hysteresis loops of BFO-CFO nanocomposite along out-of-plane (OOP) and in-plane (IP) directions (a) before and (b) after its exfoliation from SAO/STO (100) substrate.

3.4 Conclusions

In summary, we investigate chemical lift-off of perovskite (STO, BFO, and BTO) and multiferroic nanocomposite (BFO-CFO) membranes *via* water-soluble SAO interlayer, where an additional strained metal layer is introduced on top of membrane surface to expedite peeling process by applying strain at the interface and to generate a large-area membrane supported by metal layer. In this manner, material spectrum of complex-oxide thin films can be greatly expanded to explore new physical phenomena by creating the artificial heterostructures as well as to enhance material properties by avoiding the substrate clamping effect. Freestanding BFO-CFO nanocomposite membranes are also expected to exhibit significantly improved magnetoelectric coupling at the interphases of ferroelectric perovskite of BFO and ferrimagnetic spinel of CFO due to the absence of substrate clamping effect.

References

[1] Kim, Y.; Cruz, S. S.; Lee, K.; Alawode, B. O.; Choi, C.; Song, Y.; Johnson, J. M.; Heidelberger, C.; Kong, W.; Choi, S.; Qiao, K.; Almansouri, I.; Fitzgerald, E. A.; Kong, J.; Kolpak, A. M.; Hwang, J.; Kim, J. Remote Epitaxy through Graphene Enables Two-Dimensional Material-Based Layer Transfer. *Nature* **2017**, *544*, 340−343.

[2] Kong, W.; Li, H.; Qiao, K.; Kim, Y.; Lee, K.; Nie, Y.; Lee, D.; Osadchy, T.; Molnar, R. J., Gaskill, D. K.; Myers-Ward, R. L.; Daniels, K. M.; Zhang, Y.; Sundram, S.; Yu, Y.; Bae, S.-H.; Rajan, S.; Shao-Horn, Y.; Cho, K.; Ougazzaden, A.; Grossman, J. C.; Kim, J. Polarity Governs Atomic Interaction through Two-Dimensional Materials. *Nat. Mater.* **2018**, *17*, 999−1004.

[3] Kum, H.; Lee, D.; Kong, W.; Kim, H.; Park, Y.; Kim, Y.; Baek, Y.; Bae, S.-H.; Lee, K.; Kim, J. Epitaxial Growth and Layer-Transfer Techniques for Heterogeneous Integration of Materials for Electronic and Photonic Devices. *Nat. Electron.* **2019**, *2*, 439−450.

[4] Bae, S.-H.; Kum, H.; Kong, W.; Kim, Y.; Choi, C.; Lee, B.; Lin, P.; Park, Y.; Kim, J. Integration of Bulk Materials with Two-Dimensional Materials for Physical Coupling and Applications. *Nat. Mater.* **2019**, *18*, 550−560.

[5] Kum, H. S.; Lee, H.; Kim, S.; Lindemann, S.; Kong, W.; Qiao, K.; Chen, P.; Irwin, J.; Lee, J. H.; Xie, S.; Subramanian, S.; Shim, J.; Bae, S.-H.; Choi, C.; Ranno, L.; Seo, S.; Lee, S.; Bauer, J.; Li, H.; Lee, K.; Robinson, J. A.; Ross, C. A.; Schlom, D. G.; Rzchowski, M. S.; Eom, C.-B.; Kim, J. Heterogeneous Integration of Single-Crystalline Complex-Oxide Membranes. *Nature* **2020**, *578*, 75−81.

[6] Bae, S.-H.; Lu, K.; Han, Y.; Kim, S.; Qiao, K.; Choi, C.; Nie, Y.; Kim, H.; Kum, H. S.; Chen, P.; Kong, W.; Kang, B.-S.; Kim, C.; Lee, J.; Baek, Y.; Shim, J.; Park, J.; Joo, M.; Muller, D. A.; Lee, K.; Kim, J. Graphene-Assisted Spontaneous Relaxation towards Dislocation-Free Heteroepitaxy. *Nat. Nanotechnol.* **2020**, *15*, 272−276.

[7] Kim, H.; Lu, K.; Liu, Y.; Kum, H. S.; Kim, K. S.; Qiao, K.; Bae, S.-H.; Lee, S.; Ji, Y. J.; Kim, K. H.; Paik, H.; Xie, S.; Shin, H.; Choi, C.; Lee, J. H.; Dong, C.; Robinson, J. A.; Lee, J.-H.; Ahn, J.-H.; Yeom, G. Y.; Schlom, D. G.; Kim, J. Impact of 2D–3D Heterointerface on Remote Epitaxial Interaction through Graphene. *ACS Nano* **2021**, *15*, 10587−10596.

[8] Lu, D.; Baek, D. J.; Hong, S. S.; Kourkoutis, L. F.; Hikita, Y.; Hwang, H. Y. Synthesis of Freestanding Single-Crystal Perovskite Films and Heterostructures by Etching of Sacrificial Water-Soluble Layers. *Nat. Mater.* **2016**, *15*, 1255−1260.

[9] Dong, G.; Li, S.; Yao, M.; Zhou, Z.; Zhang, Y.-Q.; Han, X.; Luo, Z.; Yao, J.; Peng, B.; Hu, Z.; Huang, H.; Jia, T.; Li, J.; Ren, W.; Ye, Z.-G.; Ding, X.; Sun, J.; Nan, C.-W.; Chen, L.-Q.; Li, J.; Liu, M. Super-Elastic Ferroelectric Single-Crystal Membrane with Continuous Electric Dipole Rotation. *Science* **2019**, *366*, 475−479.

[10] Ji, D.; Cai, S.; Paudel, T. R.; Sun, H.; Zhang, C.; Han, L.; Wei, Y.; Zang, Y.; Gu, M.; Zhang, Y.; Gao, W.; Huyan, H.; Guo, W.; Wu, D.; Gu, Z.; Tsymbal, E. Y.; Wang, P.; Nie, Y.; Pan, X. Freestanding Crystalline Oxide Perovskites Down to the Monolayer Limit. *Nature* **2019**, *570*, 87−90.

[11] Hong, S. S.; Gu, M.; Verma, M.; Harbola, V.; Wang, B. Y.; Lu, D.; Vailionis, A.; Hikita, Y.; Pentcheva, R.; Rondinelli, J. M.; Hwang, H. Y. Extreme Tensile Strain States in $La_{0.7}Ca_{0.3}MnO_3$ Membranes. *Science* **2020**, *368*, 71−76.

[12] Peng, B.; Peng, R.-C.; Zhang, Y.-Q.; Dong, G.; Zhou, Z.; Zhou, Y.; Li, T.; Liu, Z.; Luo, Z.; Wang, S.; Xia, Y.; Qiu, R.; Cheng, X.; Xue, F.; Hu, Z.; Ren, W.; Ye, Z.-G.; Chen, L.-Q.; Shan, Z.; Min, T.; Liu, M. Phase Transition Enhanced Superior Elasticity in Freestanding Single-Crystalline Multiferroic $BiFeO_3$ Membranes. *Sci. Adv.* **2020**, *6*, eaba5847.

[13] Wang, Z.; Li, Y.; Viswan, R.; Hu, B.; Harris, V. G.; Li, J.; Viehland, D. Engineered Magnetic Shape Anisotropy in $BiFeO_3$-$CoFe_2O_4$ Self-Assembled Thin Films. *ACS Nano* **2013**, *7*, 3447−3456.

[14] Amrillah, T.; Bitla, Y.; Shin, K.; Yang, T.; Hsieh, Y.-H.; Chiou, Y.-Y.; Liu, H.-J.; Do, T. H.; Su, D.; Chen, Y.-C.; Jen, S.-U.; Chen, L.-Q.; Kim, K. H.; Juang, J.-Y.; Chu, Y.-H. Flexible Multiferroic Bulk Heterojunction with Giant Magnetoelectric Coupling *via* van der Waals Epitaxy. *ACS Nano* **2017**, *11*, 6122−6130.

Part III

Self-Assembled Block Copolymer Thin Films

Templating Hybrid Nanostructures

Chapter 4

Resolving Triblock Terpolymer Morphologies by Vapor-Phase Infiltration

The spontaneous formation of well-organized 3D nanostructures from self-assembled block copolymers (BCPs) holds promise for nanofabrication and lithography. The addition of a third block to BCPs provides access to a plethora of 3D geometries, but it remains difficult to resolve the geometry of such "three-color" structures when there is low contrast between the polymeric components at length scales of a few nanometers. Here, we apply vapor-phase infiltration synthesis to a silicon-containing triblock terpolymer, poly(1,1-dimethylsilacyclobutane-*b*-styrene-*b*-lactide) (PDMSB-*b*-PS-*b*-PLA or DSL) to distinguish the 3D microdomain morphologies of the two organic blocks, PLA and PS. Selective infiltration of ZnO within the PLA microdomains reveals morphologies consisting of three-color lamellae or lamellae combined with vertically aligned core-shell cylinders, depending on the volume fractions of each block. The infiltration produces ZnO nanoparticles throughout the 260 nm thickness of the DSL film, generating 3D nanocomposites containing ZnO and SiO_x. These results provide a strategy for synthesizing multicomponent 3D nanostructures as well as visualizing the phase behavior of multiblock copolymers. This work was published in ref 1.

4.1 Introduction

3D nanofabrication is essential for producing a host of useful materials and structures for applications such as electronic devices, nanoporous membranes, and functionalized surfaces.[2–7] Self-assembly of BCP thin films in particular offers an efficient route to produce a variety of 3D nanostructures, taking advantage of its simple sequence of processing steps.[8–15] Compared with diblock copolymers, triblock and multiblock polymers can produce nanostructures with greater structural diversity and additional chemical functionalities,[16–21] and there has been an increasing emphasis on understanding their self-assembly and 3D morphologies.[22–26]

However, it is challenging to resolve the morphologies of 3D BCPs comprising more than two polymeric components unless there is good contrast between the microdomains, for example, a contrast in density, chemical composition, or reactivity. Block-selective etching followed by plan-view or cross-sectional imaging using SEM is commonly used to characterize BCP morphologies, but the organic blocks are often difficult to distinguish.[24,27] X-ray scattering is used for 3D structural analysis, but it requires a scattering contrast between the blocks, for example, the presence of metal or Si in one block,[14,24] and analysis of triblock morphologies (beyond measuring the periodicity) requires modeling the structure factor.

Vapor-phase infiltration (VPI) refers to variations of *ex situ* material hybridization techniques based on atomic layer deposition (ALD) including multipulse infiltration,[28] sequential vapor infiltration,[29] and sequential infiltration synthesis,[30] where vapor-phase inorganic precursors perfuse the polymer matrix to generate unique organic−inorganic hybrids with improved material properties. When applied to a self-assembled BCP, it can greatly enhance the scattering contrast and the etch resistance between blocks by selectively incorporating inorganic material such as ZnO,

TiO_2, or Al_2O_3 into specific microdomains.[28–38] The infiltration process proceeds *via* sorption (diffusion) and a block-selective reaction of vapor-phase organometallic precursors into the polymer blocks with suitable reactive moieties to generate infused inorganic materials within the target BCP microdomains.[39–40] The hybrid nanocomposite thus formed can also be converted to an inorganic nanostructure inheriting the original structure of the polymer microdomains,[35,37] not only producing various functional nanostructures in a simple process but also enabling all-organic BCP morphologies to be fully resolved.[32] ALD of metal oxide precursors into cylinder- and gyroid-forming BCPs has been used to generate 1D and 3D nanostructures for a broad variety of nanotechnologies such as gas sensors, solar cells, photocatalysts, and pattern transfer masks.[15,33,36,41–43]

While the majority of the reports exploiting infiltration synthesis of BCPs are focused on diblock copolymers, the process is also applicable to BCPs containing three or more blocks such as triblock terpolymers (TBTPs).[38] In this work, we demonstrate the infiltration of inorganic species into PDMSB-*b*-PS-*b*-PLA (DSL), a silicon-containing TBTP with two organic blocks, PS and PLA. Our previous study of one composition of DSL reported the formation of microdomains consisting of core-shell cylinders perpendicular to perforated lamellae, based on SEM and grazing-incidence small-angle X-ray scattering (GISAXS) characterization.[24] The PDMSB was clearly resolved but it was difficult to differentiate between the PLA and the PS blocks. In this work, we demonstrate the effects of ZnO infiltration into a series of DSL compositions that includes both lamellar and lamellar plus hexagonal cylinder morphologies. We first investigate the phase behavior of four DSLs with different volume fractions of each block and then show that infiltration synthesis introduces ZnO into the PLA microdomains. These results not only reveal the

microdomain morphologies of the DSL but also demonstrate the formation of nanocomposites with ZnO, silica, and organic components.

4.2 Experimental Methods

4.2.1 Materials and Preparation of PDMSB-*b*-PS-*b*-PLA (DSL) Films

Four linear DSL TBTPs with different volume fractions of each block in Table 4-1 were synthesized *via* the combination of anionic polymerization by sequential addition of monomers and ring opening polymerization using a strong organic base as the catalyst (also called pseudo anionic polymerization). A hydroxyl-terminated poly(1,1-dimethylsilacyclobutane-*b*-styrene) (PDMSB-*b*-PS-OH) was first prepared by the sequential anionic polymerization of DMSB and styrene monomers in various compositions using tetrahydrofuran (THF)/heptane (1:1) as a solvent at −48 °C accompanied by the addition of ethylene oxide. This reaction was terminated using degassed methanol in order to achieve the desired end-functionalized symmetric and asymmetric PDMSB-*b*-PS BCPs. The ring opening polymerization of D,L-lactide was then performed in toluene at 80 °C using PDMSB-*b*-PS-OH as the macroinitiator in the presence of the catalyst triazabicyclodecene (TBD).[44]

DSL films (180−260 nm-thick) were obtained by spin-coating 4 wt % DSL solutions in a mixture of THF and propylene glycol monomethyl ether acetate or PGMEA (THF/PGMEA = 2:1) onto silicon substrates with a native oxide layer. The as-cast film thickness was determined by a spin speed of 3000 rpm and measured using a spectral reflectometer (FilMetrics F20-UV). All the solvents used in this study were purchased from Sigma-Aldrich.

Table 4-1. DSL properties, morphologies, and periods in thin films.

	Molecular weight, M_n [kg/mol]	Dispersity, M_w/M_n	Composition, $f_{PDMSB}/f_{PS}/f_{PLA}$	Thin film thickness [nm]	Thin film morphology	Period [nm][a)]
DSL-L1	28.4	1.15	0.41/0.40/0.19	180	$Lam_{//}$	21
DSL-L2	25.8	1.12	0.36/0.36/0.28	210	$Lam_{//}$	16
DSL-H1	55.5	1.09	0.25/0.40/0.35	240	$Lam_{//}$-$Hex_{\perp}$	21, 38
DSL-H2	38.4	1.07	0.31/0.53/0.16	260	$Lam_{//}$-$Hex_{\perp}$	17, 35

Lam, alternating lamellae; Hex, hexagonally packed core-shell cylinders; //, lateral alignment; ⊥, vertical alignment; [a)]Estimated from SEM and TEM images; the two values for DSL-H1 and DSL-H2 correspond to the out-of-plane lamellar spacing and the in-plane pore spacing respectively.

4.2.2 Solvent Vapor Annealing of DSL Films

Solvent vapor annealing was carried out using a continuous flow system where separate streams of nitrogen are bubbled through liquid solvents and the flow of each stream is regulated using a mass flow controller (MKS Inc., M100B).[45] As-cast DSL films on substrates were placed inside the glass annealing chamber (volume, ~80 cm^3) tightly sealed by a quartz plate along with a perfluoroelastomer O-ring (Markez Inc., Z1210) and were annealed in a vapor flow of $CHCl_3$ and N_2 for ~1 h at ambient temperature. Solvent vapors of $CHCl_3/N_2$ = 10 sccm:1 sccm were introduced to achieve an optimal swelling ratio of ~2.1 and ~1.9 for DSL-L and DSL-H, respectively, which produced well-ordered DSL morphologies. The inflow tube was connected to a mixer fed by two flow channels: pure N_2 gas (Airgas, Inc., 99.9997% purity) for diluting the vapor pressure of $CHCl_3$ and a solvent bubbler that contained $CHCl_3$. During the deswelling,

swollen films were slowly dried over 10 min by stopping the vapor flow of $CHCl_3$ and N_2 followed by gently detaching the quartz lid from the chamber at room temperature.

4.2.3. ZnO Vapor-Phase Infiltration (VPI) Synthesis in DSL Films

The infiltration synthesis of ZnO was carried out in a commercial ALD system (Cambridge Nanotech, Savannah S100) at 85 °C using diethylzinc (DEZ) and trimethylaluminum (TMA) as metal organic precursors along with water as an oxidant. The infiltration synthesis process consists of one AlO_x priming cycle followed by six ZnO infiltration cycles. The priming step consists of exposure to TMA for 100 s under a static vacuum (~350 Torr), chamber purging using N_2 (100 sccm) for 100 s, exposure to water vapor (~10 Torr) for 100 s, and chamber purging using N_2 (100 sccm) for 100 s. The following ZnO infiltration cycle consists of exposure to DEZ for 6 min under a static vacuum (~1.7 Torr), chamber purging using N_2 (100 sccm) for 2 min, exposure to water vapor (~10 Torr) for 6 min, and chamber purging using N_2 (100 sccm) for 2 min.

4.2.4. Characterization of DSL Films

As-annealed DSL films in Figure 4-1 were first etched by RIE (Plasma-Therm 790) to enhance the imaging contrast followed by Zeiss Merlin high-resolution SEM characterization at 3 kV from multiple angles. For the SEM images in plan-view, the PDMSB surface layer and microdomains of organic blocks (PS and PLA) were selectively removed by RIE treatment with CF_4 (5 s, 15 mTorr, 50 W) and O_2 (30 s, 6 mTorr, 90 W), respectively. Terraced regions of PDMSB were obtained by covering the half of the sample, etching the other half with CF_4 (60 s, 15 mTorr,

50 W) and O_2 (30 s, 6 mTorr, 90 W), and imaging the boundary between these two regions. This process yields oxidized PDMSB patterns that exhibit the morphology of the PDMSB microdomains. The cross-sections were prepared by cracking the sample in liquid nitrogen followed by RIE with O_2 (5 s, 6 mTorr, 90 W) and imaged after tilting the sample 70° to the SEM detector. The as-infiltrated organic−inorganic hybrids were characterized by TEM (JEOL 2100; 200 kV) and scanning TEM (FEI Talos F200X; 200 kV; equipped with the energy-dispersive spectroscopy or EDS elemental mapping capability). The cross-sectional TEM samples were prepared by the standard *in situ* lift-out procedure using Ga ion milling in a focused ion beam system (FEI Helios 600 Nanolab).

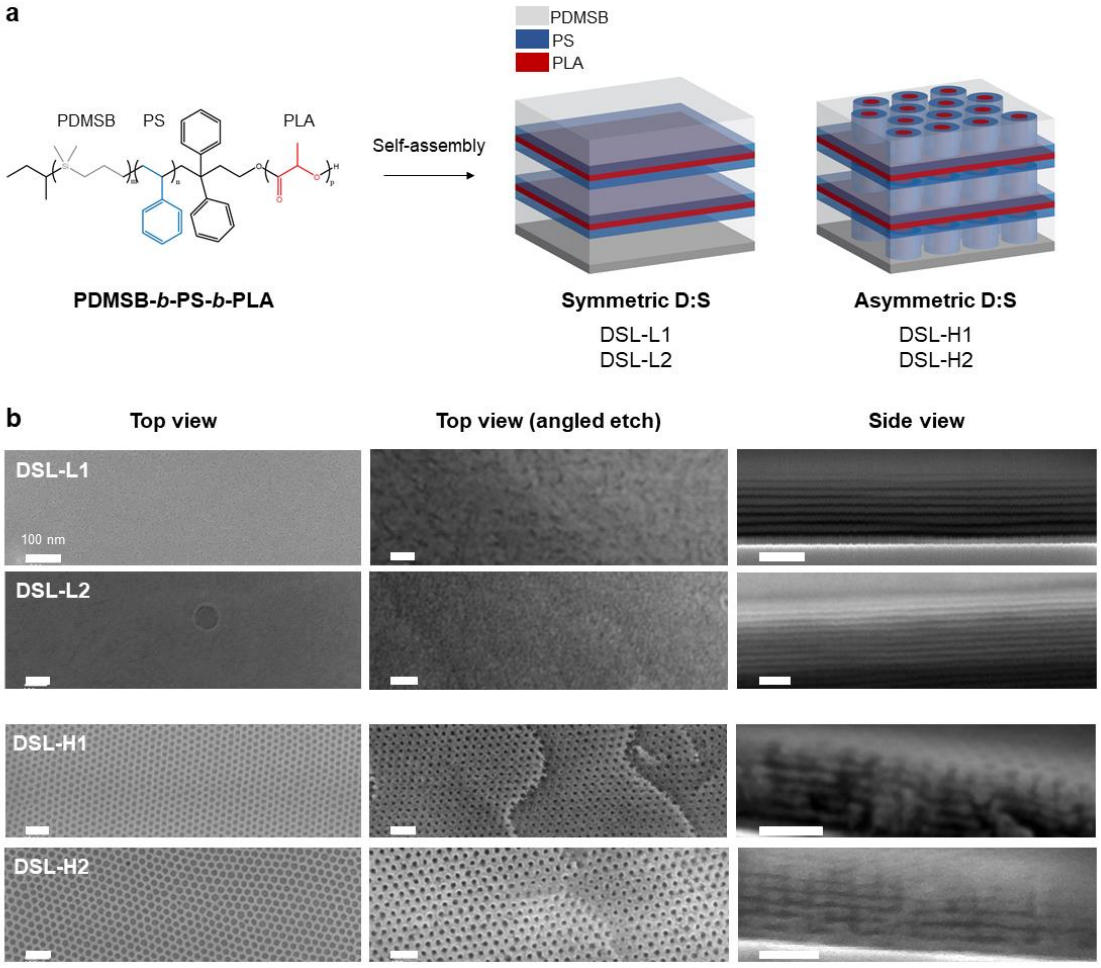

Figure 4-1. (a) Chemical structure of poly(1,1-dimethylsilacyclobutane-*b*-styrene-*b*-lactide) (PDMSB-*b*-PS-*b*-PLA or DSL) and schematic illustrations of self-assembled DSL films. The dominant morphologies obtained in this study for each DSL are presented. DSL-L with symmetric PDMSB and PS compositions form alternating in-plane lamellae (left) and DSL-H with asymmetric PDMSB and PS fractions exhibit in-plane lamellae combined with hexagonally packed vertical core-shell cylinders (right). Schematics in light grey, blue, and red represent PDMSB, PS, and PLA, respectively. (b) SEM images of the final morphologies in DSL films: Top-view (left), plan-view of terraced layers (middle), and side-view (right). The images mainly show contrast from the oxidized PDMSB nanopatterns.

4.3 Results and Discussion

4.3.1 Limited Understanding of DSL Morphologies

DSL (Figure 4-1a) was synthesized using anionic polymerization combined with ring opening polymerization, as described in the Experimental Methods and ref 24. We previously described the syntheses of PDMSB-*b*-PS-*b*-PMMA (DSM)[24,38,46] and PDMSB-*b*-PS-*b*-poly(2-vinylpyridine) (DSV).[26] The PDMSB (not to be confused with PDMS, poly(dimethylsiloxane)) monomeric unit is composed of butane with one Si atom in the backbone. DSL films of 180−260 nm thicknesses were spin-cast onto Si substrates and annealed in a solvent vapor flow of $CHCl_3$. The organic blocks were etched by oxygen plasma RIE and both top and side views of the structure were characterized by SEM. Further analysis was carried out using TEM and scanning transmission electron microscopy (STEM) and elemental mapping using EDS. The bulk morphology of vacuum-annealed samples was characterized using SAXS.

Four DSL compositions were used in this study (Table 1). DSL-L1 and DSL-L2 had symmetric PDMSB and PS volume fractions, while DSL-H1 and DSL-H2 had a volume fraction of PS that was ∼1.5 times that of PDMSB. DSL-H2 is the same polymer composition reported in ref 24. The SAXS data for the bulk DSLs are shown in Figure 4-2. The SAXS contrast originates from the difference in scattering between the PDMSB and the organic blocks. DSL-L1 showed lamellar (Lam) and DSL-L2 showed hexagonally packed cylindrical (Hex) morphologies with period L_0 = 23.2 nm and 31.4 nm, respectively. DSL-H1 exhibited broad peaks, due to its larger molecular weight, and has been tentatively indexed to hexagonally perforated lamellae (HPL) with an AB stacking (L_{100} = 39.2 nm), *i.e.*, HPL with the perforations in one layer located above the

junctions in the adjacent layers, while DSL-H2 showed peaks from a mixture of Hex (L_0 = 19.0 nm) and Lam (L_0 = 36.9 nm) structures.

SEM images of DSL films after oxygen RIE are shown in Figure 4-1b. In both DSL-L1 and L2, the plan-view images show no periodic features but in-plane lamellae ($Lam_{//}$) are observed in the cross-sectional images. This technique does not reveal any contrast between PS and PLA microdomains, showing only the PDMSB lamellae alternating with the non-Si-containing blocks. The Lam structure agrees with the bulk morphology of the DSL-L1, but the DSL-L2 was Hex in bulk, and the Lam thin film structure may be a result of the preferential swelling of PDMSB domains by $CHCl_3$ during the solvent annealing leading to an effective increase in volume fraction. Note that differences between the bulk and thin film morphologies have also been observed for both DSV[26] and DSM[46] samples.

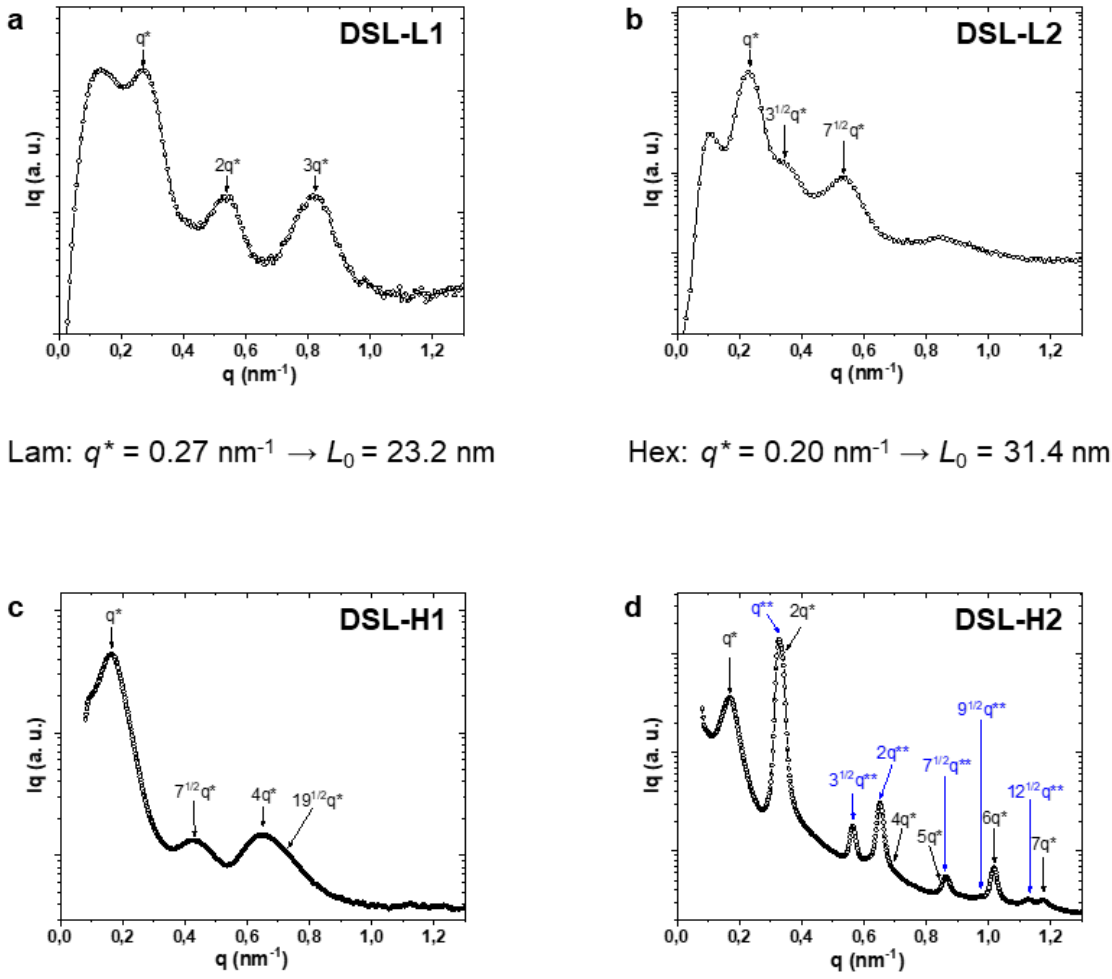

Figure 4-2. Small-angle X-ray scattering (SAXS) plots of intensity *I(q) vs. q* in nm^{-1} for the bulk morphologies of (a) DSL-L1, (b) DSL-L2, (c) DSL-H1, and (d) DSL-H2 after placing the powders under vacuum at 140 °C for 12 h and cooling slowly down to room temperature. The corresponding morphology and period are noted below the plots.

For the DSL-H1 and H2 films, the top-view SEM images (Figure 4-1b and Figure 4-3) clearly exhibit a hexagonal pore array attributed to the out-of-plane cylindrical morphology, $Hex_{\perp}$. The pores show a core-shell morphology assumed to consist of a PS shell and a PLA core, evident from a difference in their etching rate in the O_2 plasma. To examine the structure at different depths, we introduced an angled plasma RIE followed by SEM imaging from the top surface (see Experimental Methods). This reveals terraces showing vertical alignment of the core-shell cylinders throughout the film, in agreement with the DSL-H2 results in ref 24. Cross-sectional imaging of both DSL-H1 and H2 shows in-plane $Lam_{//}$ with vertical features corresponding to the cylinders passing through the perforations in the lamellae. We therefore describe the structure as $Lam_{//}$-$Hex_{\perp}$. Our earlier work[24] on DSL-H2 also showed that about 20 % of the film had a morphology attributed to alternating in-plane cylindrical microdomains ($Alt_{//}$); a similar result was found in the present work for DSL-H2 but no in-plane cylinders were found in DSL-H1.

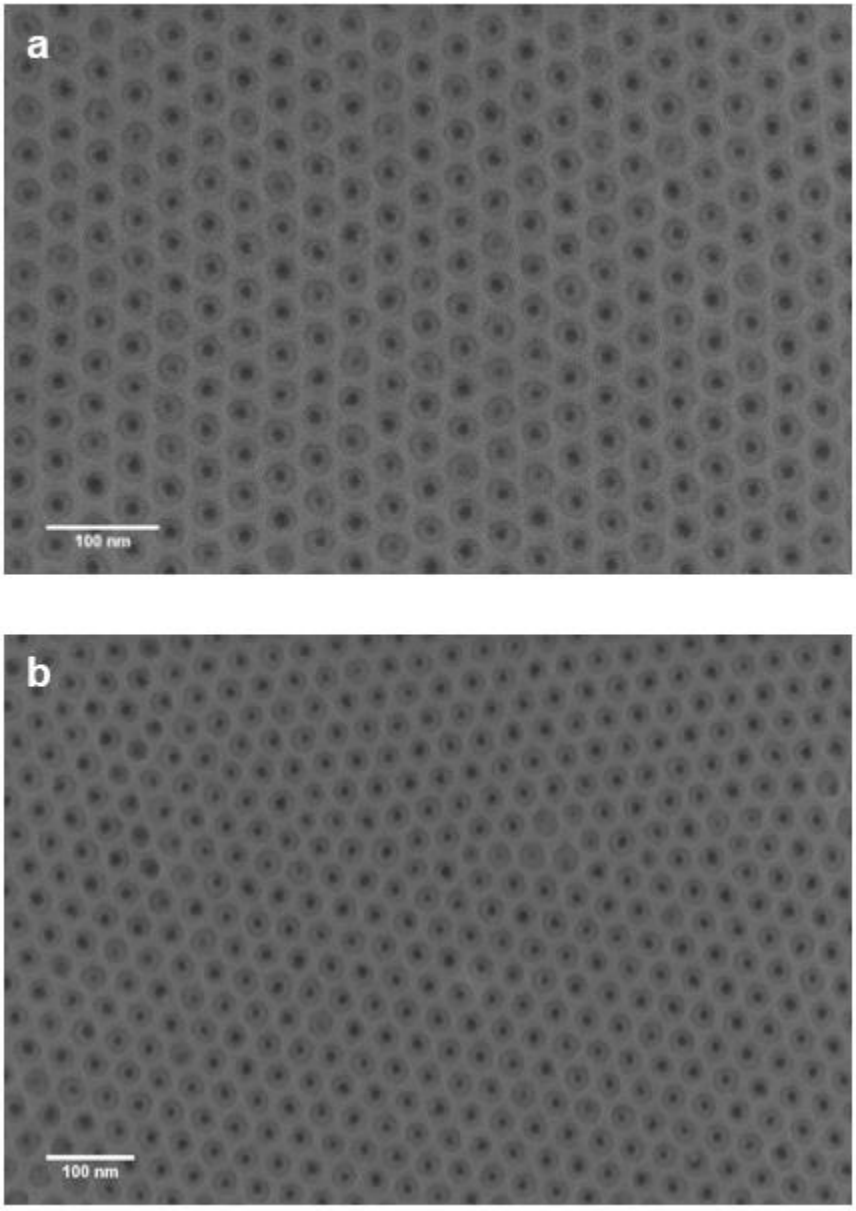

Figure 4-3. Top-view SEM images of self-assembled morphologies in DSL-H films after annealing in a solvent vapor flow of $CHCl_3$:N_2 = 10:1: (a) DSL-H1 and (b) DSL-H2 showing the vertical core-shell cylinders of PLA-PS after O_2 reactive ion etching (RIE).

4.3.2 Selective VPI of ZnO Resolving Three-Color Lamellae of DSL Films

To clarify the distribution of PS and PLA within the microphase-separated DSL films, we employed infiltration synthesis to infuse ZnO selectively within the PLA microdomains. ZnO infiltration consisted of cyclic exposures of the BCP film to DEZ and water, which are precursors respectively for Zn and O. In total, six cycles were performed, assisted by an initial single AlO_x infiltration cycle using TMA and water (referred to as AlO_x priming).[31,47−48] During an infiltration synthesis cycle, gaseous organometallic precursors, which are typically Lewis acids, diffuse into the polymer matrix and react with Lewis-basic functional groups within the polymer to form chemical bonds. A subsequent exposure of the film to an oxidizing agent, such as water, transforms the preinfiltrated organometallic precursor into metal oxide molecules. In the DSL films, only the PLA block contains a Lewis-basic carbonyl group, and thus, metal oxide moieties are expected to be selectively infiltrated into the PLA domain. However, similar to the well-studied PMMA, the carbonyl group within PLA does not readily react with weakly Lewis-acidic DEZ.[31,35,47−48] This was mitigated by the AlO_x priming because more Lewis-acidic TMA can react better with the carbonyl group and generate −Al−OH species in the PLA domain once the priming cycle is completed with water. The available OH group then can readily react with DEZ, facilitating the subsequent infiltration cycles of ZnO.

Figure 4-4a shows schematics of the proposed structure of the DSL-L thin films after infiltration, with ZnO present in the PLA blocks. Figure 4-4b shows a cross-sectional bright-field TEM image of DSL-L1 after ZnO infiltration. The dark and uniform in-plane lamellae consist of the Si-containing PDMSB block. However, additional layers are evident within the in-plane

lamellae, which are identified as ZnO-infused PLA, confirming the alternating three-color lamellar structure of DSL-L1. DSL-L2 shows a similar morphology, as shown in Figure 4-5 and 4-6. The ZnO-infiltrated PLA lamellae exhibit rough interfaces and a sparse distribution of ZnO particles, which are attributed to the small volume fraction of PLA (f_{PLA} = 0.19) in DSL-L1. The discontinuous ZnO growth inside the PLA domain could also result from the single AlO_x priming cycle that is insufficient to provide uniform reactivity with the infiltrating DEZ; we did not pursue AlO_x-only infiltration due to the lack of Z-contrast between Al and Si, but this was demonstrated previously for DSM where the PMMA cores of core-shell cylinders were decorated with alumina.[38] DSL-L2, which includes a larger fraction of PLA (f_{PLA} = 0.28) exhibits more homogeneous ZnO layers in between PS lamellae (Figures 4-5 and 4-6).

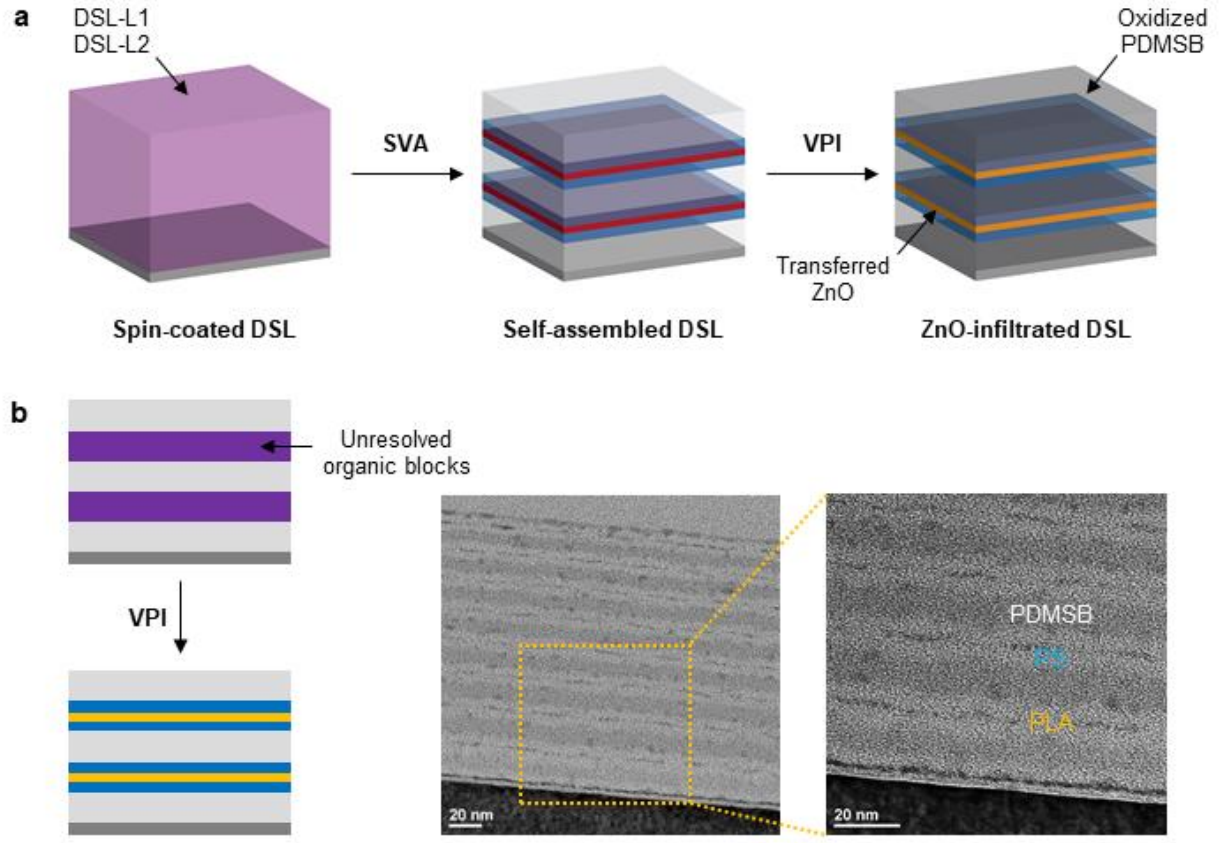

Figure 4-4. (a) Schematic illustrations depicting the solvent vapor annealing (SVA) followed by infiltration synthesis to produce SiO_x/PS/ZnO nanostructures in DSL-L films. The purple structure in the spin-coated DSL film represents as-cast DSL-L before microphase separation. Schematics in light grey, blue, red, grey, and yellow represent PDMSB, PS, PLA, SiO_x, and ZnO, respectively. (b) Schematic illustrations (left) of the cross-sections of DSL-L structure before (top) and after (bottom) infiltration of ZnO and TEM images (right) of resultant SiO_x/PS/ZnO nanostructure in DSL-L1 film.

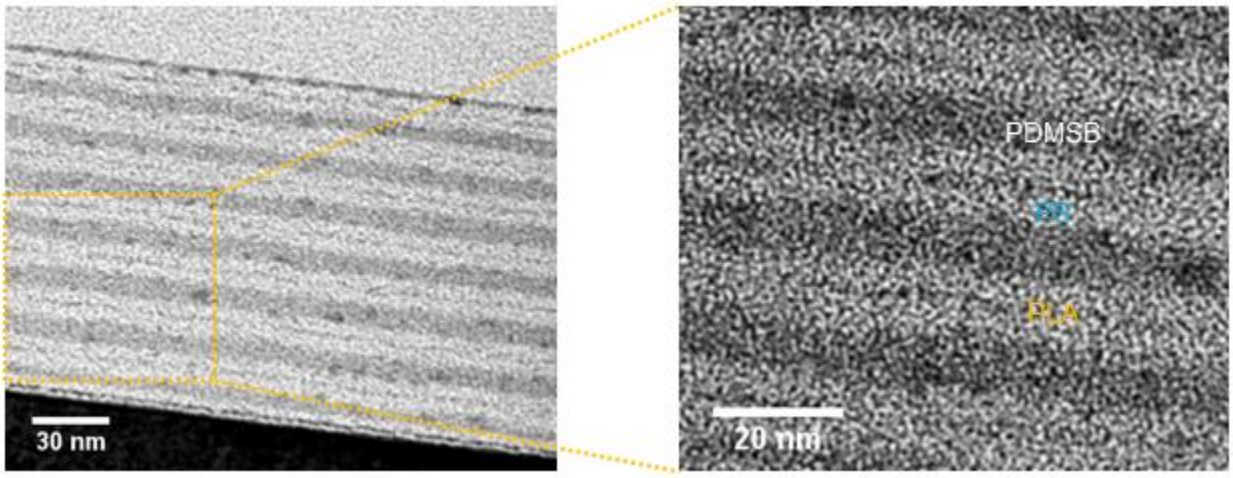

Figure 4-5. TEM images of the cross-sections of DSL-L2 structure after infiltration of ZnO, showing the resultant SiO_x/PS/ZnO three-color lamellae.

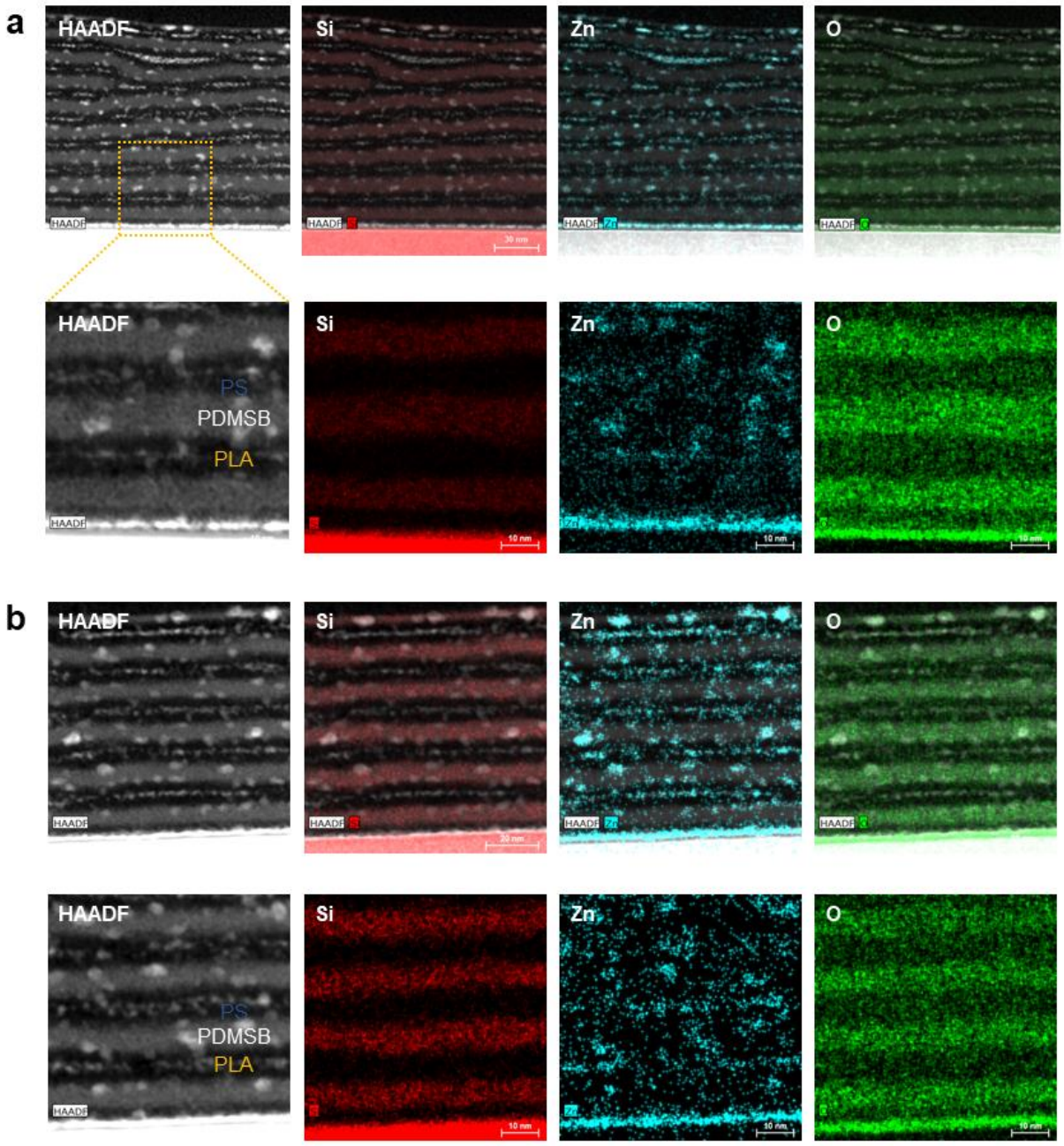

Figure 4-6. High-angle annular dark-field (HAADF) scanning transmission electron microscopy (STEM) images and associated energy-dispersive spectroscopy (EDS) area elemental mappings (Si, Zn, and O) for the cross-sections of ZnO infiltrated (a) DSL-L1 and (b) DSL-L2 structures.

The ZnO-infiltrated DSL-L1 structure was analyzed by high-angle annular dark-field (HAADF) imaging and EDS elemental mapping (Figure 4-6a). HAADF images sensitive to Z-contrast reveal the three-color lamellar structure with ZnO present in the PLA throughout the film thickness. This demonstrates the potential of this approach to resolve the internal structure of even thick films. Elemental mapping shows that as expected, Si is uniformly distributed in the PDMSB domain, which exhibit sharp interfaces, but oxygen is also present. In fact, the oxidation appears to have occurred before the ZnO infiltration (Figure 4-7), likely due to ambient oxygen and water. The majority of Zn is selectively infiltrated into PLA but there are also ZnO particles present in the PDMSB, presumably due to its prior oxidation, which could provide an increased reactivity of the PDMSB toward DEZ. Kinetic entrapment of precursors driven by weak physisorption within the polymer matrix might also contribute, as has been proposed to explain AlO_x and ZnO infiltration into PDMS.[49–51] It is noted that the nominally unreactive blocks around the PLA are not expected to retard the infiltration of ZnO into the targeted PLA domain because the absence of strong interaction between infiltrating precursors and unreactive polymer domains renders their diffusion through the inert domains fast, as confirmed by a recent study by Waldman *et al.* examining the infiltration of weakly interacting organometallic precursors in homopolymer thin films.[52] This is consistent with previous reports that have shown a high-fidelity block-selective infiltration of various inorganic materials into isolated PMMA domains surrounded by a majority of unreactive PS domains.[31–32]

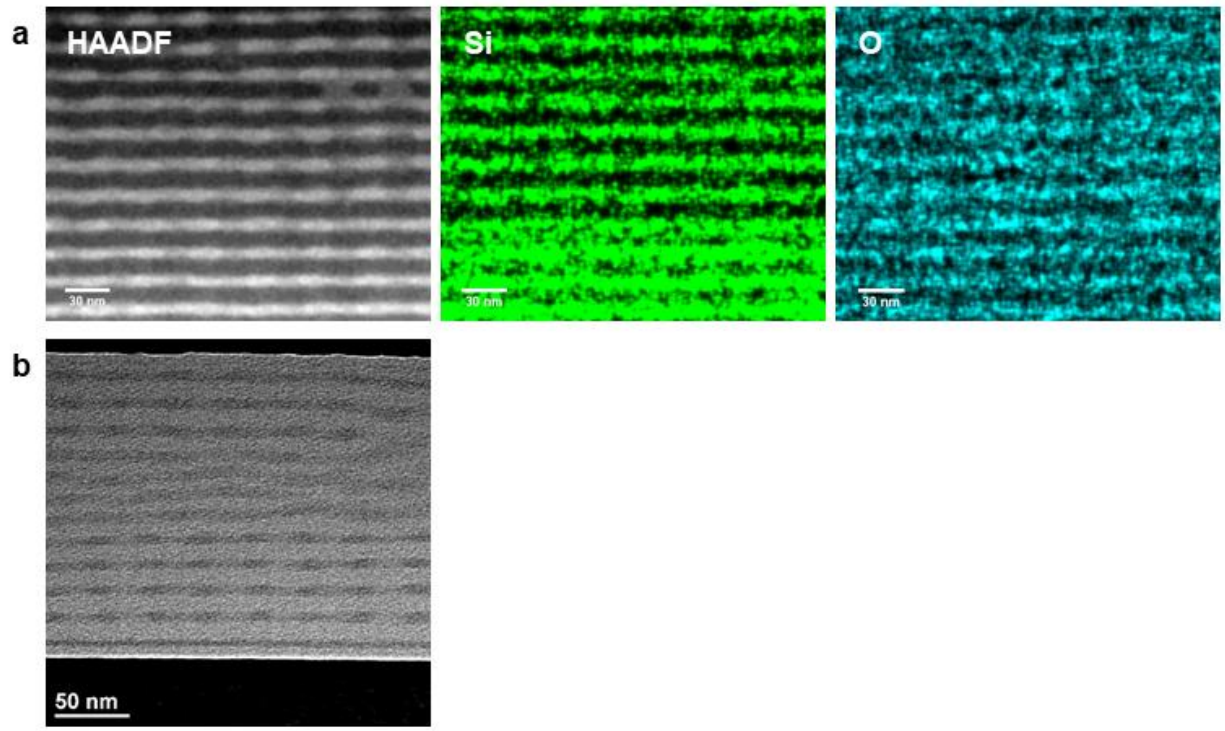

Figure 4-7. (a) HAADF STEM image and associated EDS area elemental mappings (Si and O) for a cross-section of non-infiltrated DSL-H1. (b) Bright field image of non-infiltrated DSL-H2. The darker layers are the PDMSB, and the lighter layers include both PS and PLA. The PDMSB shows periodic in-plane changes in contrast corresponding to the vertical cylinders.

Based on the elemental maps for the ZnO-infiltrated DSL-L films, we estimated the periodicities and volume fraction of microdomains in each structure, as shown in Figure 4-8. The period of DSL-L1 ($L_{0,L1}$ = 21 nm) is larger than that of DSL-L2 ($L_{0,L2}$ = 16 nm), $L_{0,L1}/L_{0,L2}$ = 1.31, although the difference exceeds that predicted from the ratio of (molecular weight (M_n))$^{2/3}$, $(M_{n,L1}/M_{n,L2})^{2/3}$ = 1.07. For both structures, the PDMSB domains are 1.5 times wider than the organic domains although the volume fraction of PDMSB is 36−41 %. This is attributed to

preferential swelling of the PDMSB during solvent annealing, which is at least partly preserved after drying.

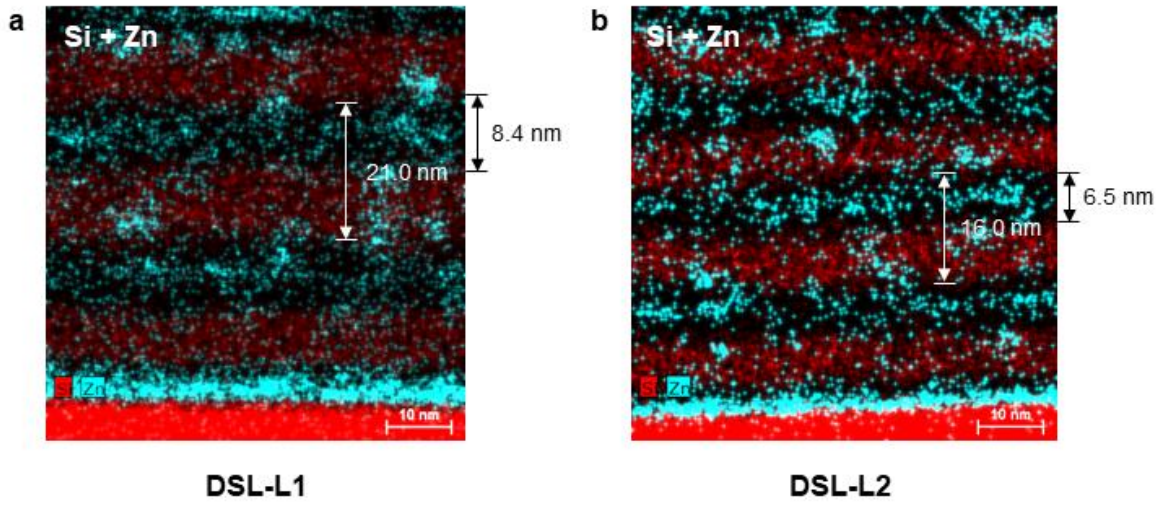

Figure 4-8. EDS elemental mappings of both Si (red) and Zn (blue) for DSL structures: (a) DSL-L1 and (b) DSL-L2. Estimated width of each microdomain is indicated.

4.3.3 Selective VPI of ZnO Resolving Core-Shell Cylinders of DSL Films

ZnO was infiltrated into DSL-H films *via* the same process, as described in Figure 4-9a. Unlike DSL-L, the DSL-H forms $Lam_{//}$ through which $Hex_{\perp}$ of PLA-PS pass perpendicular to the substrate, *i.e.*, the SEM indicates a morphology consisting of both in-plane and out-of-plane periodic features, a result supported by GISAXS[24] and also described for thick films of DSV.[26] Figure 4-9b shows cross-sectional HAADF STEM data comparing the DSL-H1 morphology

before and after ZnO infiltration. This clearly shows selective ZnO infiltration into the PLA block at the junction between the lamellae and cylinders, while the uninfiltrated sample exhibits no such contrast. As illustrated in the schematics in Figure 4-9b, the wider region of ZnO visible at the cylinder−lamella intersection is attributed to the widening of the PLA block at the junction between the cores of the cylinders and the thin PLA lamellae. Little ZnO is seen outside the junction areas due to the narrowness of the PLA cores and lamellae. However, it is clear that the ZnO-decorated regions are located at the center of the vertical core-shell cylindrical domains, and the SEM depth profile and cross section of the etched films (Figure 4-1b and Figure 4-3) confirm the continuity of the vertical PLA cores.

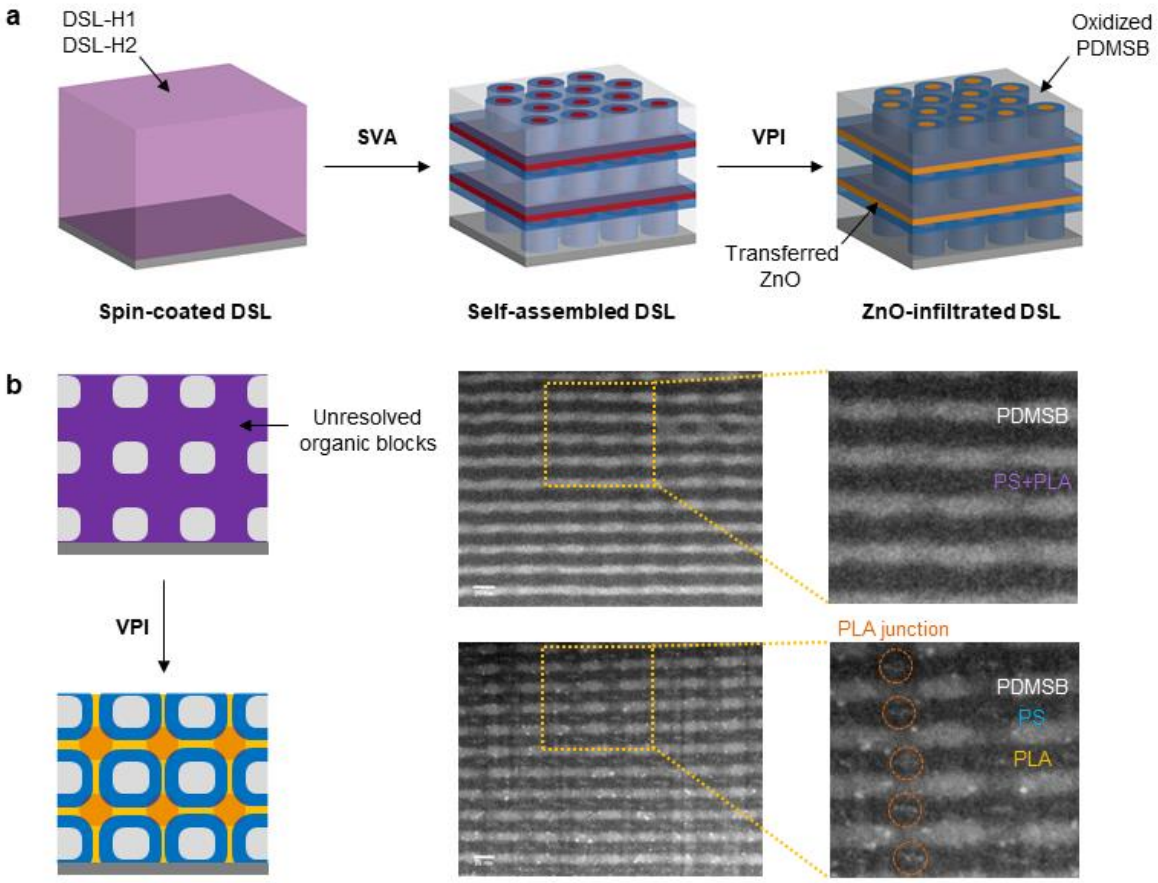

Figure 4-9. (a) Schematic illustrations depicting SVA followed by infiltration synthesis to produce SiO_x/PS/ZnO nanostructures in DSL-H films. The purple structure in the spin-coated DSL film represents as-cast DSL-H before phase separation. Schematics in light grey, blue, red, grey, and yellow represent PDMSB, PS, PLA, SiO_x, and ZnO, respectively. (b) Schematic illustrations (left) and HAADF STEM images (right) of the cross-sections of DSL-H1 structure before (top) and after (bottom) infiltration of ZnO. The junctions between the lateral and vertical PLA domains are highlighted by orange circles in the schematic and in the magnified STEM image of ZnO infiltrated DSL-H1 structure.

The phase behavior of ZnO-infiltrated DSL-H2, which includes a much lower fraction of PLA than DSL-H1, is shown in Figure 4-10. Thin ZnO-decorated layers are present within the PS lamellae corresponding to the PLA lamellae embedded in the PS, as seen in DSL-L1, L2, and H1. This is in agreement with the morphology of DSL-H2 resolved by employing hydrolysis to selectively degrade the PLA domains.[24] However, unlike DSL-H1, thicker ZnO-infused regions corresponding to the cores of the core-shell cylinders are not evident in the image, even though the SEM plan-view and cross-section (Figure 4-1b) as well as the bright-field cross-section of the uninfiltrated DSL-H2 (Figure 4-7b) demonstrate continuous vertical cylinders. We assume that the low volume fraction of the PLA limited the infiltration of Zn into the cylinder cores, which were not resolved in Figure 4-10. We note that self-assembled BCP films in general can be swelled when exposed to infiltrating precursors as organic vapors can do,[53] but our TEM data clearly indicate no disruption of the self-assembled BCP morphology by the precursor infiltration. This is most likely due to the purging step included in the infiltration protocol, which removes the unreacted precursor out of the BCP film.

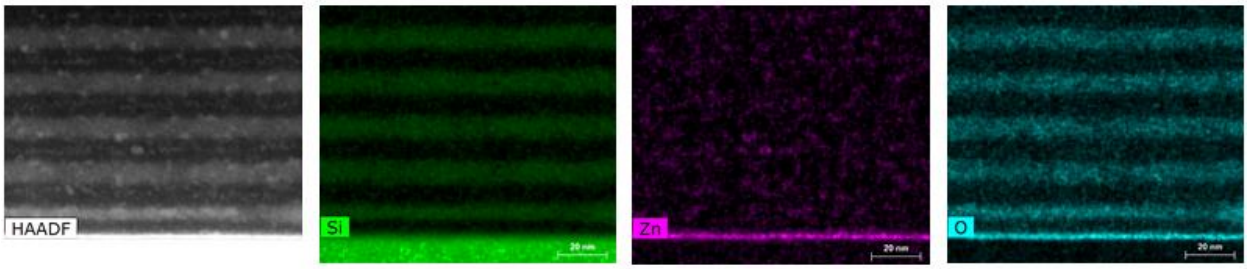

Figure 4-10. HAADF STEM images and associated EDS area elemental mappings (Si, Zn, and O) for the cross-sections of ZnO-infiltrated DSL-H2 structure.

Unlike the HPL phase in DSV thick films where the perforations are stacked in an AB sequence,[26] the DSL-H in this work shows an AA stacking sequence according to the SEM and STEM images in Figures 4-1 and 4-9, respectively. The AA sequence refers to the perforations aligned above each other in adjacent lamellae, *i.e.*, cylinders penetrating orthogonal to the lamellae. This is the same structure as we proposed in ref 24 and it is also the structure observed in thick films of DSM blended with PDMSB-*b*-PS, which results in $f_{PDMSB}/f_{PS}/f_{PMMA}$ = 0.31/0.45/0.24.[46] Thus, the two DSL-H here and the DSM blend in ref 46 have similar volume fractions and are found to exhibit AA stacked $Lam_{//}$–$Hex_{\perp}$ under solvent annealing in $CHCl_3$, a morphology that has not been reported in other BCPs.

We note that the demonstrated use of block-selective infiltration in TBTPs achieves TEM contrast enhancement in a similar manner to traditional polymer staining methods based on OsO_4 and RuO_4 reagents, with the former known to oxidize polymers with olefinic functionalities and the latter to react primarily with aromatic and unsaturated polymers.[54–56] Another example is iodide staining, which is used to investigate the internal 3D structure of ~25 nm-thick films of an ABA triblock copolymer, poly(2-vinylpyridine)-*b*-PS-*b*-poly(2-vinylpyridine).[57] However, these methods can be very slow (*e.g.*, even up to several days)[55] or difficult to perform due to the toxicity of the metal oxides, and it may be hard to predict the domains to be stained due to various other chemical and structural characteristics known to affect the preferential reactivity of blocks.[56] On the other hand, infiltration synthesis, relying on a relatively straightforward Lewis acid–base interaction between infiltrating precursors and polymers, allows us to predict the domain to be preferentially infiltrated and is quick and safe to implement using a commercial ALD system.

4.4 Conclusions

In summary, a VPI synthesis was demonstrated to selectively deposit inorganic material (ZnO) into an organic block (PLA) of a triblock terpolymer film. The infiltration extends over film thicknesses of at least 260 nm and enables the resolution of microdomain morphologies and volume fractions of the blocks. The triblock terpolymer, DSL, shows a transition from a three-color lamellar structure to perforated lamellae plus perpendicular core-shell cylinders on decreasing the volume fraction of the PDMSB. Environmental oxidation of the PDMSB domains formed SiO_x, and infiltration of the PLA domains with ZnO results in hierarchical ZnO/polymer/SiO_x nanostructures. Infiltration synthesis therefore provides access to multicomponent nanocomposites with both lateral and vertical periodicities as well as a process for investigating complex 3D BCP morphologies.

References

[1] Lee, S.; Subramanian, A.; Tiwale, N.; Kisslinger, K.; Mumtaz, M.; Shi, L.-Y.; Aissou, K.; Nam, C.-Y.; Ross, C. A. Resolving Triblock Terpolymer Morphologies by Vapor-Phase Infiltration. *Chem. Mater.* **2020**, *32*, 5309−5316.

[2] Shulaker, M. M.; Hills, G.; Park, R. S.; Howe, R. T.; Saraswat, K.; Wong, H.-S. P.; Mitra, S. Three-Dimensional Integration of Nanotechnologies for Computing and Data Storage on a Single Chip. *Nature* **2017**, *547*, 74−78.

[3] Javey, A.; Nam, S. W.; Friedman, R. S.; Yan, H.; Lieber, C. M. Layer-by-Layer Assembly of Nanowires for Three-Dimensional, Multifunctional Electronics. *Nano Lett.* **2007**, *7*, 773−777.

[4] Li, H.; Li, X.; Guo, D.; Lou, L.; Li, W.; Zhang, X. Three-Dimensional Self-Assembly of Core/Shell-Like Nanostructures for High-Performance Nanocomposite Permanent Magnets. *Nano Lett.* **2016**, *16*, 5631−5638.

[5] Fernández-Pacheco, A.; Streubel, R.; Fruchart, O.; Hertel, R.; Fischer, P.; Cowburn, R. P. Three-Dimensional Nanomagnetism. *Nat. Commun.* **2017**, *8*, 15756.

[6] von Freymann, G.; Ledermann, A.; Thiel, M.; Staude, I.; Essig, S.; Busch, K.; Wegener, M. Three-Dimensional Nanostructures for Photonics. *Adv. Funct. Mater.* **2010**, *20*, 1038−1052.

[7] Castles, F.; Day, F. V.; Morris, S. M.; Ko, D-H.; Gardiner, D. J.; Qasim, M. M.; Nosheen, S.; Hands, P. J. W.; Choi, S. S.; Friend, R. H.; Coles, H. J. Blue-Phase Templated Fabrication of Three-Dimensional Nanostructures for Photonic Applications. *Nat. Mater.* **2012**, *11*, 599−603.

[8] Ross, C. A.; Berggren, K. K.; Cheng, J. Y.; Jung, Y. S.; Chang, J.-B. Three-Dimensional Nanofabrication by Block Copolymer Self-Assembly. *Adv. Mater.* **2014**, *26*, 4386−4396.

[9] Tavakkoli K. G., A.; Gotrik, K. W.; Hannon, A. F.; Alexander-Katz, A.; Ross, C. A.; Berggren, K. K. Templating Three-Dimensional Self-Assembled Structures in Bilayer Block Copolymer Films. *Science* **2012**, *336*, 1294−1298.

[10] Oh, J.; Suh, H. S.; Ko, Y.; Nah, Y.; Lee, J.-C.; Yeom, B.; Char, K.; Ross, C. A.; Son, J. G. Universal Perpendicular Orientation of Block Copolymer Microdomains Using a Filtered Plasma. *Nat. Commun.* **2019**, *10*, 2912.

[11] Rahman, A.; Majewski, P. W.; Doerk, G.; Black, C. T.; Yager, K. G. Non-Native Three-Dimensional Block Copolymer Morphologies. *Nat. Commun.* **2016**, *7*, 13988.

[12] Cheng, L.-C.; Simonaitis, J. W.; Gadelrab, K. R.; Tahir, M.; Ding, Y.; Alexander-Katz, A.; Ross, C. A. Imparting Superhydrophobicity with a Hierarchical Block Copolymer Coating. *Small* **2020**, *16*, 1905509.

[13] Chuang, V. P.; Cheng, J. Y.; Savas, T. A.; Ross, C. A. Three-Dimensional Self-Assembly of Spherical Block Copolymer Domains into V-Shaped Grooves. *Nano Lett.* **2006**, *6*, 2332−2337.

[14] Lee, S.; Cheng, L.-C.; Gadelrab, K. R.; Ntetsikas, K.; Moschovas, D.; Yager, K. G.; Avgeropoulos, A.; Alexander-Katz, A.; Ross, C. A. Double-Layer Morphologies from a Silicon-Containing ABA Triblock Copolymer. *ACS Nano* **2018**, *12*, 6193−6202.

[15] Ren, Y.; Zou, Y.; Liu, Y.; Zhou, X.; Ma, J.; Zhao, D.; Wei, G.; Ai, Y.; Xi, S.; Deng, Y. Synthesis of Orthogonally Assembled 3D Cross-Stacked Metal Oxide Semiconducting Nanowires. *Nat. Mater.* **2020**, *19*, 203−211.

[16] Choi, H. K.; Aimon, N. M.; Kim, D. H.; Sun, X. Y.; Gwyther, J.; Manners, I.; Ross, C. A. Hierarchical Templating of a $BiFeO_3$−$CoFe_2O_4$ Multiferroic Nanocomposite by a Triblock Terpolymer Film. *ACS Nano* **2014**, *8*, 9248−9254.

[17] Chuang, V. P.; Gwyther, J.; Mickiewicz, R. A.; Manners, I.; Ross, C. A. Templated Self-Assembly of Square Symmetry Arrays from an ABC Triblock Terpolymer. *Nano Lett.* **2009**, *9*, 4364−4369.

[18] Son, J. G.; Gwyther, J.; Chang, J.-B.; Berggren, K. K.; Manners, I.; Ross, C. A. Highly Ordered Square Arrays from a Templated ABC Triblock Terpolymer. *Nano Lett.* **2011**, *11*, 2849−2855.

[19] Robbins, S. W.; Beaucage, P. A.; Sai1, H.; Tan, K. W.; Werner, J. G.; Sethna, J. P.; DiSalvo, F. J.; Gruner, S. M.; Van Dover, R. B.; Wiesner, U. Block Copolymer Self-Assembly–Directed Synthesis of Mesoporous Gyroidal Superconductors. *Sci. Adv.* **2016**, *2*, e1501119.

[20] Docampo, P.; Stefik, M.; Guldin, S.; Gunning, R.; Yufa, N. A.; Cai, N.; Wang, P.; Steiner, U.; Wiesner, U.; Snaith, H. J. Triblock-Terpolymer-Directed Self-Assembly of Mesoporous TiO_2: High-Performance Photoanodes for Solid-State Dye-Sensitized Solar Cells. *Adv. Energy Mater.* **2012**, *2*, 676−682.

[21] Vignolini, S.; Yufa, N. A.; Cunha, P. S.; Guldin, S.; Rushkin, I.; Stefik, M.; Hur, K.; Wiesner, U.; Baumberg, J. J.; Steiner, U. A 3D Optical Metamaterial Made by Self-Assembly. *Adv. Mater.* **2012**, *24*, OP23−OP27.

[22] Löbling, T. I.; Borisov, O.; Haataja, J. S.; Ikkala, O.; Gröschel, A. H.; Müller, A. H. E. Rational Design of ABC Triblock Terpolymer Solution Nanostructures with Controlled Patch Morphology. *Nat. Commun.* **2016**, *7*, 12097.

[23] Löbling, T. I.; Hiekkataipale, P.; Hanisch, A.; Bennet, F.; Schmalz, H.; Ikkala, O.; Groschel, A. H.; Müller, A. H.E. Bulk Morphologies of Polystyrene-block-Polybutadiene-block-Poly(tert-butyl methacrylate) Triblock Terpolymers. *Polymer* **2015**, *72*, 479−489.

[24] Lee, S.; Cheng, L.-C.; Yager, K. G.; Mumtaz, M.; Aissou, K.; Ross, C. A. *In Situ* Study of ABC Triblock Terpolymer Self-Assembly under Solvent Vapor Annealing. *Macromolecules* **2019**, *52*, 1853−1863.

[25] Nunns, A.; Ross, C. A.; Manners, I. Synthesis and Bulk Self-Assembly of ABC Star Terpolymers with a Polyferrocenylsilane Metalloblock. *Macromolecules* **2013**, *46*, 2628−2635.

[26] Aissou, K.; Mumtaz, M.; Bouzit, H.; Pecastaings, G.; Portale, G.; Fleury, G.; Hadziioannou, G. Bicontinuous Network Nanostructure with Tunable Thickness Formed on Asymmetric Triblock Terpolymer Thick Films. *Macromolecules* **2019**, *52*, 4413−4420.

[27] Gu, X.; Gunkel, I.; Russell, T. P. Pattern Transfer Using Block Copolymers. *Phil. Trans. R. Soc. A* **2013**, *371*, 20120306.

[28] Lee, S.-M.; Pippel, E.; Gösele, U.; Dresbach, C.; Qin, Y.; Chandran, C. V.; Bräuniger, T.; Hause, G.; Knez, M. Greatly Increased Toughness of Infiltrated Spider Silk. *Science* **2009**, *324*, 488−492.

[29] Gong, B.; Peng, Q.; Jur, J. S.; Devine, C. K.; Lee, K.; Parsons, G. N. Sequential Vapor Infiltration of Metal Oxides into Sacrificial Polyester Fibers: Shape Replication and Controlled Porosity of Microporous/Mesoporous Oxide Monoliths. *Chem. Mater.* **2011**, *23*, 3476−3485.

[30] Peng, Q.; Tseng, Y.-C.; Darling, S. B.; Elam, J. W. Nanoscopic Patterned Materials with Tunable Dimensions *via* Atomic Layer Deposition on Block Copolymers. *Adv. Mater.* **2010**, *22*, 5129−5133.

[31] Peng, Q.; Tseng, Y.-C.; Darling, S. B.; Elam, J. W. A Route to Nanoscopic Materials *via* Sequential Infiltration Synthesis on Block Copolymer Templates. *ACS Nano* **2011**, *5*, 4600−4606.

[32] Segal-Peretz, T.; Winterstein, J.; Doxastakis, M.; Ramirez-Hernandez, A.; Biswas, M.; Ren, J.; Suh, H. S.; Darling, S. B.; Liddle, J. A.; Elam, J. W.; de Pablo, J. J.; Zaluzec, N. J.; Nealey, P. F. Characterizing the Three-Dimensional Structure of Block Copolymers *via* Sequential Infiltration Synthesis and Scanning Transmission Electron Tomography. *ACS Nano* **2015**, *9*, 5333−5347.

[33] Cummins, C.; Ghoshal, T.; Holmes, J. D.; Morris, M. A. Strategies for Inorganic Incorporation using Neat Block Copolymer Thin Films for Etch Mask Function and Nanotechnological Application. *Adv. Mater.* **2016**, *28*, 5586−5618.

[34] Chai, J.; Buriak, J. M. Using Cylindrical Domains of Block Copolymers To Self-Assemble and Align Metallic Nanowires. *ACS Nano* **2008**, *2*, 489−501.

[35] Subramanian, A.; Doerk, G.; Kisslinger, K.; Yi, D. H.; Grubbs, R. B.; Nam, C.-Y. Three-Dimensional Electroactive ZnO Nanomesh Directly Derived from Hierarchically Self-Assembled Block Copolymer Thin Films. *Nanoscale* **2019**, *11*, 9533−9546.

[36] Subramanian, A.; Tiwale, N.; Nam, C.-Y. Review of Recent Advances in Applications of Vapor-Phase Material Infiltration Based on Atomic Layer Deposition. *JOM* **2019**, *71*, 185−196.

[37] Subramanian, A.; Tiwale, N.; Doerk, G.; Kisslinger, K.; Nam, C.-Y. Enhanced Hybridization and Nanopatterning *via* Heated Liquid-Phase Infiltration into Self-Assembled Block Copolymer Thin Films. *ACS Appl. Mater. Interfaces* **2020**, *12*, 1444−1453.

[38] Aissou, K.; Mumtaz, M.; Marcasuzaa, P.; Brochon, C.; Cloutet, E.; Fleury, G.; Hadziioannou, G. Highly Ordered Nanoring Arrays Formed by Templated Si-Containing Triblock Terpolymer Thin Films, *Small* **2017**, *13*, 1603184.

[39] Waldman, R. Z.; Mandia, D. J.; Yanguas-Gil, A.; Martinson, A. B. F.; Elam, J. W.; Darling, S. B. The Chemical Physics of Sequential Infiltration Synthesis-A Thermodynamic and Kinetic Perspective. *J. Chem. Phys.* **2019**, *151*, 190901.

[40] Peng, Q.; Tseng, Y.-C.; Long, Y.; Mane, A. U.; DiDona, S.; Darling, S. B.; Elam, J. W. Effect of Nanostructured Domains in Self-Assembled Block Copolymer Films on Sequential Infiltration Synthesis. *Langmuir* **2017**, *33*, 13214−13223.

[41] Kim, E.; Vaynzof, Y.; Sepe, A.; Guldin, S.; Scherer, M.; Cunha, P.; Roth, S. V.; Steiner, U. Gyroid-Structured 3D ZnO Networks Made by Atomic Layer Deposition. *Adv. Funct. Mater.* **2014**, *24*, 863−872.

[42] Rahman, A.; Ashraf, A.; Xin, H.; Tong, X.; Sutter, P.; Eisaman, M. D.; Black, C. T. Sub-50-nm Self-Assembled Nanotextures for Enhanced Broadband Antireflection in Silicon Solar Cells. *Nat. Commun.* **2015**, *6*, 5963.

[43] Akyildiz, H. I.; Stano, K. L.; Roberts, A. T.; Everitt, H. O.; Jur, J. S. Photoluminescence Mechanism and Photocatalytic Activity of Organic−Inorganic Hybrid Materials Formed by Sequential Vapor Infiltration. *Langmuir* **2016**, *32*, 4289−4296.

[44] Simón, L.; Goodman, J. M. The Mechanism of TBD-Catalyzed Ring-Opening Polymerization of Cyclic Esters. *J. Org. Chem.* **2007**, *72*, 9656−9662.

[45] Gotrik, K. W.; Hannon, A. F.; Son, J. G.; Keller, B.; Alexander-Katz, A.; Ross, C. A. Morphology Control in Block Copolymer Films Using Mixed Solvent Vapors. *ACS Nano* **2012**, *6*, 8052−8059.

[46] Aissou, K.; Mumtaz, M.; Demazy, N.; Pécastaings, G.; Fleury, G.; Hadziioannou, G. Periodic Bicontinuous Structures Formed on the Top Surface of Asymmetric Triblock Terpolymer Thick Films. *ACS Macro Lett.* **2019**, *8*, 923−930.

[47] Kamcev, J.; Germack, D. S.; Nykypanchuk, D.; Grubbs, R. B.; Nam, C.-Y.; Black, C. T. Chemically Enhancing Block Copolymers for Block-Selective Synthesis of Self-Assembled Metal Oxide Nanostructures. *ACS Nano* **2013**, *7*, 339−346.

[48] Ocola, L. E.; Connolly, A.; Gosztola, D. J.; Schaller, R. D.; Yanguas-Gil, A. Infiltrated Zinc Oxide in Poly(methyl methacrylate): An Atomic Cycle Growth Study. *J. Phys. Chem. C* **2017**, *121*, 1893−1903.

[49] Yu, Y.; Li, Z.; Wang, Y.; Gong, S.; Wang, X. Sequential Infiltration Synthesis of Doped Polymer Films with Tunable Electrical Properties for Efficient Triboelectric Nanogenerator Development. *Adv. Mater.* **2015**, *27*, 4938−4944.

[50] Gong, B.; Spagnola, J. C.; Parsons, G. N. Hydrophilic Mechanical Buffer Layers and Stable Hydrophilic Finishes on Polydimethylsiloxane Using Combined Sequential Vapor Infiltration and Atomic/Molecular Layer Deposition. *J. Vac. Sci. Technol. A* **2012**, *30*, 01A156.

[51] Leng, C. Z.; Losego, M. D. Vapor Phase Infiltration (VPI) for Transforming Polymers into Organic–Inorganic Hybrid Materials: A Critical Review of Current Progress and Future Challenges. *Mater. Horiz.* **2017**, *4*, 747−771.

[52] Waldman, R. Z.; Jeon, N.; Mandia, D. J.; Heinonen, O.; Darling, S. B.; Martinson, A. B. F. Sequential Infiltration Synthesis of Electronic Materials: Group 13 Oxides *via* Metal Alkyl Precursors. *Chem. Mater.* **2019**, *31*, 5274−5285.

[53] She, Y.; Lee, J.; Lee, B.; Diroll, B.; Scharf, T.; Shevchenko, E. V.; Berman, D. Effect of the Micelle Opening in Self-assembled Amphiphilic Block Co-polymer Films on the Infiltration of Inorganic Precursors. *Langmuir* **2019**, *35*, 796−803.

[54] Wang, Y.; Coombs, N.; Turak, A.; Lu, Z.-H.; Manners, I.; Winnik, M. A. Interfacial Staining of a Phase-Separated Block Copolymer with Ruthenium Tetroxide. *Macromolecules* **2007**, *40*, 1594−1597.

[55] Loo, Y.-L.; Register, R. A.; Adamson, D. H. Direct Imaging of Polyethylene Crystallites within Block Copolymer Microdomains. *J. Polym. Sci. B Polym. Phys.* **2000**, *38*, 2564−2570.

[56] Trent, J. S.; Scheinbeim, J. I.; Couchman, P. R. Ruthenium Tetraoxide Staining of Polymers for Electron Microscopy. *Macromolecules* **1983**, *16*, 589−598.

[57] Segal-Peretz, T.; Ren, J.; Xiong, S.; Khaira, G.; Bowen, A.; Ocola, L. E.; Divan, R.; Doxastakis, M.; Ferrier, N. J.; de Pablo, J.; Nealey, P. F. Quantitative Three-Dimensional Characterization of Block Copolymer Directed Self-Assembly on Combined Chemical and Topographical Prepatterned Templates. *ACS Nano* **2017**, *11*, 1307−1319.

Chapter 5

Selective Deposition of Copper on Self-Assembled Block Copolymer Surfaces *via* Physical Vapor Deposition

BCP self-assembly produces chemically and topographically patterned surfaces which are used to guide the formation of Cu nanostructures by exploiting differences in the mobility of vapor-deposited species on each microdomain. Cu metal films a few nm thick were deposited on three different BCP surfaces self-assembled from PS-*b*-PMMA and PS-*b*-poly(2-vinylpyridine) (PS-*b*-P2VP). For PS-*b*-PMMA, the effects of chemical heterogeneity dominate over the effects of the 2 nm peak-to-valley topography, and sputtered Cu preferentially wets the PS block. PS-*b*-P2VP has greater chemical and topographical contrast and shows a wider process window for selective deposition. Cu grown by evaporation has less surface mobility, and shadowing effects are believed to dominate pattern formation. The hierarchical self-assembly process of thin metal films on BCP surfaces provides a route to fabricating heterogeneous metallic nanostructures. This work was published in ref 1.

5.1 Introduction

BCP self-assembly − a facile, scalable, and cost-effective way of producing a cornucopia of periodic arrays at a nanometer length scale − has been leveraged to overcome the limitations of conventional lithography.[2–7] Directed self-assembly of BCPs in particular allows for density multiplication of patterns in long-range order and generation of a variety of geometries ranging from close-packed dots or lines to more complex features such as rectilinear arrays, line segments, or lines with bends, junctions, jogs, and so on.[8–16] However, a majority of practical applications that could benefit from such well-ordered BCP nanopatterns require the functionality of metals, semiconductors, or dielectrics instead of polymeric materials.[17–23] Hence, pattern transfer from self-assembled BCPs into other materials is critically important to provide nanostructures with desired properties.

Approaches to convert the BCP morphologies into functional components may be categorized as deriving either from conventional planar fabrication processes[2,4–5,10,18–22,24] or from material hybridization or infiltration techniques.[23,25–30] The former category uses BCP microdomains as masks for etching, lift-off, or additive processes analogous to photoresist patterns. In particular, BCPs containing inorganic elements in one block, for example, PS-*b*-PDMS, exhibit high etch contrast between the constituent blocks, allowing the self-assembled BCP structures to serve as a robust lithographic mask to pattern the target materials.[5,18,24] On the other hand, infiltration synthesis techniques based on block-selective reaction of precursors within BCP microdomains offer a quick and simple route to generate three-dimensional nanostructures beyond planar assemblies.[23,25–31] These methods have been developed for specific combinations of BCPs

and precursors, but the amount of material that can be incorporated into the block is typically limited.

Preferential wetting of one of the BCP domains by deposited metal vapor species has emerged as a simple pattern transfer process based on mobility contrast of adatoms on the chemically or topographically disparate polymer blocks.[32–42,45] Lopes *et al.*[32–33] showed that metals thermally evaporated onto a self-assembled PS-*b*-PMMA film wetted one of the blocks preferentially, reproducing the underlying block morphology due to the different chemical affinity of the metals to the PS and PMMA blocks which serve as a chemical template. Erb *et al.* reported that reactive metals including Fe, Pt, and Ni sputtered on a PS-*b*-PMMA surface selectively coalesce onto the PS domains,[37] and Kreuzer *et al.*[38] and El Sachat *et al.*[40] showed preferential coverage by Ti and Cr, respectively, of the PS domains of a PS-*b*-polyethylene oxide (PS-*b*-PEO) surface. Müller-Buschbaum, Roth *et al.*[34,36,39] used glancing incidence sputter deposition to prepare anisotropic metal nanostructures on PS-*b*-PEO and PS-*b*-PMMA films. The same group investigated the evolution of Ag films on PMMA-*b*-poly(3-hexylthiophene-2,5-diyl) (PMMA-*b*-P3HT)[41] and Cu films on PS-*b*-PEO,[42] identifying the importance of reactions with the polymer, implantation of the metal into the polymer, and surface mobility. These factors also influence nanostructure formation in metals on homopolymer surfaces as do the roughness and density of the polymer surface, the metal deposition rate, film thickness, and changes to the polymer induced by the deposition process such as chain scission or cross-linking.[43–44] For Cu on PS-*b*-PEO,[42] four growth stages were identified consisting of nucleation, growth driven by diffusion, growth driven by adsorption, and grain growth. Gopinathan[45] modeled metal nanostructure formation, pointing out the importance of kinetics and surface mobility contrast in determining the final structure.

An alternative approach taking advantage of surface topography instead of chemical contrast is also expected to lead to nanostructuring of deposited materials. Substrate topography and associated shadowing effects are well-established methods to control the morphology of vapor-deposited films,[46–48] yielding a wide range of microstructures dependent on topography, angle of incidence, and substrate motion. Sundar *et al.* demonstrated the effect of a topographically modulated Pt substrate (itself patterned into periodic bumps using a BCP film/sputtered carbon bilayer as an etch mask) on the growth of composite structures of codeposited CoPt and SiO_2, where the metal coated the high points of the topography and the silica coated the valleys.[35]

In general, BCP templates exhibit both topographical and chemical contrast, but the combined effects of these two types of surface inhomogeneities have not been considered. In this study, we examine the selective deposition of Cu (a representative reactive metal with importance in interconnects) on self-assembled BCP surfaces made from films of PS-*b*-PMMA and PS-*b*-P2VP. By separately controlling the chemical and topographical modulation of BCP templates *via* the polymer composition and annealing technique, we illustrate the contributions of chemical and topographical selectivity in generating Cu nanostructures templated by the BCP domains. We also demonstrate the effect of adatom mobility in the templating of sputtered *versus* evaporated Cu.

5.2 Experimental Methods

5.2.1 Materials and Preparation of Block Copolymer (BCP) Templates

Two linear asymmetric PS-*b*-PMMA (SM-T and SM-S) and one linear asymmetric PS-*b*-P2VP (SV-S) diblock copolymers purchased from Polymer Source were used to prepare the BCP templates for Cu deposition (Table 5-1). The M_n values for each block of SM-T, SM-S, and SV-S were 50.5−20.9, 96.5−35.5, and 79−36.5 kg/mol, and the polydispersity index values were 1.06, 1.11, and 1.05 respectively. The f_{PS} for SM-T, SM-S, and SV-S was 0.73, 0.75, and 0.70, respectively. All BCP thin films were spin-coated on silicon substrates with a native oxide layer from 2 wt % (SM-T and SM-S) and 4 wt % (SV-S) solutions in toluene, which results in 80 and 200 nm thick films, respectively. The as-cast film thickness was determined by the spin speed of 3000 rpm and measured using a spectral reflectometer (FilMetrics F20-UV).

The SM-T film was thermally annealed under vacuum at 190 °C for 72 h to obtain the equilibrium morphology with long-range order.[49] Solvent vapor annealing was carried out in a glass chamber (volume ~ 80 cm^3) consisting of a solvent reservoir in which solvent vapor pressure was adjusted by nitrogen flow regulated by a mass flow controller (MKS Inc., M100B). SM-S and SV-S films on Si substrates were placed inside the chamber containing 1 mL of liquid THF and chloroform, respectively, and were annealed in a solvent vapor with a N_2 flow of 3 sccm for 30 min at ambient temperature. The chamber was tightly sealed by a quartz plate along with a perfluoroelastomer O-ring (Markez Inc., Z1210) during the annealing, and the BCP films were deswelled by raising the N_2 flow rate to 200 sccm followed by gently detaching the quartz lid from

the chamber. All the solvents used in this study were purchased from Sigma-Aldrich. More details concerning the self-assembly of identical SV-S sample can be found in ref 30.

Table 5-1. BCP properties and self-assembly processes leading to the templates of vertically aligned cylindrical morphologies in thin films.

	Molecular weight, M_n [kg/mol]	Dispersity, M_w/M_n	Composition, f_{PS}/f_{PMMA} or f_{PS}/f_{P2VP}	Thin film thickness [nm]	Annealing technique	Period [nm][a)]
SM-T	71.4	1.06	0.73/0.27	80	TA (at 190 ^{0}C)	49
SM-S	132.0	1.11	0.75/0.25	40	SVA (in THF)	52
SV-S	115.5	1.05	0.70/0.30	200	SVA (in Chloroform)	50

TA, thermal annealing; SVA, solvent vapor annealing; THF, tetrahydrofuran; [a)]Estimated from SEM and TEM images; the value for SM-S is averaged due to its less well ordered morphology.

5.2.2 Cu Deposition on BCP Templates

Cu thin films were deposited on the BCP templates at room temperature by direct current (DC) magnetron sputtering with a base pressure of 2×10^{-6} Torr. The films were sputtered at 10 mTorr of an Ar atmosphere, and their deposition rate was determined by tuning DC power ranging from 25 W (corresponding to 0.016 nm/s) to 200 W. For comparison, Cu nanostructures on the SV-S surface were also formed by electron-beam evaporation with base pressure of 2×10^{-5} Torr at deposition rates of 0.01, 0.03, and 0.05 nm/s at ambient temperature.

5.2.3 Characterization of BCP Templates and Self-Aligned Cu

The AFM measurement for BCP templates was conducted using an AFM probe with a silicon tip (PPP-NCHR, NanosensorsTM) in a non-contact mode (Park NX10, Park Systems). For the SEM images, Cu morphologies on BCP templates were first etched by RIE (Plasma-Therm 790) with O_2 (30 s, 6 mTorr, 90 W) to enhance the imaging contrast followed by Zeiss Merlin high-resolution SEM characterization at 3 kV from multiple angles. Cu-coated BCP templates were characterized by STEM (Tecnai G2 F30 S-Twin; 200 kV) and TEM (FEI Talos F200X TEM; 200 kV), respectively. X-ray photoelectron spectroscopy (XPS) surface analysis for Cu/SM-S and Cu/SV-S templates was carried out on a Kratos Axis-Supra instrument.

5.3 Results and Discussion

5.3.1 Morphologies and Height Profiles of Self-Assembled BCP Templates

Three types of templates made from annealed PS-*b*-PMMA and PS-*b*-P2VP BCP films are used in this work, consisting of vertically aligned cylinders of PMMA or P2VP microdomains in a PS matrix (Figure 5-1). Using the same PS-*b*-PMMA BCP, two disparate annealing techniques − thermal and solvent annealing − were applied to the PS-*b*-PMMA BCP to produce templates with the same surface chemistry but with different topography. As described in Figure 5-1a,b,d,e,g,h, thermal annealing at 190 °C produces a hexagonally packed cylindrical morphology where the PS matrix is ∼2 nm higher than the PMMA vertical cylindrical microdomains, while solvent annealing in THF shows less well-ordered cylinders with the opposite topography, that is, the PS matrix is lower than the PMMA cylindrical microdomains by ∼2 nm. These templates are named hereafter as SM-T for the thermally annealed PS-*b*-PMMA template and SM-S for the solvent-annealed template. A third template named SV-S was made by solvent annealing PS-*b*-P2VP in chloroform. It consists of vertically oriented P2VP cylindrical microdomains, in which the PS protrudes ∼5 nm above the P2VP (Figure 5-1c,f,i). The three templates have a periodicity around 50 nm (Table 5-1).

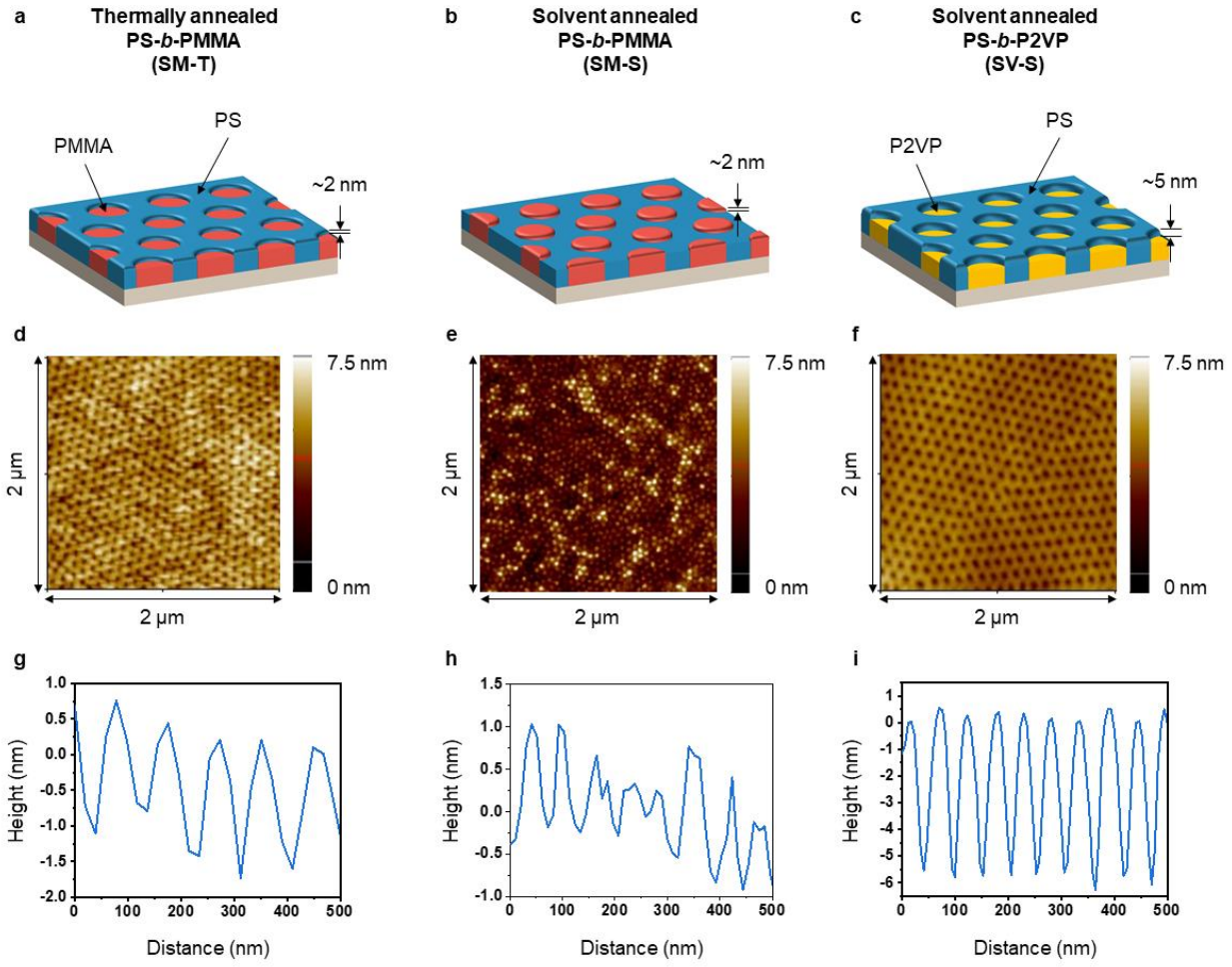

Figure 5-1. Schematic illustrations and plan-view AFM images with height profiles of self-assembled BCP thin films on Si substrates: (a,d,g) Thermally annealed PS-*b*-PMMA (SM-T), (b,e,h) solvent annealed PS-*b*-PMMA (SM-S), and (c,f,i) solvent annealed PS-*b*-P2VP (SV-S) nanostructures. All BCP morphologies here are vertically aligned PMMA (or P2VP) cylinders in PS matrix exhibiting different topographies as described in AFM profiles. Schematics in blue, red, yellow, and light gray represent PS, PMMA, P2VP, and Si, respectively.

5.3.2 Selective Cu Alignment on Self-Assembled PS-*b*-PMMA Templates

Cu was sputtered at different deposition rates (R_d) controlled by the target power, and different nominal film thicknesses (t) were controlled by the deposition time. Only a narrow growth condition of low growth rate and thickness (R_d = 0.016 nm/s, t = 3 nm) led to the selective wetting of Cu on SM-T and SM-S templates, as shown by STEM images in Figure 5-2c,d. The HAADF imaging used here is sensitive to atomic number contrast, and the pores with dark contrast indicate the locations of the PMMA cylinders, while the brighter matrix represents PS domains coated by Cu. The SM-S template shows a rougher surface with additional bright contrast in the matrix attributed to thickness variations in the Cu. Cu preferably wets the PS matrix rather than the PMMA cylinders on both templates, indicating that chemical templating was the dominant factor over topographical templating. The preferential location of Cu on the PS block is in good agreement with the results of ref 37, in which Ni and Fe are preferentially present on the PS blocks of PS-*b*-PMMA, which was attributed to higher mobility of the metal on the PMMA. Higher R_d and t led to the Cu covering both blocks of the SM-T template, as shown in the SEM images in Figure 5-3.

The R_d = 0.016 nm/s, t = 3 nm Cu/SM-T was O_2 plasma RIE and imaged by SEM. Figure 5-2f,g shows SEM images of both unetched and etched samples. The SEM of the unetched sample resembles the STEM image, as shown in Figure 5-2c, though the morphology shows weak contrast and is difficult to resolve in SEM. On the contrary, O_2 RIE removes the exposed PMMA domains while leaving the PS matrix masked by Cu. The silica substrate at the locations of the PMMA microdomains is exposed and shows bright due to charging. The PS is partly protected from

etching by the thin Cu, but the Cu itself agglomerates into small bright particles assumed to be copper oxide, visible most easily at the triple points of the PS matrix.

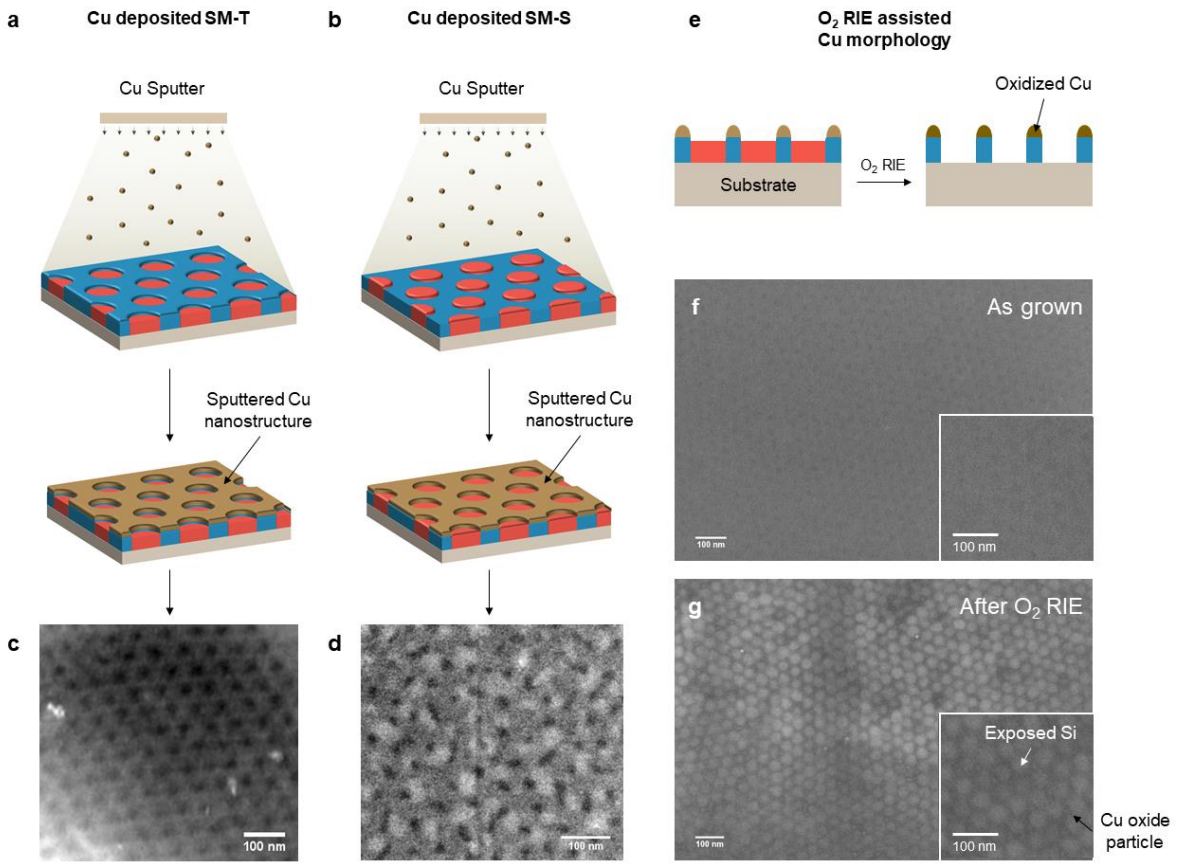

Figure 5-2. (a,b) Schematic illustrations depicting Cu sputtering onto (a) SM-T and (b) SM-S and (c,d) plan-view STEM images of Cu morphologies on the corresponding BCP structures. (e) Schematic of process used to resolve Cu morphology assisted by O_2 RIE. (f,g) Plan-view SEM images of Cu nanostructure on SM-T surface (f) before and (g) after O_2 RIE treatment, which is obtained at specific sputtering condition (R_d = 0.016 nm/s, t = 3 nm). Schematics in blue, red, brown, dark brown, and light gray represent PS, PMMA, Cu, oxidized Cu, and Si, respectively. All the scale bars in the main images and insets are 100 nm.

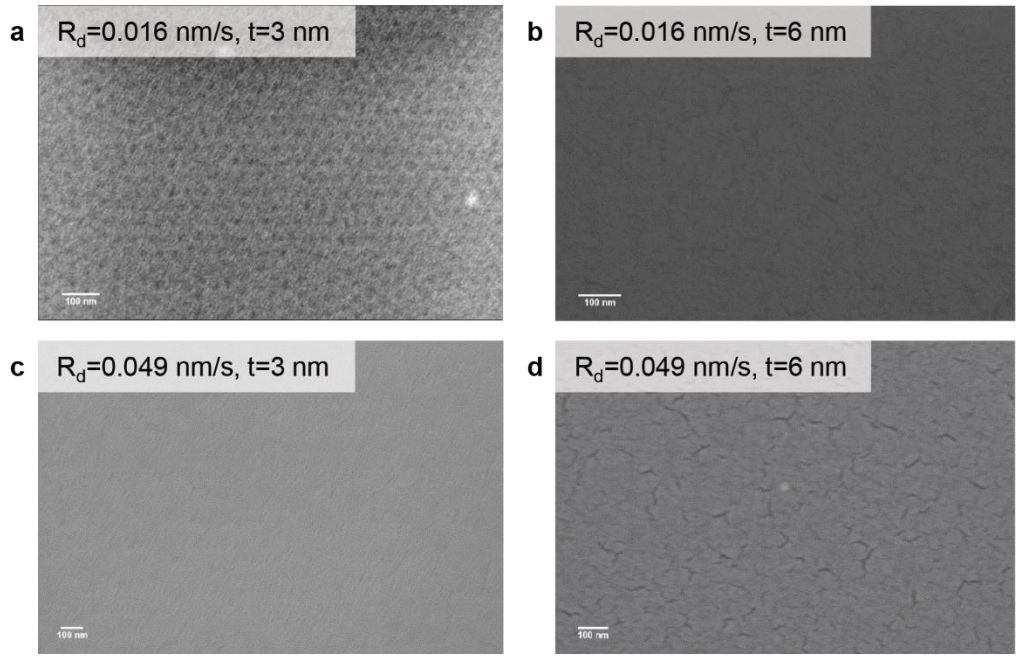

Figure 5-3. Top-view SEM images of Cu morphologies on the self-assembled SM-T thin films, which are sputtered at (a) R_d = 0.016 nm/s, t = 3 nm, (b) R_d = 0.016 nm/s, t = 6 nm, (c) R_d = 0.049 nm/s, t = 3 nm, and (d) R_d = 0.049 nm/s, t = 6 nm. All the scale bars are 100 nm.

5.3.3 Selective Cu Alignment on Self-Assembled PS-*b*-P2VP Templates

Cu was grown on top of SV-S templates using a wide range of sputtering conditions followed by O_2 RIE (Figure 5-4) in the same manner as for Cu/SM-T. Cu showed selectivity to the PS blocks over a wider range of conditions than those observed for SM-T templates, forming films with pores corresponding to the P2VP microdomains. At R_d = 0.016 nm/s, selective deposition of Cu/SV-S was observed up to t = 6 nm, whereas on SM-T, the highest thickness for selective deposition was 3 nm. Even R_d = 0.028 nm/s and t = 10 nm yielded selective deposition onto the PS block. Further

deposition of Cu at R_d = 0.028 nm/s and t = 20 nm results in a fully merged dimpled Cu film which replicates the underlying SV-S topography, and this conformal growth is also apparent for a 35 nm thick Cu layer sputtered at higher R_d of 0.049 nm/s.

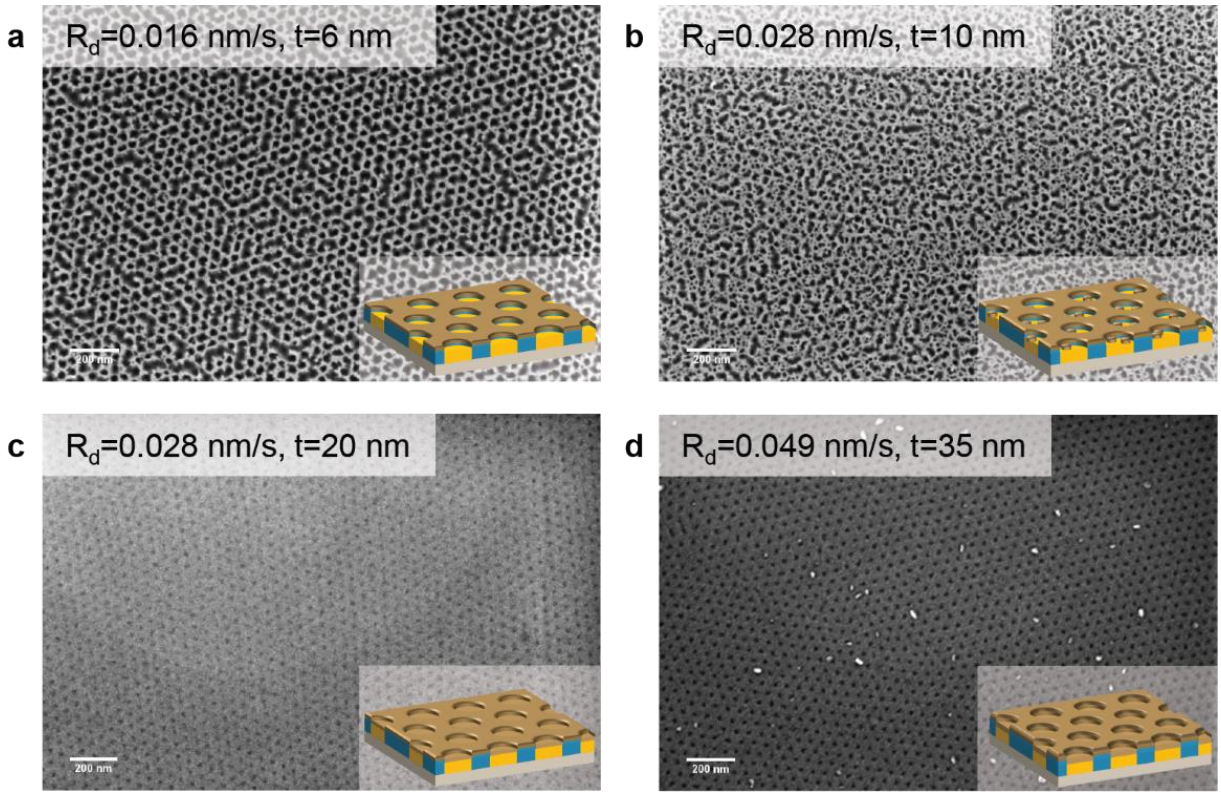

Figure 5-4. Top-view SEM images of oxidized Cu morphologies on the self-assembled SV-S thin films, which are sputtered at (a) R_d = 0.016 nm/s, t = 6 nm, (b) R_d = 0.028 nm/s, t = 10 nm, (c) R_d = 0.028 nm/s, t = 20 nm, and (d) R_d = 0.049 nm/s, t = 35 nm. Insets exhibit the schematics for the respective Cu/SV-S structures. All the scale bars in the SEM images are 200 nm. Schematics in blue, yellow, brown, and light gray represent PS, P2VP, Cu, and Si, respectively.

5.3.4 Cu Selectivity Depending on BCP Template and Deposition Technique

Surface analysis by XPS reveals the chemical interaction of sputtered Cu with the SM-S and SV-S templates, for Cu thicknesses of 0, 3, 6, and 15 nm at R_d = 0.016 nm/s (Figures 5-5 and 5-6). When the Cu thickness exceeds 6 nm, samples made on both SM-S and SV-S templates show the Cu^{2+} doublet at 933.7 and 953.5 eV corresponding to $2p^{3/2}$ and $2p^{1/2}$ peaks, respectively, and the 15 nm thick Cu on SM-S also shows the satellite peaks at 942.3 and 962.1 eV.[50−51] Oxygen peaks may be used to characterize the amount of PMMA present at the surface of the sample, as Cu is deposited. In the O 1s spectra for Cu/SM-S (Figure 5-5b), peaks corresponding to PMMA C−O bonds at 533.2 eV and C=O bonds at 531.6 eV are present in the spectrum for t = 0 nm. As the Cu thickness increases, the C−O peak slowly diminishes. The increase in intensity of the adjacent peak is attributed not to an increase in C=O bonds but to the development of a peak located at 531.3 eV corresponding to weakly charged oxygen species, O_{ad}.[50] The O_{ad} peak is thought to originate from bonding between O of the PMMA and the Cu adatoms chemisorbed on the PMMA domains. These results indicate that the PMMA has some Cu coverage even when the Cu film is thin. In contrast, the pyridinic N peak can be used to characterize the amount of P2VP present at the surface of the sample as Cu is deposited on SV-S. Figure 5-6b shows that the peak intensity for pyridinic N (at 398.2 eV) declines with increasing Cu thickness, but the N−Cu peak (at 399.0 eV)[51] is only observed at 15 nm thickness. These results are consistent with the gradual coverage of the PMMA and P2VP blocks with Cu as the Cu thickness increases.

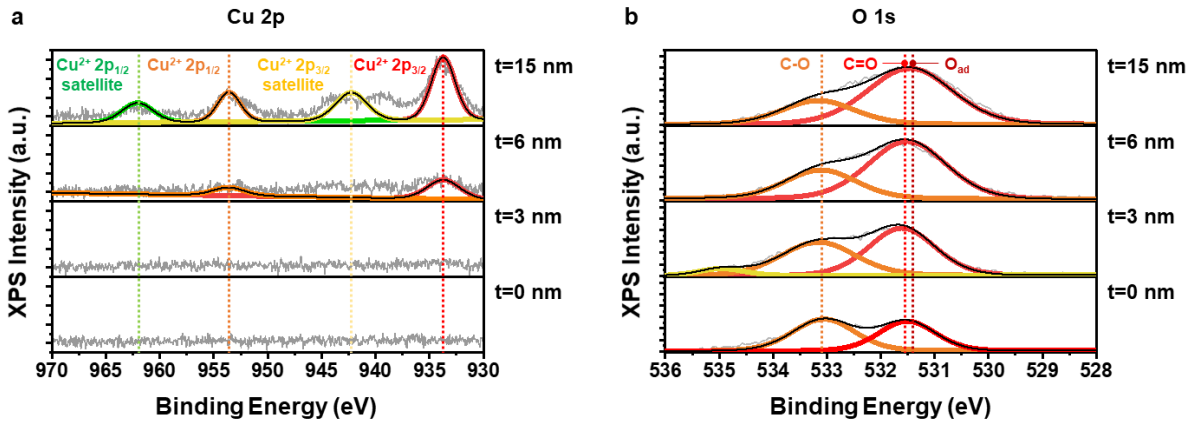

Figure 5-5. (a) Cu 2p and (b) O 1s X-ray photoelectron spectroscopy (XPS) spectra of Cu sputtered SM-S template. From the bottom to the top, each panel indicates the spectra for nominal Cu thickness of 0 nm, 3 nm, 6 nm, and 15 nm. Each set of spectra is plotted on the same relative scale.

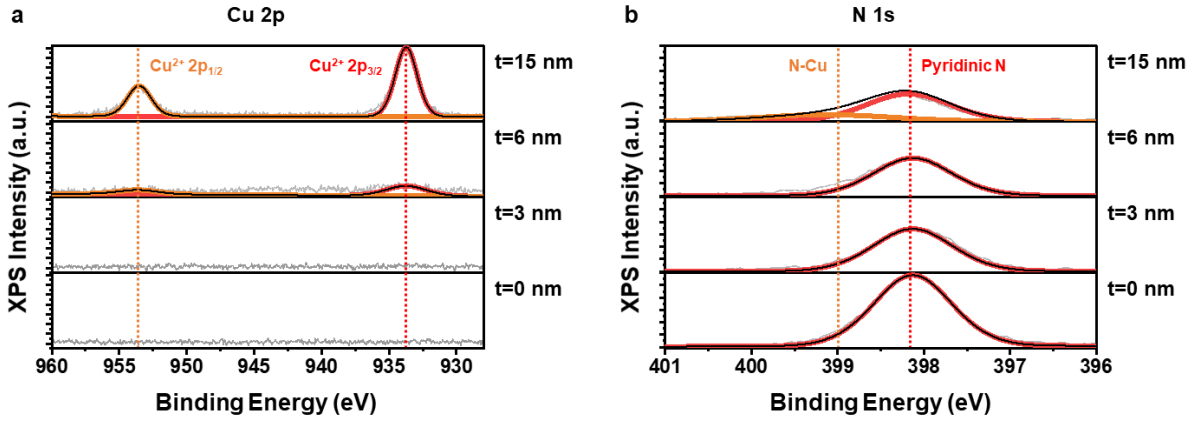

Figure 5-6. (a) Cu 2p and (b) N 1s XPS spectra of Cu sputtered SV-S template. From the bottom to the top, each panel indicates the spectra for nominal Cu thickness of 0 nm, 3 nm, 6 nm, and 15 nm. Each set of spectra is plotted on the same relative scale.

In comparison with sputtering, we found that electron-beam evaporation of Cu produced microstructures with little or no selectivity on SV-S templates. Figure 5-7 presents TEM characterization results for evaporated Cu under various deposition conditions. All the deposited Cu consisted of nanometer-sized Cu particles dispersed over the SV-S surface with almost no block selectivity. Only at the lowest R_d and t (R_d = 0.01 nm/s, t = 3 nm), a subtle difference in particle size and density was found, attributed to the shadowing effect of the topography. Denser and larger Cu clusters are formed on the higher PS matrix compared to the lower P2VP cylinders, as illustrated in the processed TEM image (Figure 5-7a). However, this effect is attenuated when either R_d or t increases (Figure 5-7b).

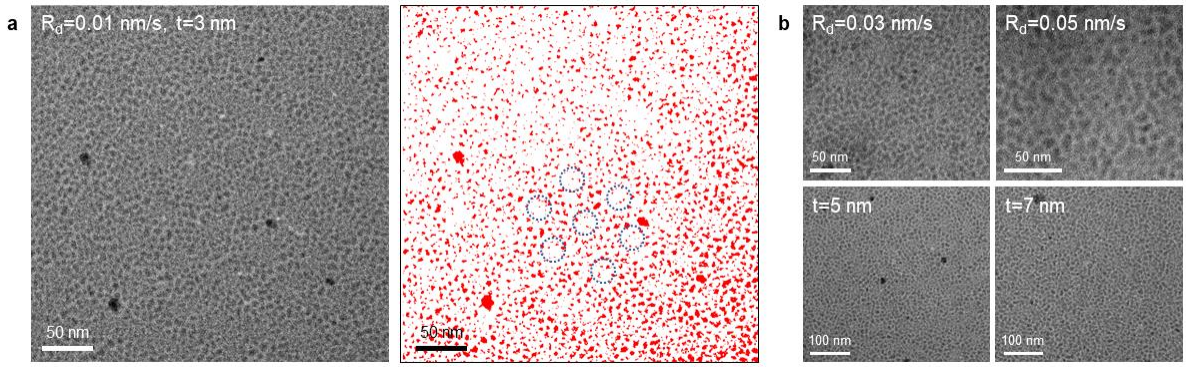

Figure 5-7. (a) TEM characterization result (left) and corresponding color-coded image (right) showing the Cu morphology on SV-S thin film deposited by e-beam evaporation at R_d = 0.01 nm/s, t = 3 nm. Only Cu particles are colored in red in the color-coded image. Blue rings indicate some of the regions of lower particle density which correspond to the surface of the P2VP cylinders. (b) Plan-view TEM images of Cu/SV-S structures, which are electron-beam evaporated at R_d = 0.03 nm/s and R_d = 0.05 nm/s for t = 3 nm (top) and for t = 5 nm and t = 7 nm at R_d = 0.01 nm/s (bottom).

As electron-beam evaporation provides metal vapor species with a lower kinetic energy than sputtered species, there is less surface diffusion or implantation, and shadowing effects dominate the morphology. On the other hand, sputtered species have greater energies and surface mobility, and the differences in mobility of adatoms and clusters, cluster agglomeration dynamics, and metal reactivity with the block lead to preferential accumulation of adatoms on one block, explaining the chemically selective growth[37,42] (as long as the topography does not prevent atom surface migration). Evaporated species have thermal energies on the order of $k_B T_e$, where T_e is the evaporation temperature. This corresponds to ∼0.25 eV for Cu taking T_e as the boiling point = 2840 K, compared to 1−10 eV or higher typical of sputtered Cu. For selective deposition originating from mobility differences, the mean free path of the adatoms needs to be on the order of the template periodicity, and the evaporated adatoms have much shorter mean free paths, precluding this mechanism. Increasing the growth or post-deposition annealing temperature (while remaining below the glass-transition temperature of PS-*b*-PMMA) may provide a strategy to increase the mobility of Cu adatoms, thus promoting their diffusion onto preferable domains, as demonstrated by Lopes *et al.*[32−33] and Erb *et al.*[37]

The results of this study show that for sputtered Cu on PS-*b*-PMMA, selectivity due to the chemical contrast is dominant over the effects of the 2 nm high topography. The Cu preferentially covers the PS block whether it is higher or lower than the PMMA block. However, selective deposition was only observed in films sputtered at low growth rates and up to a few nanometers thick. This mechanism is effective only for ultrathin films because chemical contrast is lost once a layer of Cu forms on the PMMA. Moreover, a low growth rate was required to obtain selective Cu deposition in our experiment, consistent with long equilibration times needed for the surface diffusion of adatoms.[43] This brings the additional challenge of the reaction between the metal film

and residual gases in the chamber, leading to the formation of oxides or other compounds during growth. The weaker selectivity of evaporated Cu compared to sputtered Cu on PS-*b*-P2VP for similar growth rates emphasizes the importance of adatom surface mobility.

On PS-*b*-P2VP templates, the greater chemical contrast (inferred from the higher Flory−Huggins parameter) and greater topographical contrast can both lead to greater selectivity of Cu growth compared to the PS-*b*-PMMA template. However, the increased topographic contrast is likely to inhibit the utility of the chemical contrast because it impedes the diffusion of atoms between the chemically distinct regions of the surface. A highly topographic surface can generate nanostructured Cu *via* shadowing effects, independently of the chemical interaction with the substrate features.

Given that chemical selectivity is less effective once there is more than a few nanometers of the film present, it may be most useful in a process where thin generated patterns can serve as a seed or catalyst for additional material growth steps, for example, electroless deposition or atomic layer deposition. On the other hand, the heterogeneities produced by film growth over topographic contrast tend to propagate even in thick films.

5.4 Conclusions

In summary, we describe an etchless route to transfer BCP patterns into thin copper films at a few tens of nanometers length scale. The metal features are self-aligned to specific BCP microdomains based on chemical and/or topographic contrast. In PS-*b*-PMMA, chemical contrast is dominant, and the Cu preferentially agglomerates on the PS block independent of its 2 nm height difference compared to the PMMA block. However, the selective growth occurred only for thin films at low growth rates. Solvent-annealed PS-*b*-P2VP templates provided a wider process window for making Cu nanostructures compared to PS-*b*-PMMA templates, attributed to the greater chemical and topographical contrast of PS-*b*-P2VP films. Evaporated Cu showed less selectivity than sputtered Cu, illustrating the importance of surface mobility. Selective metal deposition guided by nanoscale BCP templates thus provides a simple technique for nanofabrication of heterogeneous functional surfaces.

References

[1] Lee, S.; Lee, W.; Jung, H.-T.; Ross, C. A. Selective Deposition of Copper on Self-Assembled Block Copolymer Surfaces *via* Physical Vapor Deposition. *ACS Appl. Mater. Interfaces* **2021**, *13*, 52931−52937.

[2] Park, M.; Harrison, C.; Chaikin, P. M.; Register, R. A.; Adamson, D. H. Block Copolymer Lithography: Periodic Arrays of ~10^{11} Holes in 1 Square Centimeter. *Science* **1997**, *276*, 1401−1404.

[3] Thurn-Albrecht, T.; Steiner, R.; DeRouchey, J.; Stafford, C. M.; Huang, E.; Bal, M.; Tuominen, M.; Hawker, C. J.; Russell, T. P. Nanoscopic Templates from Oriented Block Copolymer Films. *Adv. Mater.* **2000**, *12*, 787−791.

[4] Tang, C.; Lennon, E. M.; Fredrickson, G. H.; Kramer, E. J.; Hawker, C. J. Evolution of Block Copolymer Lithography to Highly Ordered Square Arrays. *Science* **2008**, *322*, 429−432.

[5] Jung, Y. S.; Chang, J. B.; Verploegen, E.; Berggren, K. K.; Ross, C. A. A Path to Ultranarrow Patterns Using Self-Assembled Lithography. *Nano Lett.* **2010**, *10*, 1000−1005.

[6] Gotrik, K. W.; Hannon, A. F.; Son, J. G.; Keller, B.; Alexander-Katz, A.; Ross, C. A. Morphology Control in Block Copolymer Films Using Mixed Solvent Vapors. *ACS Nano* **2012**, *6*, 8052−8059.

[7] Lee, S.; Cheng, L.-C.; Gadelrab, K. R.; Ntetsikas, K.; Moschovas, D.; Yager, K. G.; Avgeropoulos, A.; Alexander-Katz, A.; Ross, C. A. Double-Layer Morphologies from a Silicon-Containing ABA Triblock Copolymer. *ACS Nano* **2018**, *12*, 6193−6202.

[8] Kim, S. O.; Solak, H. H.; Stoykovich, M. P.; Ferrier, N. J.; de Pablo, J. J.; Nealey, P. F. Epitaxial Self-Assembly of Block Copolymers on Lithographically Defined Nanopatterned Substrates. *Nature* **2003**, *424*, 411−414.

[9] Stoykovich, M. P.; Muller, M.; Kim, S. O.; Solak, H. H.; Edwards, E. W.; de Pablo, J. J.; Nealey, P. F. Directed Assembly of Block Copolymer Blends into Nonregular Device-Oriented Structures. *Science* **2005**, *308*, 1442−1446.

[10] Ruiz, R.; Kang, H.; Detcheverry, F. A.; Dobisz, E.; Kercher, D. S.; Albrecht, T. R.; de Pablo, J. J.; Nealey, P. F. Density Multiplication and Improved Lithography by Directed Block Copolymer Assembly. *Science* **2008**, *321*, 936−939.

[11] Cheng, J. Y.; Mayes, A. M.; Ross, C. A. Nanostructure Engineering by Template Self-Assembly of Block Copolymers. *Nat. Mater.* **2004**, *3*, 823−828.

[12] Bita, I.; Yang, J. K. W.; Jung, Y. S.; Ross, C. A.; Thomas, E. L.; Berggren, K. K. Graphoepitaxy of Self-Assembled Block Copolymers on Two-Dimensional Periodic Patterned Templates. *Science* **2008**, *321*, 939−943.

[13] Yang, J. K. W.; Jung, Y. S.; Chang, J.-B.; Mickiewicz, R. A.; Alexander-Katz, A.; Ross, C. A.; Berggren, K. K. Complex Self-Assembled Patterns Using Sparse Commensurate Templates with Locally Varying Motifs. *Nat. Nanotechnol.* **2010**, *5*, 256−260.

[14] Tavakkoli K. G., A.; Nicaise, S. M.; Gadelrab, K. R.; Alexander-Katz, A.; Ross, C. A.; Berggren, K. K. Multilayer Block Copolymer Meshes by Orthogonal Self-Assembly. *Nat. Commun.* **2016**, *7*, 10518.

[15] Feng, X.; Kawabata, K.; Cowan, M. G.; Dwulet, G. E.; Toth, K.; Sixdenier, L.; Haji-Akbari, A.; Noble, R. D.; Elimelech, M.; Gin, D. L.; Osuji, C. O. Single Crystal Texture by Directed Molecular Self-Assembly along Dual Axes. *Nat. Mater.* **2019**, *18*, 1235−1243.

[16] Shi, L.-Y.; Lee, S.; Du, Q.; Zhou, B.; Weng, L.; Liu, R.; Ross, C. A. Bending Behavior and Directed Self-Assembly of Rod−Coil Block Copolymers. *ACS Appl. Mater. Interfaces* **2021**, *13*, 10437−10445.

[17] Thurn-Albrecht, T.; Schotter, J.; Kastle, G. A.; Emley, N.; Shibauchi, T.; Krusin-Elbaum, L.; Guarini, K.; Black, C. T.; Tuominen, M. T.; Russell, T. P. Ultrahigh-Density Nanowire Arrays Grown in Self-Assembled Diblock Copolymer Templates. *Science* **2000**, *290*, 2126−2129.

[18] Cheng, J. Y.; Ross, C. A.; Chan, V. Z.-H.; Thomas, E. L.; Lammertink, R. G. H.; Vancso, G. J. Formation of a Cobalt Magnetic Dot Array *via* Block Copolymer Lithography. *Adv. Mater.* **2001**, *13*, 1174−1178.

[19] Jeong, S.-J.; Xia, G.; Kim, B. H.; Shin, D. O.; Kwon, S.-H.; Kang, S.-W.; Kim, S. O. Universal Block Copolymer Lithography for Metals, Semiconductors, Ceramics, and Polymers. *Adv. Mater.* **2008**, *20*, 1898−1904.

[20] Arora, H.; Du, P.; Tan, K. W.; Hyun, J. K.; Grazul, J.; Xin, H. L.; Muller, D. A.; Thompson, M. O.; Wiesner, U. Block Copolymer Self-Assembly–Directed Single-Crystal Homo- and Heteroepitaxial Nanostructures. *Science* **2010**, *330*, 214−219.

[21] Hellwig, O.; Bosworth, J. K.; Dobisz, E.; Kercher, D.; Hauet, T.; Zeltzer, G.; Risner-Jamtgaard, J. D.; Yaney, D.; Ruiz, R. Bit Patterned Media Based on Block Copolymer Directed Assembly with Narrow Magnetic Switching Field Distribution. *Appl. Phys. Lett.* **2010**, *96*, 052511.

[22] Bai, J.; Zhong, X.; Jiang, S.; Huang, Y.; Duan, X. Graphene Nanomesh. *Nat. Nanotechnol.* **2010**, *5*, 190−194.

[23] Kim, E.; Vaynzof, Y.; Sepe, A.; Guldin, S.; Scherer, M.; Cunha, P.; Roth, S. V.; Steiner, U. Gyroid-Structured 3D ZnO Networks Made by Atomic Layer Deposition. *Adv. Funct. Mater.* **2014**, *24*, 863−872.

[24] Chang, S.-W.; Chuang, V. P.; Boles, S. T.; Ross, C. A.; Thompson, C. V. Densely Packed Arrays of Ultra-High-Aspect-Ratio Silicon Nanowires Fabricated Using Block-Copolymer Lithography and Metal-Assisted Etching. *Adv. Funct. Mater.* **2009**, *19*, 2495−2500.

[25] Chai, J.; Buriak, J. M. Using Cylindrical Domains of Block Copolymers to Self-Assemble and Align Metallic Nanowires. *ACS Nano* **2008**, *2*, 489−501.

[26] Peng, Q.; Tseng, Y.-C.; Darling, S. B.; Elam, J. W. Nanoscopic Patterned Materials with Tunable Dimensions *via* Atomic Layer Deposition on Block Copolymers. *Adv. Mater.* **2010**, *22*, 5129−5133.

[27] Kamcev, J.; Germack, D. S.; Nykypanchuk, D.; Grubbs, R. B.; Nam, C.-Y.; Black, C. T. Chemically Enhancing Block Copolymers for Block-Selective Synthesis of Self-Assembled Metal Oxide Nanostructures. *ACS Nano* **2013**, *7*, 339−346.

[28] Subramanian, A.; Doerk, G.; Kisslinger, K.; Yi, D. H.; Grubbs, R. B.; Nam, C.-Y. Three-Dimensional Electroactive ZnO Nanomesh Directly Derived from Hierarchically Self-Assembled Block Copolymer Thin Films. *Nanoscale* **2019**, *11*, 9533−9546.

[29] Lee, S.; Subramanian, A.; Tiwale, N.; Kisslinger, K.; Mumtaz, M.; Shi, L.-Y.; Aissou, K.; Nam, C.-Y.; Ross, C. A. Resolving Triblock Terpolymer Morphologies by Vapor-Phase Infiltration. *Chem. Mater.* **2020**, *32*, 5309−5316.

[30] Lee, W.; Lee, S.; Tang, A. S.; Kim, C.; Liu, R.; Im, K.; Jung, H.-T.; Ross, C. A. Platinum Infiltration of a Block Copolymer for Interconnected Three-Dimensional Metal Nanostructures. *ACS Appl. Nano Mater.* **2021**, *4*, 793−801.

[31] Boontongkong, Y.; Cohen, R. E.; Rubner, M. F. Selective Electroless Copper Deposition within Block Copolymer Microdomains. *Chem. Mater.* **2000**, *12*, 1628−1633.

[32] Lopes, W. A.; Jaeger, H. M. Hierarchical Self-Assembly of Metal Nanostructures on Diblock Copolymer Scaffolds. *Nature* **2001**, *414*, 735−738.

[33] Lopes, W. A. Nonequilibrium Self-Assembly of Metals on Diblock Copolymer Templates. *Phys. Rev. E* **2002**, *65*, 031606.

[34] Metwalli, E.; Körstgens, V.; Schlage, K.; Meier, R.; Kaune, G.; Buffet, A.; Couet, S.; Roth, S. V.; Röhlsberger, R.; Müller-Buschbaum, P. Cobalt Nanoparticles Growth on a Block Copolymer Thin Film: A Time-Resolved GISAXS Study. *Langmuir* **2013**, *29*, 6331−6340.

[35] Sundar, V.; Zhu, J.; Laughlin, D. E.; Zhu, J.-G. Novel Scheme for Producing Nanoscale Uniform Grains Based on Templated Two-Phase Growth. *Nano Lett.* **2014**, *14*, 1609−1613.

[36] Roth, S. V.; Santoro, G.; Risch, J. F. H.; Yu, S.; Schwartzkopf, M.; Boese, T.; Döhrmann, R.; Zhang, P.; Besner, B.; Bremer, P.; Rukser, D.; Rübhausen, M. A.; Terrill, N. J.; Staniec, P. A.; Yao, Y.; Metwalli, E.; Müller-Buschbaum, P. Patterned Diblock Co-Polymer Thin Films as Templates for Advanced Anisotropic Metal Nanostructures. *ACS Appl. Mater. Interfaces* **2015**, *7*, 12470−12477.

[37] Erb, D. J.; Schlage, K.; Röhlsberger, R. Uniform Metal Nanostructures with Long-Range Order *via* Three-Step Hierarchical Self-Assembly. *Sci. Adv.* **2015**, *1*, e1500751.

[38] Kreuzer, M.; Simão, C.; Diaz, A.; Sotomayor Torres, C. M. Formation of Titanium Nanostructures on Block Copolymer Templates with Varying Molecular Weights. *Macromolecules* **2014**, *47*, 8691−8699.

[39] Gensch, M.; Schwartzkopf, M.; Ohm, W.; Brett, C. J.; Pandit, P.; Vayalil, S. K.; Bießmann, L.; Kreuzer, L. P.; Drewes, J.; Polonskyi, O.; Strunskus, T.; Faupel, F.; Stierle, A.; Müller-Buschbaum, P.; Roth, S. V. Correlating Nanostructure, Optical and Electronic Properties of Nanogranular Silver Layers during Polymer-Template-Assisted Sputter Deposition. *ACS Appl. Mater. Interfaces* **2019**, *11*, 29416−29426.

[40] El Sachat, A.; Spièce, J.; Evangeli, C.; Robson, A. J.; Kreuzer, M.; Rodríguez-Laguna, M. R.; Chavez, E.; Sledzinska, M.; Sotomayor Torres, C. M.; Kolosov, O. V.; Alzina, F.

Nanoscale Mapping of Thermal and Mechanical Properties of Bare and Metal-Covered Self-Assembled Block Copolymer Thin Films. *ACS Appl. Polym. Mater.* **2020**, *2*, 487−496.

[41] Gensch, M.; Schwartzkopf, M.; Brett, C. J.; Schaper, S. J.; Kreuzer, L. P.; Li, N.; Chen, W.; Liang, S.; Drewes, J.; Polonskyi, O.; Strunskus, T.; Faupel, F.; Müller-Buschbaum, P.; Roth, S. V. Selective Silver Nanocluster Metallization on Conjugated Diblock Copolymer Templates for Sensing and Photovoltaic Applications. *ACS Appl. Nano Mater.* **2021**, *4*, 4245−4255.

[42] Schaper, S. J.; Löhrer, F. C.; Xia, S.; Geiger, C.; Schwartzkopf, M.; Pandit, P.; Rubeck, J.; Fricke, B.; Frenzke, S.; Hinz, A. M.; Carstens, N.; Polonskyi, O.; Strunskus, T.; Faupel, F.; Roth, S. V.; Müller-Buschbaum, P. Revealing the Growth of Copper on Polystyrene-*block*-Poly(ethylene oxide) Diblock Copolymer Thin Films with *In Situ* GISAXS. *Nanoscale* **2021**, *13*, 10555−10565.

[43] Schwartzkopf, M.; Hinz, A.; Polonskyi, O.; Strunskus, T.; Löhrer, F. C.; Körstgens, V.; Müller-Buschbaum, P.; Faupel, F.; Roth, S. V. Role of Sputter Deposition Rate in Tailoring Nanogranular Gold Structures on Polymer Surfaces. *ACS Appl. Mater. Interfaces* **2017**, *9*, 5629−5637.

[44] Schwartzkopf, M.; Wöhnert, S.-J.; Waclawek, V.; Carstens, N.; Rothkirch, A.; Rubeck, J.; Gensch, M.; Drewes, J.; Polonskyi, O.; Strunskus, T.; Hinz, A. M.; Schaper, S. J.; Körstgens, V.; Müller-Buschbaum, P.; Faupel, F.; Roth, S. V. Real-Time Insight into Nanostructure Evolution During the Rapid Formation of Ultra-Thin Gold Layers on Polymers. *Nanoscale Horiz.* **2021**, *6*, 132−138.

[45] Gopinathan, A. Kinetic Self-Assembly of Metals on Copolymer Templates. *Phys. Rev. E* **2005**, *71*, 041601.

[46] Whitacre, J. F.; Rek, Z. U.; Bilello, J. C.; Yalisove, S. M. Surface Roughness and In-Plane Texturing in Sputtered Thin Films. *J. Appl. Phys.* **1998**, *84*, 1346.

[47] Barranco, A.; Borras, A.; Gonzalez-Elipe, A. R.; Palmero, A. Perspectives on Oblique Angle Deposition of Thin Films: From Fundamentals to Devices. *Prog. Mater. Sci.* **2016**, *76*, 59−153.

[48] Jensen, M. O.; Brett, M. J. Periodically Structured Glancing Angle Deposition Thin Films. *IEEE Trans. Nanotechnol.* **2005**, *4*, 269−277.

[49] Han, E.; Stuen, K. O.; La, Y.-H.; Nealey, P. F.; Gopalan, P. Effect of Composition of Substrate-Modifying Random Copolymers on the Orientation of Symmetric and Asymmetric Diblock Copolymer Domains. *Macromolecules* **2008**, *41*, 9090−9097.

[50] Svintsitskiy, D. A.; Kardash, T. Y.; Stonkus, O. A.; Slavinskaya, E. M.; Stadnichenko, A. I.; Koscheev, S. V.; Chupakhin, A. P.; Boronin, A. I. In Situ XRD, XPS, TEM, and TPR Study of Highly Active in CO Oxidation CuO Nanopowders. *J. Phys. Chem. C* **2013**, *117*, 14588−14599.

[51] Bulushev, D. A.; Chuvilin, A. L.; Sobolev, V. I.; Stolyarova, S. G.; Shubin, Y. V.; Asanov, I. P.; Ishchenko, A. V.; Magnani, G.; Ricco, M.; Okotrub, A. V.; Bulusheva, L. G. Copper on Carbon Materials: Stabilization by Nitrogen Doping. *J. Mater. Chem. A* **2017**, *5*, 10574−10583.

Chapter 6

Summary and Outlook

6.1 Summary

In this thesis, nanoscale engineering is introduced to tackle the major challenges in current technologies, especially in remote epitaxy, and to propose new strategies to assemble or integrate a broad range of mixed-dimensional heterostructures that are distinct from the vdW heterostructure counterparts. Three case studies are presented to exemplify how material design and engineering at nanoscale are leveraged to solve long-standing problems that are not readily overcome through the conventional techniques and methodologies: 1) nanopatterned graphene-based universal epitaxy for single-crystalline membrane transfer; 2) freestanding complex-oxide membrane growth and transfer *via* sacrificial interlayer for emergent multiferroics; and 3) self-assembled block copolymer thin films templating hybrid nanostructures.

A universal platform for releasable epitaxy with an ultimate defect reduction is developed by engineering graphene interlayer at nanoscale. Such a simple modification solves fundamental limitations in non-polar and weak semiconductor materials of which single-crystalline membranes are not remote epitaxially formed through bare graphene. Further studies of heteroepitaxy through n-Gr platform reveal its capability of reducing defects in heteroepitaxial films such as APBs and misfit dislocations, which outperforms the conventional way of mitigating defects such as selective area epitaxy based on dielectric barrier materials. This work will be an effective stepping stone

toward developing a new class of epitaxial lift-off that could be widely used not only in the laboratory-scale research but also in the industrial-scale production. A major bottleneck for the industrial use of this method may be scale up of n-Gr. Cost-effective bottom-up fabrication approaches such as block copolymer self-assembly and DNA origami self-assembly, which is studied in Part III, could be an enabler for large-area graphene nanopatterning in a deterministic manner.

A shared motivation with Part I to tackle the challenges in remote epitaxy allows to develop a strained layer-assisted chemical lift-off process for generating large-area perovskite membranes in an efficient manner. As it is demonstrated that multiferroic nanocomposite membranes can be produced with using the same approach, it is expected to greatly expand material spectrum of accessible complex-oxide membranes in addition to other classes of oxides such as spinel and garnet that can be formed by remote epitaxy.

A rich variety of self-assembled BCP thin films are used as a template for generating functional hybrid nanostructures including hierarchical 3D nanostructures and heterogeneous metallic nanostructures *via* vapor-phase infiltration and selective deposition techniques, respectively. Furthermore, nanoscale BCP templates are also expected to be introduced to Part I in order to achieve wafer-scale nanopatterning of graphene interlayer and employed in Part II in order to deterministically control the morphologies of self-assembled nanocomposite membranes.

6.2 Outlook

We summarize the technological advances of n-Gr-based epitaxy in Figure 6-1. Our new approach has a bright future in that it not only offers a numerous benefits expected from remote epitaxy but also widens material spectrum of membranes beyond those classically envisioned from remote epitaxy. As non-polar and weak materials are added to the library of material systems readily accessible for single-crystalline membrane growth and integration, we could explore a wealth of physical phenomena and new functions that have not been achieved by the conventional technologies. Moreover, a substantial reduction of defects such as APBs and dislocations in heteroepitaxy could pave a new way of heterostructuring that does not require any further layer transfer.

For example, it has been difficult to integrate high-quality Ge onto lattice-mismatched Si substrate with no aid of additional buffer layers when producing complementary metal–oxide–semiconductor (CMOS) compatible Ge photonic devices. However, we could easily stack them together *via* n-Gr-based epitaxy, either by a Ge homoepitaxy followed by its layer transfer onto Si substrate or by a dislocation-reduced Ge heteroepitaxy directly on Si substrate. In addition, hemispherical infrared photodetectors could be fabricated by n-Gr-based epitaxy. Although InAs is one of the representative materials to be utilized for state of the art infrared applications, people have been reluctant to use it mainly due to its high cost of wafer. Our approach could overcome this bottleneck by repeatedly using the same n-Gr platform to generate high-quality InAs membrane multiple times. Also, we could take advantage of its transferability to curved surface in order to produce a curvilinear focal plane arrays with a wider field of view. In principle, it is

expected to act like an electronic-eye that can detect the objects beyond a human's eyesight even in infrared regime, which could be feasible by introducing n-Gr-based epitaxy.

A complementary approach of graphene-based remote epitaxy and chemical lift-off of a wide range of freestanding complex-oxide membranes with high-crystallinity could allow an easy integration of unique heterogeneous oxide systems, where structurally and chemically incompatible materials are interfaced with each other. It is leveraged to explore new physical phenomena by creating the artificial heterostructures as well as to enhance material properties by avoiding the substrate clamping effect, which is receiving a lot of attention from complex-oxide community. It further enables an efficient control of physical properties at the interface through coupling to the external perturbations such as strain, light, gating, and proximity. For instance, a freestanding form of self-assembled BFO-CFO nanocomposites could be integrated with a piezoelectric $Pb(Mg_{1/3}Nb_{2/3})O_3$-$PbTiO_3$ (PMN-PT) layer to systematically manipulate magnetoelectric coupling at the interphases of ferroelectric perovskite of BFO and ferrimagnetic spinel of CFO.

A variety of 3D morphologies self-assembled from the advanced BCP architectures are unequivocally attractive to produce a cornucopia of mixed-dimensional nanostructures. However, a majority of practical applications that could benefit from such well-ordered BCP nanopatterns require the functionality of metals, semiconductors, or dielectrics instead of polymeric materials. Therefore, a pattern transfer from self-assembled BCPs into other materials is critically important to provide nanostructures with desired properties. In this regard, two different pattern transfer techniques (vapor-phase infiltration, Chapter 4 and selective deposition, Chapter 5) discussed in this thesis drives progress in creating functional hybrid nanostructures templated by BCP geometries with a simple sequence of processing steps. However, we still need to address the

limitations of these technologies such as low material quality in case of vapor-phase infiltration and narrow processing window in case of selective deposition.

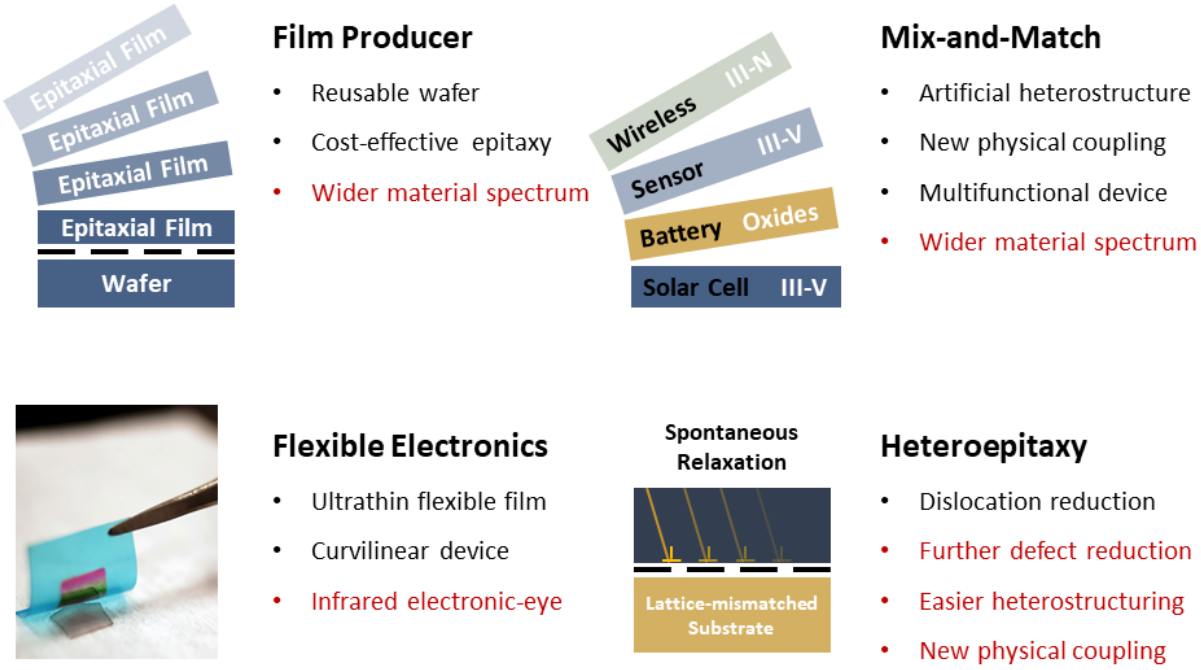

Figure 6-1. Technological advances of n-Gr-based epitaxy. Features expected in both remote epitaxy and n-Gr-based epitaxy are written in black and additional benefits in n-Gr-based epitaxy are written in red.

List of Publications

[1] **Sangho Lee**, *et al.*, Emergent Multiferroics of Self-Assembled Nanocomposite Membrane, *TBD* **2022**, *in preparation*.

[2] **Sangho Lee**, *et al.*, Remote Epitaxy and Chemical Lift-Off of Complex-Oxide Membranes, *TBD* **2022**, *in preparation*.

[3] **Sangho Lee**, *et al.*, Nanopatterned Graphene as a Universal Platform for Releasable Epitaxy with Ultimate Defect Reduction, *TBD* **2022**, *in preparation*.

[4] Ling-Ying Shi, Ashwanth Subramanian, Lin Weng, **Sangho Lee**, Kim Kisslinger, Chang-Yong Nam, and Caroline A. Ross, Selective Sequential Infiltration Synthesis of ZnO in the Liquid Crystalline Phase of Silicon-Containing Rod-Coil Block Copolymers, *Nanoscale* **2021**, *accepted*.

[5] **Sangho Lee**,[#] Wonmoo Lee,[#] Hee-Tae Jung, and Caroline A. Ross, Selective Deposition of Copper on Self-Assembled Block Copolymer Surfaces *via* Physical Vapor Deposition, *ACS Appl. Mater. Interfaces* **2021**, *13*, 52931–52937.

[6] Hyunseok Kim,[#] Kuangye Lu,[#] Yunpeng Liu, Hyun S. Kum, Ki Seok Kim, Kuan Qiao, Sang-Hoon Bae, **Sangho Lee**, You Jin Ji, Ki Hyun Kim, Hanjong Paik, Saien Xie, Heechang Shin, Chanyeol Choi, June Hyuk Lee, Chengye Dong, Joshua A. Robinson, Jae-Hyun Lee, Jong-Hyun Ahn, Geun Young Yeom, Darrell G. Schlom, and Jeehwan Kim, Impact of 2D-3D Heterointerface on Remote Epitaxial Interaction through Graphene, *ACS Nano* **2021**, *15*, 10587–10596.

[7] Ling-Ying Shi, **Sangho Lee**, Qingyang Du, Bo Zhou, Lin Weng, Runze Liu, and Caroline A. Ross, Bending Behavior and Directed Self-Assembly of Rod-Coil Block Copolymers, *ACS Appl. Mater. Interfaces* **2021**, *13*, 10437–10445.

[8] Wonmoo Lee, **Sangho Lee**, Astera S. Tang, Chansol Kim, Runze Liu, Kiseop Im, Hee-Tae Jung, and Caroline A. Ross, Platinum Infiltration of a Block Copolymer for Interconnected Three-Dimensional Metal Nanostructures, *ACS Appl. Nano Mater.* **2021**, *4*, 793–801.

[9] Kun-Hua Tu,[#] Hejin Huang,[#] **Sangho Lee**, Wonmoo Lee, Zehao Sun, Alfredo Alexander-Katz, and Caroline A. Ross, Machine Learning Predictions of Block Copolymer Self-Assembly, *Adv. Mater.* **2020**, *32*, 2005713.

[10] **Sangho Lee**, Ashwanth Subramanian, Nikhil Tiwale, Kim Kisslinger, Muhammad Mumtaz, Ling-Ying Shi, Karim Aissou, Chang-Yong Nam, and Caroline A. Ross, Resolving Triblock Terpolymer Morphologies by Vapor-Phase Infiltration, *Chem. Mater.* **2020**, *32*, 5309–5316.

[11] Ling-Ying Shi, Ji Lan, **Sangho Lee**, Li-Chen Cheng, Kevin G. Yager, and Caroline A. Ross, Vertical Lamellae formed by Two-Step Annealing of a Rod-Coil Liquid Crystalline Block Copolymer Thin Film, *ACS Nano* **2020**, *14*, 4289–4297.

[12] Hyun S. Kum,[#] Hyungwoo Lee,[#] Sungkyu Kim,[#] Shane Lindemann,[#] Wei Kong, Kuan Qiao, Peng Chen, Julian Irwin, June Hyuk Lee, Saien Xie, Shruti Subramanian, Jaewoo Shim, Sang-Hoon Bae, Chanyeol Choi, Luigi Ranno, Seungju Seo, **Sangho Lee**, Jackson Bauer, Huashan Li, Kyusang Lee, Joshua A. Robinson, Caroline A. Ross, Darrell G. Schlom, Mark S. Rzchowski, Chang-Beom Eom, and Jeehwan Kim, Heterogeneous Integration of Single-Crystalline Complex-Oxide Membranes, *Nature* **2020**, *578*, 75–81.

[13] Ling-Ying Shi, Fen Liao, Li-Chen Cheng, **Sangho Lee**, Rong Ran, Zhihao Shen, and Caroline A. Ross, Core-shell and Zigzag Nanostructures from a Thin Film Silicon-Containing Conformationally Asymmetric Triblock Terpolymer, *ACS Macro Lett.* **2019**, *8*, 852–858.

[14] **Sangho Lee**, Li-Chen Cheng, Kevin G. Yager, Muhammad Mumtaz, Karim Aissou, and Caroline A. Ross, *In Situ* Study of ABC Triblock Terpolymer Self-Assembly under Solvent Vapor Annealing, *Macromolecules* **2019**, *52*, 1853–1863.

[15] Ling-Ying Shi, **Sangho Lee**, Li-Chen Cheng, Hejin Huang, Fen Liao, Rong Ran, Kevin G. Yager, and Caroline A. Ross, Thin Film Self-Assembly of a Silicon-Containing Rod-Coil Liquid Crystalline Block Copolymer, *Macromolecules* **2019**, *52*, 679–689.

[16] Fen Liao, Ling-Ying Shi, Li-Chen Cheng, **Sangho Lee**, Rong Ran, Kevin G. Yager, and Caroline A. Ross, Self-Assembly of a Silicon-Containing Side-Chain Liquid Crystalline Block Copolymer in Bulk and in Thin Films: Kinetic Pathway of a Cylinder to Sphere Transition, *Nanoscale* **2019**, *11*, 285–293.

[17] **Sangho Lee**, Li-Chen Cheng, Karim R. Gadelrab, Konstantinos Ntetsikas, Dimitrios Moschovas, Kevin G. Yager, Apostolos Avgeropoulos, Alfredo Alexander-Katz, and Caroline A. Ross, Double-Layer Morphologies from a Silicon-Containing ABA Triblock Copolymer, *ACS Nano* **2018**, *12*, 6193–6202.

[18] Jianyuan Zhang, Peter J. Santos, Paul A. Gabrys, **Sangho Lee**, Caroline Liu, and Robert J. Macfarlane, Self-Assembling Nanocomposite Tectons, *J. Am. Chem. Soc.* **2016**, *138*, 16228–16231.

[19] Dongseong Kim, **Sangho Lee**, Yubin Hwang, Kyung-Han Yun, and Yong-Chae Chung, Hydrogen Storage in Li Dispersed Graphene with Stone–Wales Defects: A First-Principles Study, *Int. J. Hydrogen Energy* **2014**, *39*, 13189–13194.

[20] Seungchan Jo, **Sangho Lee**, Kyung-Han Yun, Yubin Hwang, and Yong-Chae Chung, Strain-Controllable Magnetism in Co Decorated Pyridinic N-Doped Graphene, *IEEE Trans. Magn.* **2014**, *50*, 1600104.

[21] Youngbin Lee, **Sangho Lee**, Yubin Hwang, and Yong-Chae Chung, Modulating Magnetic Characteristics of Pt Embedded Graphene by Gas Adsorption (N_2, O_2, NO_2, SO_2), *Appl. Surf. Sci.* **2014**, *289*, 445–449.

[22] **Sangho Lee** and Yong-Chae Chung, Nitrogen-Tuned Bonding Mechanism of Li and Ti Adatom Embedded Graphene, *J. Solid State Chem.* **2013**, *205*, 160–164.

[23] Sung Beom Cho, **Sangho Lee**, and Yong-Chae Chung, Water Trapping at the Graphene/Al_2O_3 Interface, *Jpn. J. Appl. Phys.* **2013**, *52*, 06GD09.

[24] **Sangho Lee**, Minho Lee, and Yong-Chae Chung, Geometric and Magnetic Properties of Co

Adatom Decorated Nitrogen-Doped Graphene, *J. Appl. Phys.* **2013**, *113*, 17B503.

[25] Dongseong Kim, **Sangho Lee**, Seungchan Jo, and Yong-Chae Chung, Strain Effects on Hydrogen Storage in Ti Decorated Pyridinic N-Doped Graphene, *Phys. Chem. Chem. Phys.* **2013**, *15*, 12757–12761.

[26] **Sangho Lee**, Minho Lee, and Yong-Chae Chung, Enhanced Hydrogen Storage Properties under External Electric Fields of N-Doped Graphene with Li Decoration, *Phys. Chem. Chem. Phys.* **2013**, *15*, 3243–3248.

[27] **Sangho Lee**, Minho Lee, Heechae Choi, Dong Su Yoo, and Yong-Chae Chung, Effect of Nitrogen Induced Defects in Li Dispersed Graphene on Hydrogen Storage, *Int. J. Hydrogen Energy*, **2013**, *38*, 4611–4617.

[28] **Sangho Lee**, Heechae Choi, and Yong-Chae Chung, Effects of Biaxial Strains on the Magnetic Properties of Co-Graphene Heterojunctions, *J. Appl. Phys.* **2012**, *111*, 113922.

Appendix

A. Graphene Formation Process

2D material-coated crystalline substrate works as a template for remote epitaxy, which is in general prepared by two representative methods: (a) synthesis of 2D crystals on foreign substrates, followed by their transfer onto growth substrates that remote epitaxy will be conducted and (b) direct 2D layer synthesis on growth substrate, which does not require transfer processes. Here, we focus on graphene formation process among 2D vdW materials, which has been regarded as a preferable 2D interlayer for remote epitaxy due to its transparent nature and well-developed processing steps.

In the former method, graphene is first synthesized by two major approaches: one is graphene growth on catalytic metal surfaces *via* CVD technique[1], and the other is graphitization of hexagonal SiC crystals to form epitaxial graphene on their topmost surface[2]. CVD process, wherein hydrocarbon precursors are decomposed and deposited onto metallic foils such as Cu to generate graphene, has been credited for offering an efficient route to produce large-area monolayer graphene with using low-cost substrates although it is mostly polycrystalline with micrometer- to millimeter-sized domains.[1] Pliable and rough Cu foil requires "wet-transfer" process of CVD-graphene onto target substrate as summarized in Figure Aa: spin-coating polymer support (*e.g.* PMMA) on graphene; etching away graphene on the rear side of Cu foil by O_2 plasma and Cu foil in $FeCl_3$ solution; rinsing polymer/graphene stack in DI water and scooping it by growth substrates, where remote epitaxy will be conducted on; and removing polymer support by

dissolving it in proper solvent (*e.g.* acetone for PMMA). However, this wet transfer method is likely to introduce a significant amount of unwanted defects including wrinkles, holes, polymer residues and interfacial contamination, which could disturb remote interaction between the substrate and epitaxial film through graphene. Therefore, wet transfer method can be used only for remote epitaxy of certain types of materials.

On the other hand, epitaxial graphene can be generated by sublimation of top Si-face and rearrangement of remaining C atoms on single-crystalline SiC wafers.[2] As-grown SiC-graphene is single-crystalline over whole SiC surface and "dry-transfer" process is accessible benefited from stiff and atomically flat SiC wafer, which is schematically shown in Figure Ab. For its dry transfer, Ni is first deposited on graphene as a stressor layer. To prevent damages on graphene lattice by bombardments, initial deposition of Ni needs to be done by e-beam evaporation or thermal evaporation, and once graphene is fully covered by evaporated Ni, then sputtered Ni can also be used for further deposition. Next, TRT is attached on Ni/graphene/SiC substrate to mechanically exfoliate Ni/graphene stack from SiC substrate. Released TRT/Ni/graphene stack is then manually attached onto growth substrate, wherein graphene forms vdW bonding with substrate. TRT can be removed at the elevated temperature (such as 80-150 °C) on hot plates, and lastly, Ni is removed by Ni etchant, producing graphene-coated substrate. Compared to wet-transfer process of graphene from Cu foils, dry-transfer of SiC-graphene is less likely to introduce wrinkles and residues in graphene leading to high-quality graphene uniformly covering the substrate. Also, since there is no water or any other liquid that can be trapped between graphene and substrate, dry transfer ensures much cleaner interface. However, a major downside of this approach is high cost of SiC wafers and process for graphitization that requires extremely high temperature around 1500 °C.

An alternative way of forming graphene is its direct growth on substrate that can be directly

employed for remote epitaxy. Unlike epitaxial graphene only grown on SiC wafers, CVD-graphene can be synthesized not only on metal foils but also on semiconductor substrates, which are of vital importance for advanced electronic/photonic applications. For example, it has been reported that monolayer graphene can be grown on Ge and Al_2O_3 substrates.[3-4] However, due to its high growth temperature that is typically above 900 °C, it is difficult to grow high-quality graphene directly on substrates that cannot sustain such high temperatures. By directly forming graphene on growth substrates, graphene surface can be made free of process residues and defects, which will thus be an ideal template for remote epitaxy with the cleanest interfaces. Process will also become highly scalable, thus further development of graphene growth methods on a wider variety of substrates will greatly benefit the development of remote epitaxy and related applications.

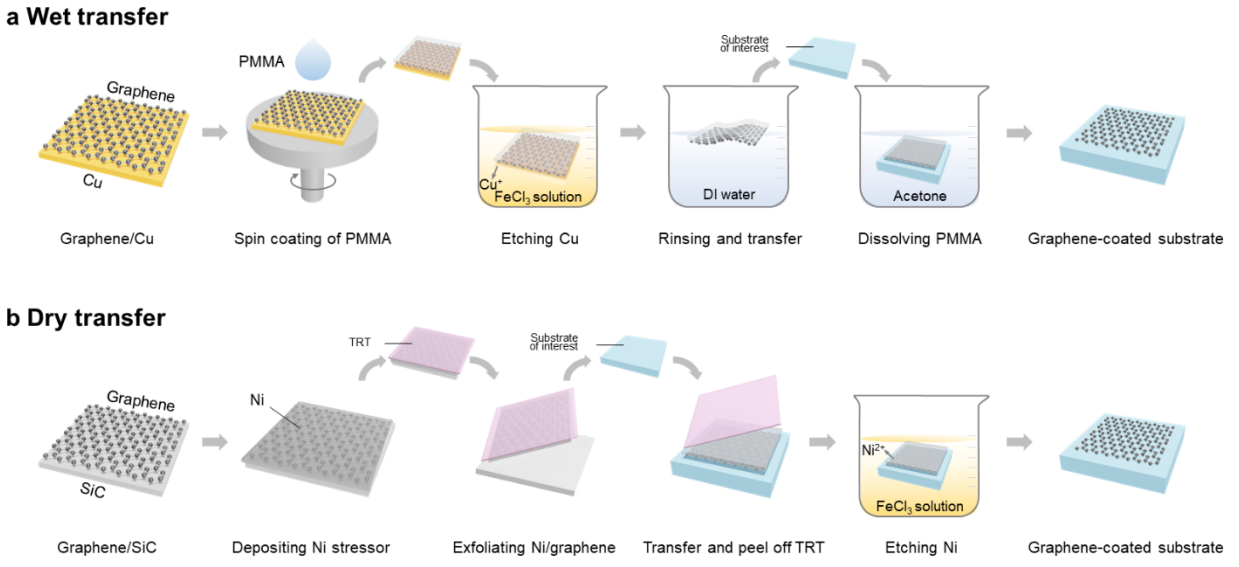

Figure A. Schematics of (a) wet transfer and (b) dry transfer process to form graphene-coated substrates.

B. Strained Layer-Based Chemical Lift-Off Process

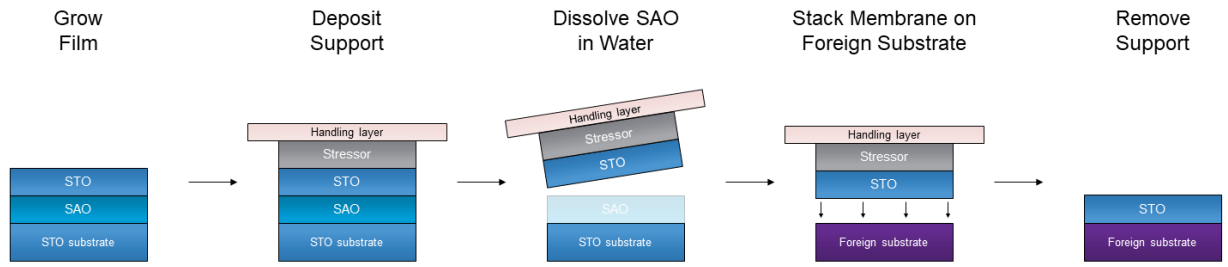

Figure B. Schematics of chemical lift-off process based on the strained layer to transfer perovskite complex-oxide membranes.

References

[1] Li, X.; Cai, W.; An, J.; Kim, S.; Nah, J.; Yang, D.; Piner, R.; Velamakanni, A.; Jung, I.; Tutuc, E.; Banerjee, S. K.; Colombo, L.; Ruoff, R. S. Large-Area Synthesis of High-Quality and Uniform Graphene Films on Copper Foils. *Science* **2009**, *324*, 1312−1314.

[2] Emtsev, K. V.; Bostwick, A.; Horn, K.; Jobst, J.; Kellogg, G. L.; Ley, L.; McChesney, J. L.; Ohta, T.; Reshanov, S. A.; Röhrl, J.; Rotenberg, E.; Schmid, A. K.; Waldmann, D.; Weber, H. B.; Seyller, T. Towards Wafer-Size Graphene Layers by Atmospheric Pressure Graphitization of Silicon Carbide. *Nat. Mater.* 2009, *8*, 203−207.

[3] Lee, J.-H.; Lee, E. K.; Joo, W.-J.; Jang, Y.; Kim, B.-S.; Lim, J. Y.; Choi, S.-H.; Ahn, S. J.; Ahn, J. R.; Park, M.-H.; Yang, C.-W.; Choi, B. L.; Hwang, S.-W.; Whang, D. Wafer-Scale Growth of Single-Crystal Monolayer Graphene on Reusable Hydrogen-Terminated Germanium. *Science* **2014**, *344*, 286−289.

[4] Hwang, J.; Kim, M.; Campbell, D.; Alsalman, H. A.; Kwak, J. Y.; Shivaraman, S.; Woll, A. R.; Singh, A. K.; Hennig, R. G.; Gorantla, S.; Rümmeli, M. H.; Spencer, M. G. van der Waals Epitaxial Growth of Graphene on Sapphire by Chemical Vapor Deposition without a Metal Catalyst. *ACS Nano* **2013**, *7*, 385−395.